Study of zero-chromatic FFAG synchrotron for muon acceleration(Dissertation_全文)

AUTHOR(S):

PLANCHE, Thomas

CITATION:

PLANCHE, Thomas. Study of zero-chromatic FFAG synchrotron for muon acceleration. 京都大学, 2010, 博士(工学)

ISSUE DATE:

2010-11-24

URL:

https://doi.org/10.14989/doctor.k15726

Study of zero-chromatic FFAG synchrotron for muon acceleration

PLANCHE Thomas

Abstract

A deeper understanding of the high-energy physics may proceed from experiments using high-energy muon beams. However, muons are unstable particles and their short lifetime as well as the large emittance of muon beams make that their acceleration remains very challenging. The aim of this study is to provide a new approach to muon acceleration for future high-energy facilities. The idea is to take advantage from the properties of zero-chromatic fixed field alternating gradient (FFAG) synchrotrons, in a way compatible with the acceleration of this very particular type of beam.

The zero-chromaticity is indeed of a great interest for the acceleration of large emittance beams since it limits the longitudinal emittance blow-up due to time-of-flight dependence on transverse amplitudes. It moreover eliminates issues related to betatron resonance crossing. Moreover, to limit the number of muons lost by decay it is necessary to accelerate them rapidly. For this purpose accelerating structure using fixed guide fields and radio-frequency (rf) cavities working at constant frequencies are preferred. Although the scaling type of FFAG combines both a static guide field with a zero-chromatic optic, their non-isochronism makes that usual acceleration methods are incompatible with constant rf frequency acceleration.

To overcome this issue, the application of two innovative acceleration methods allowing constant rf frequency acceleration with scaling FFAGs has been considered during this study. The first one, called the stationary bucket acceleration, is relying on the use of synchrotron motion inside a wide stable area of the longitudinal phase space. The second one, the harmonic number jump acceleration, uses the change of revolution time during acceleration to make particle jumping every turn inside a different stable area of the longitudinal phase space.

A fundamental understanding of these two acceleration schemes is developed, using both analytical and numerical approaches. From this understanding, examples of zero-chromatic rings are designed. In particular, a new type of zero-chromatic FFAG ring including insertions is presented. 6D particle tracking simulations are then carried out to illustrate this work and demonstrate the expected large 6D acceptance of these two different schemes. The possibility to improve the baseline design of the neutrino factory using the concepts proposed during this study is finally discussed.

Acknowledgments

First and foremost, I would like to express my sincere gratitude to my supervisor, Professor Yoshiharu Mori. I am deeply grateful for the unique chance he offered me to integrate his team, in internship first, and then as a PhD student. His wise advice, coming from his deep understanding of the accelerator physics as well as from his great open-mindedness, were precious guides all along these years.

I am deeply grateful to Dr. Yoshihiro Ishi and Dr. Tomonori Uesugi for their continuous and warm support. They were always available to answer my questions, to provide me valuable advice, and also to cheer me up the couple of times my spirits were low.

I warmly thanks my friends and colleagues Jean-Baptiste Lagrange, Hiroyuki Horii and Emi Yamakawa for the work we have done together, as for all the bad and good times we have shared.

I owe my most sincere gratitude to Mayumi Mikura, Tomoko Ono, Yuka Ono and Masako Taki, for their unbelievable kindness, their vital help to find financial supports, and for the hundreds of other things some may call "details", but life is made of nothing but such "details".

I wish to express my warm and sincere gratitude to all the member of the research team I did not named yet, who all helped me at some point during this study: Dr. Kota Okabe, Dr. Yasutoshi Kuriyama, Hirofumi Yoshino, Akihiro Osanai, Prof. Izumi Sakai, Dr. Qin Bin, Hideki Imazu, Masashi Takashima, Yoshihiro Takahoko.

The financial support from the Japanese Ministry of Education (MEXT) is also gratefully acknowledged.

Last but not least, I owe my deepest thanks to my wife Sakura, my Parents, my brother Régis, my Grandparents and my friends David Longuevergne and Yoël Giboudot, for their love which was the strongest among all supports.

Contents

Chapter 1
Introduction

The central theme of this study is the development of fixed field alternating gradient (FFAG) synchrotrons for the acceleration of muon beams. In this chapter, the basic notions, recent progress and remaining challenges in the research fields related to this topic are introduced.

1.1 Development of FFAG accelerators

1.1.1 The early age of FFAG accelerators

The FFAG accelerator is a type of circular particle accelerator which combines a static guide field, just as cyclotrons, with an alternation of focusing and defocusing elements providing the strong focusing used in modern synchrotrons. The principle of FFAG accelerators was proposed in the early 1950s, independently in Japan, USSR and USA [1, 2, 3], in application of the newly discovered alternating gradient focusing [4].

The first FFAG model, an electron machine, was build in 1955 by the Midwestern Universities Research Association (MURA) [5]. It was followed by two other electron models, a ring with spiral sector magnets in 1956 [6], and an electron colliding ring in 1961 [7]. In such machines, since the guide field is static, the position of the equilibrium orbit varies with the particle energy. To ensure stable motion of the particles over wide energy ranges, these three machines were designed to satisfy the invariance with energy of the transverse focusing. As it will be discussed in Sec. 2.1, this is possible once the closed orbits for all energies are photographic enlargements of each other. This requires a particular type of field distribution, described in Sec. 2.1. Because of the property of scaling with energy of the orbits, this type of machine is usually referred as "scaling" FFAG.

In such rings, the strong focusing can be realized by alternating normal and reversed bends. The reverse bends tend however to increase significantly the circumference factor, *i.e.* the ring size. A way to avoid negative bends is to use alternating edge focusing, by means of spiral shape magnets [8].

The particular field configuration of scaling FFAGs requires the design of complicated combined function magnets, which was uneasy at the time of the early days of finite element computations. The strong non-linear field

components which may arise from such field distribution also increase the level of complexity of these machines.

Since the end of the 1960s and for about 40 years, FFAG accelerators did not undergo any significant development. However, during the last decade, driven by the combination of new needs and newly available tools, the interest shown in this type of particle accelerator strongly revived [9].

1.1.2 The rebirth of FFAGs

Several research fields are indeed showing a strong interest for the unique features of FFAG accelerators, as indicates the increasing number of FFAGs built or under commissioning all around the world.

The production of high-power proton beams is the major reason at the origin of the recent developments. Because of their static guide field, the time needed to complete an acceleration cycle is not limited by magnet ramping issues, by contrast with pulsed synchrotrons. Higher repetition rates are possible with FFAG rings, which is of a great interest for application requiring a high beam power. Moreover, the alternating gradient focusing allows the use of much higher field gradients than in cyclotrons. For a given energy range, a larger field gradient allows to significantly reduce the beam excursion, and therefore the size of the magnets. This way, high-energy proton accelerators can be achieved, as indicates the various multi-GeV FFAG proton drivers already proposed [10, 11, 12].

The world first proton FFAG, which accelerated protons from 50 keV to 500 keV, was build and successfully operated at the High Energy Accelerator Research Organization (KEK) in 2000 [13]. This machine was made of eight radial sector scaling FFAG cells, adopting for the first time the triplet type of FFAG cell [14]. It was followed by the first MeV class proton FFAG, a 150 MeV radial sector ring, successfully commissioned at KEK in 2004 [15].

The world first accelerator driven system (ADS) using spallation neutrons generated by high-energy proton beams started at Kyoto University Research Reactor Institute (KURRI) in March 2009, making use of the 100 MeV proton beam produced by an FFAG complex [16]. This facility is composed of three scaling FFAG rings in cascade, a spiral FFAG injector followed by two radial sector rings, and is designed to accelerate protons up to 150 MeV [17].

The development of FFAG for the production of high power proton beams has been followed by a growing interest in other fields of research. The production of pure and quasi-monoenergetic muon beams, initiated the development and construction of the PRISM FFAG ring [18, 19]. The further work is now gathered within the PRISM task force [20].

More recently, the production of intense source of secondary particles from proton beams stimulated the development and construction of the energy recovering internal target (ERIT) FFAG scheme [21, 22]. The capability

of rapid-cycling as well as the possibility to vary the extraction energy motivated the design of FFAG rings for hadrontherapy [23, 24].

Finally, by relaxing on the condition of scaling of the orbits, a wide variety of machines, called non-scaling FFAG rings, could be designed. This concept led to the development of the EMMA ring [25], which is currently under commissioning at Daresbury laboratory in the UK.

Many tools, which were not available in the early age of FFAGs, played an essential role in the recent developments. FFAG magnets producing well-controlled non-linear field distribution are now designed with the help of finite element magnetic computation [26, 27, 28]. The linear lattice parameters are easily studied thanks to well-established matrix code such as SAD [29]. Non-linear beam dynamics is commonly studied with available step-wise particle tracking code such as Zgoubi [30, 31, 28]. The development of broad band radio-frequency (rf) cavities, using magnetic alloy loaded cavities [32, 33], also strongly contributed to the recent developments. With such cavities rapid frequency sweeping with relatively high rf voltages is achieved, allowing thus high repetition rates in proton FFAGs.

1.2 Acceleration of muon beams

The production of high-energy muon beams is considered for various purposes. One of these is the high-energy muon radiography [34], which is considered of great interest for several applications such as medical imaging [35] or detection of hidden heavy nuclear materials in cargo containers [36].

From the point of view of high-energy physics experiments, the interest of muon beams is twofold. On the one hand, the next generation of lepton-antilepton collider could be in the form of a $\mu^+ \mu^-$ collider. Collisions between leptons are preferable for precise measurements of new phenomena. It comes from the fact that leptons are single particles, by contrast with hadrons which are composite particles. For electron-positron colliders such as the former large electron position collider (LEP) at CERN, the achievable particle energy is however limited by the energy losses due to synchrotron radiation. The energy lost per particle and per turn in such machines follows a law in E^4/r [37], with E the electron/position energy and r the machine radius. Since the ring size cannot be made impractically large, this phenomena limits in practice the electron/position energy to the 100 GeV range. One way to overcome this problem is to use linear structures. However with current technologies, such a machine must be very long to reach the TeV of center-of-mass energy ($\sim$31 km for the international linear collider ILC [38]). Since the radiation losses follow also the inverse of the fourth power of the particle rest mass, another way to overcome this problem is to use heavier leptons, such as muons. The great prospect of precise measurement and

discovery of new physics are discussed in this reference paper [39].

On the other hand, high energy muons circulating in a storage ring will decay producing neutrinos. The idea of a dedicated facility, called a neutrino factory, making use of this principle for neutrino physics experiments has been proposed and discussed in Ref. [40]. In such a facility, muon beams accelerated to a few 10 GeV circulate in a storage ring with long straight sections orientated toward distant neutrino detectors. A great interest of this scheme is that the flux and mixture of the neutrino beams produced[1] is well known. The small divergence and the high energy of the produced neutrino allow also high rates of neutrino events in far detectors. The outstanding prospects of study of neutrino oscillations and understanding of the physics beyond the standard model are detailed in the following Ref. [41]. Because of its lower level of complexity, a neutrino factory can also be seen, in addition to the interest it has on its own, as an intermediate step toward a muon collider [42]. For these reasons, a neutrino factory is a good candidate for the next world-class facility for particle physics.

Several design studies of a neutrino factory have been produced worldwide [43, 42, 44, 45], and international efforts are today gathered within the "International Design Study for the Neutrino Factory" (IDS-NF) [46]. A schematic view of a recent baseline design produced by this international collaboration is presented in Fig. 1.1.

This baseline design consists, first of all, of a proton accelerator complex (called proton driver) which provides a high-power beam to a mercury target. The charged pions produced by interaction of the proton beam on the target are captured by means of a strong solenoidal field. Charged pions are then transported in a linear decay channel, where they decay producing the both muons μ^- and anti-muons μ^+. The resulting muon beam is then longitudinally manipulated (bunching and phase rotation). Next, an ionization cooling channel is used to reduce the transverse emittance of the muon beams. And then starts the process of muon acceleration which is the core issue of this study.

As part of this international effort, the development of accelerating structures capable to accelerate in a very short time muon beams is required. Because of the short lifetime of muons ($\sim$2.2μs), the rapid acceleration is essential to limit the number of muons lost by decay. Such rapid acceleration is possible in accelerating structures free from magnet ramping and frequency sweeping issues. For this reason, structures using fixed guide field and constant rf frequency, such as linear accelerators, recirculating linear accelerators (RLA) and FFAG synchrotrons, are preferred.

Linear type of non-scaling FFAG lattices have recently been developed

[1] Depending on the type of muon, the decay follows either $\mu^- \longrightarrow e^- + \bar{\nu}_e + \nu_\mu$, or $\mu^+ \longrightarrow e^+ + \nu_e + \bar{\nu}_\mu$.

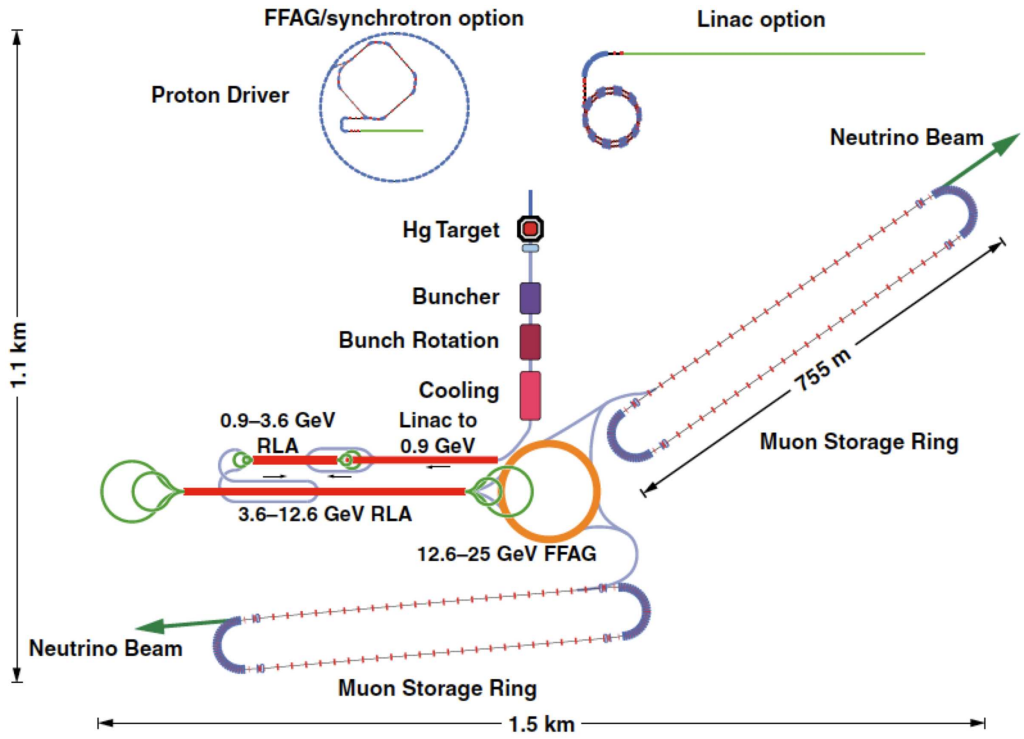

Figure 1.1: Schematic view of the baseline design of a neutrino factory of the IDS-NF. Details concerning the design can be found in Ref. [45], from which this picture is reproduced.

for this purpose [47]. Such a scheme has numerous features which are great advantages in the case of the acceleration of muons: (i) it uses only linear magnets which are simpler to produce compared to the scaling type of FFAG magnets; (ii) the excursion can be small once high field gradient are used; (iii) this type of ring can be made almost isochronous, which allows constant rf frequency acceleration. However this type of machine has its own limitations coming from the lost of the invariance in the optical properties with energy. This causes betatron resonance crossing during acceleration. Very fast acceleration is then required to limit the deterioration of the beam emittance and beam losses. The transverse acceptance in such rings is also highly sensitive to errors [48], which may either come from fringing field or alignment errors. The significant tune variation with energy (commonly called chromaticity) introduces also a dependence of the time of flight on the transverse amplitude [49], which can induce significant longitudinal emittance blow-up [50].

Depending on the proposed scenario, no cooling [43] or a limited amount of ionization cooling [42] is considered prior to the acceleration of the muon beams. In both cases, in order to accelerate a large number of muons and

produce the required neutrino flux, one has to manipulate muon beam with huge transverse emittance. In the most recent baseline scenario [51], the normalized transverse emittance of the accelerated beam if set to the very unusually large value of 30,000 πmm.mrad for both horizontal and vertical planes.

In the present baseline design, a linear accelerator is used as pre-acceleration stage, bringing muons beams to ultra-relativistic energy ($\beta \approx 1$). The next acceleration stages are relying on RLAs at intermediate energies, and linear non-scaling FFAG rings at higher energies to reduce the cost by multiplying the passes through the rf cavities. The RLAs are less cost-effective than FFAG rings, because a different arc is required for each pass through the linac, and because the number of passes is limited to 4 or 5 [45]. But the longitudinal emittance growth, caused by the dependence of the time of flight on the transverse amplitude, tends to constraint the use of a single non-scaling FFAG ring for the highest acceleration stage [50].

1.3 Purpose of the study

One feature of the scaling type of FFAG rings is that their chromaticity is null. The first order dependence of the time of flight on the transverse amplitude thus disappears, by contrast with linear FFAGs [49]. Scaling FFAGs are then less affected by the longitudinal amplitude growth for large transverse amplitude, which limits the use of non-scaling FFAGs. Moreover, since betatron tunes stay constant during acceleration, one can avoid the issue of resonance crossing. With a proper choice of the working point, far from harmful resonances, huge dynamic apertures can be achieved over the whole energy range.

The use of scaling FFAG rings for muon acceleration has already been proposed in a former study [43]. But designs presented in Ref. [43] assumed variable frequency acceleration at frequencies of the order of 5 MHz, which is incompatible with the present baseline scenario [52]. The choice of ionization cooling prior to acceleration indeed imposes the use of only $\sim$200 MHz, or a multiple as the frequency of each rf cavities of the acceleration stage. Innovative acceleration schemes were thus needed to put forward competitive solution based on scaling FFAGs.

The purpose of this study is to reexamine the possibilities offered by this type of ring, considering innovative constant frequency acceleration schemes. We thus aim to determine whether or not we can achieve the fast acceleration of muon beams, from lower energies than non-scaling FFAG rings, and in a more cost efficient way than RLAs.

1.4 Organization of the study

Essential properties of the scaling type of FFAGs are recalled in Chapter 2. Two ways to accelerate particles with constant frequency rf cavities in such rings are then successively considered. The Chapter 3 is dedicated to the case of the so-called stationary bucket acceleration. The Chapter 4 is dedicated to the study of the harmonic number jump acceleration scheme. In both cases the constraints fixed by each particular acceleration scheme on the lattice parameters are determined. Tools to understand the transverse and the longitudinal beam dynamics in such schemes are developed. Example of 3.6 to 12.6 GeV muon rings are presented, and the 6D beam dynamics in these examples is studied by means of step-wise particle tracking. Finally, the performance of these schemes are summarized and compared in Chapter 6, which allow us to discuss the possibility to improve the present baseline design of a neutrino factory using such zero-chromatic FFAG rings.

Chapter 2

Basic study of scaling FFAG accelerators

The aim of this chapter is to provide a proper understanding of the basic properties of the scaling type of FFAG rings. Starting from the most fundamental of them, which is the invariance with energy of the betatron oscillations, the property of scaling between the different closed orbits is deduced and the general form of the required field distribution is derived. Then, fundamental principles of non-linear beam dynamics which are essential to understand the particle motion in scaling FFAG rings are recalled. Consequences of the scaling field law on the longitudinal motion of particles, and on the method required to achieve constant rf frequency acceleration, are finally discussed.

2.1 Scaling field law

To study the motion of charged particles in the static magnetic field of FFAG rings, let's start from the following assumptions:

Hypothesis 1. *For any momentum p, it exists a unique closed orbit.*

Hypothesis 2. *Every closed orbit lies in the machine mid-plane ($z = 0$).*

Each closed orbit is then represented in cylindrical coordinates (r, θ, z) by:

$$\begin{cases} r = r_{co}(\theta, p), \\ z = 0. \end{cases} \tag{2.1}$$

Along the closed orbit for an arbitrary momentum p, a right-handed curvilinear coordinate system (x, s, z) is defined as shown in Fig. 2.1.

The motion of a particle of momentum p around the closed orbit is described, for small amplitudes, by the following linearized equations of motion

$$\begin{cases} \dfrac{\mathrm{d}^2 x}{\mathrm{d}s^2} + \dfrac{1}{\rho^2}(1-n) \cdot x = 0, & \text{(a)} \\ \dfrac{\mathrm{d}^2 z}{\mathrm{d}s^2} + \dfrac{n}{\rho^2} \cdot z = 0\,, & \text{(b)} \end{cases} \tag{2.2}$$

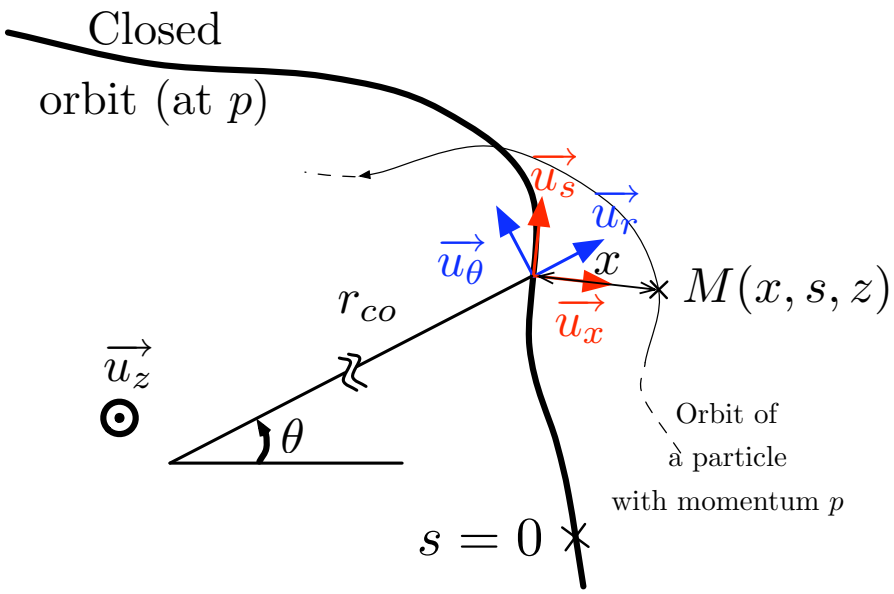

Figure 2.1: The position M of a particle with momentum p is determined by its local coordinates (x, s, z).

with ρ the local radius of curvature of the closed orbit, and n the field index, defined as:

$$n = -\frac{\rho}{B}\left(\frac{\partial B}{\partial x}\right)_{\perp}, \tag{2.3}$$

with B the vertical component of the magnetic field. The symbol $\perp$ here signifies that the partial derivative is done in the machine mid-plane perpendicularly to the closed orbit, and evaluated at $x = 0$.

Since we are considering particle circulating around closed orbits, the parameters n and ρ are periodic functions of s, with period L:

$$n(s+L) = n(s) \qquad \text{and} \qquad \rho(s+L) = \rho(s). \tag{2.4}$$

The period L is a fractional part of the ring circumference C:

$$L = C/N, \tag{2.5}$$

with N an integer called the ring periodicity ($N \geq 1$). Equations 2.2(a) and 2.2(b) are thus in the form of Hill's equations which general solutions can be written in the form [53]:

$$y = \sqrt{\epsilon}\sqrt{\beta(s)}\cos(\nu\phi(s) + \phi_0), \tag{2.6}$$

where ϵ and ϕ_0 are arbitrary constants, and y stands for either x or z. The constant ϵ is usually called the emittance of the particle. The function $\beta(s)$

is also periodic with period L. The parameter ν is called the cell tune, and is given by:

$$\nu = \frac{1}{2\pi}\int_{s}^{s+L}\frac{\mathrm{d}s}{\beta}. \tag{2.7}$$

As for the phase $\phi(s)$, it is defined as:

$$\phi(s) = \int\frac{\mathrm{d}s}{\nu\beta}. \tag{2.8}$$

The motion of particles described by Eq. 2.6 can thus be seen as an oscillation around the equilibrium orbit, commonly called the betatron oscillation, characterized by its frequency ν and its amplitude modulated following the square root of the beta-function β. Thereafter, subscripts notations are used to distinguish the horizontal cell tune ν_x from the vertical one ν_z, and the horizontal beta-function β_x from the vertical one β_z.

The definition of the cell tune allows us to introduce the related notion of *zero-chromaticity*, which is defined as the invariance of both the horizontal and the vertical cell tunes with respect to the energy (momentum) of the particles. Let Q be the ring tune defined as:

$$Q = N\nu, \tag{2.9}$$

with N the ring periodicity. Like for the cell tune the notations Q_x and Q_z are used to designate the horizontal and the vertical ring tune, respectively.

To go further we define the notion of closed orbit equivalent radius R defined as:

$$R = \frac{1}{2\pi}\oint \mathrm{d}s, \tag{2.10}$$

The equivalent radius R is independent of the position s along a closed orbit, and thus depends only on p. Let Θ be the corresponding azimuthal coordinate defined as:

$$s = R\Theta. \tag{2.11}$$

The linearized equation of motion can now be re-written in the coordinate system (Θ, x, z):

$$\begin{cases} \dfrac{\mathrm{d}^2x}{\mathrm{d}\Theta^2} + \dfrac{R^2}{\rho^2}(1-n)\cdot x = 0 \\ \dfrac{\mathrm{d}^2z}{\mathrm{d}\Theta^2} + \dfrac{R^2}{\rho^2}n\cdot z = 0\,, \end{cases} \tag{2.12}$$

A necessary and sufficient condition of the invariance with momentum of the betatron oscillations along the curves $\Theta = const.$ is thus given by:

$$\boxed{\text{(a)}: \quad \left(\frac{\partial(R/\rho)}{\partial p}\right)_{\Theta} = 0 \quad \text{and} \qquad \text{(b)}: \quad \left(\frac{\partial n}{\partial p}\right)_{\Theta} = 0.} \tag{2.13}$$

The Eq. 2.13.a expresses the condition of geometrical similarity of the closed orbits. As it is shown in App. A.1 it implies that the closed orbits for different momentums are all photographic enlargements of each other.

It is important to notice that the invariance with momentum of the betatron oscillations is only a sufficient condition to achieve zero-chromaticity. It is indeed possible to design lattices, which are zero-chromatic over a wide energy range, and which do not satisfy the condition of scaling of the closed orbits, as shown in Chapter 4.

As it is demonstrated in App. A.1, *once the curve $\Theta = 0$ is chosen following a logarithmic spiral*, a necessary and sufficient condition of the invariance with momentum of the betatron oscillations is that the magnetic field distribution in the machine mid-plane follows

$$\boxed{B(r,\theta) = B_0 \left(\frac{r}{r_0}\right)^k \mathcal{F}(\theta - \tan\zeta \ln\frac{r}{r_0}),} \tag{2.14}$$

where $\mathcal{F}$ is a function independent of p, k is a constant called the geometrical field index, and ζ is a constant and corresponds to the spiral angle. The radial sector type of scaling FFAG ring simply corresponds to the particular case where ζ is chosen null.

2.2 Basic considerations of non-linear beam dynamics

To estimate the amount of non-linear field component arising from such a field distribution we choose the following approach: limiting ourself to the case of radial sector machines and assuming a quasi-circular closed orbit, the Taylor expansion of the magnetic field around this orbit simply writes:

$$\begin{aligned} B(r,\theta) &= B(r_{co},\theta)\left(\frac{r}{r_{co}}\right)^k \\ &= B(r_{co},\theta)\left(1 + \frac{k}{r_{co}}x + \frac{k(k-1)}{2!r_{co}^2}x^2 + \frac{k(k-1)(k-2)}{3!r_{co}^3}x^3 + ...\right), \end{aligned} \tag{2.15}$$

where x is the distance of the particle to the closed orbit, given in the case of a quasi-circular closed orbit, as $x = r - r_{co}$. One thus can see that, except in the very particular case where k = -1, 0 or 1, the scaling field law gives rise to non-linear (*i.e.* of order > 1) field components. To understand the beam dynamics in scaling FFAG rings, it is thus essential to consider the effect of these non-linear components.

A general method to treat this problem is to consider the effect of non-linear field components as perturbation terms of linearized equations of motion such as given in Eq. 2.2. Without entering into the detail of this approach, as it is extensively described in reference papers such as Refs. [54, 55], we simply recall in this section the general expression of resonance condition in non-linear field distribution:

$$m_x Q_x + m_z Q_z = q, \tag{2.16}$$

where m_x, m_z and q are *small* integers. When the working point (Q_x, Q_z) is close to such a resonance condition, the amplitude of transverse motion may increase, giving rise to emittance degradation and possibly beam losses. This is the reason why one generally try as much as possible during this study to avoid exciting such a resonance behavior.

In the absence of errors, *i.e.* when the periodic cells are actually all identical, the resonance condition reduces to:

$$m_x \nu_x + m_z \nu_z = q. \tag{2.17}$$

These resonances are called *structure resonances*. Moreover, in scaling FFAG rings in the absence of error, the machine mid-plane is an anti-symmetry plane of the field distribution. Skew field components are thus excluded, which reduce further the resonance condition to the case where m_z is an even number.

2.3 Acceleration in scaling FFAG synchrotrons

In this section the basic notions used to understand the rf acceleration and study the longitudinal motion in scaling FFAGs are presented.

2.3.1 Classical approach of the synchrotron motion

In most circular accelerators, the energy of particles is increased by means of electric fields produced in the gap of radio frequency (rf) cavities, which oscillate at a frequency f_{rf} closed to an integer multiple of the revolution frequency of the particles. The condition of synchronization of the rf frequency with the revolution frequency f_{rev_s} of a *synchronous* particle simply writes:

$$f_{rf} = h \cdot f_{rev_s}, \tag{2.18}$$

where h is an integer called the harmonic number.

To locate particles around the accelerator ring, let's consider the azimuthal coordinate Θ defined as:

$$\Theta = \int_0^s \frac{2\pi}{C} \mathrm{d}s, \tag{2.19}$$

with C the circumference of the particle closed orbit for a momentum p, and s the distance traveled by the particle. Assuming that the rf cavities are uniformly distributed around the ring, one can write the general equations of the longitudinal motion as:

$$\begin{aligned} mc^2 \frac{\mathrm{d}\gamma}{\mathrm{d}\Theta} &= \frac{eV_0}{2\pi} \sin\phi \\ \frac{\mathrm{d}\phi}{\mathrm{d}\Theta} &= f_{rf} \cdot \frac{C}{\beta c} - h, \end{aligned} \tag{2.20}$$

where ϕ is defined as $\phi = 2\pi f_{rf}\ t - h\Theta$, βc is the particle velocity, m is its rest mass, γ is its Lorentz factor, t is its time coordinate, and V_0 is the sum over one turn of the rf cavities peak voltage.

To quantify the relative change in revolution frequency f_{rev} of a particle with momentum, one generally use the *phase slip factor* defined as:

$$\eta = \frac{\mathrm{d}\ln(f_{rev})}{\mathrm{d}\ln(p)} = \frac{1}{\gamma^2} - \alpha, \tag{2.21}$$

where p is the momentum of the particle, γ its Lorentz factor, and α is the *momentum compaction factor*, defined as:

$$\alpha = \frac{\mathrm{d}\ln C}{\mathrm{d}\ln p}. \tag{2.22}$$

The classical approach described in several textbooks such as Refs. [56, 57] consists in considering the motion of particles in the vicinity of a synchronous particle (*i.e.* small energy deviation), assuming that the synchronous particle energy $\gamma_s mc^2$ and revolution frequency f_{rev_s} vary slowly compared to the independent variable Θ. One can then re-write Eq. 2.20 as:

$$\begin{aligned} \frac{\mathrm{d}\Gamma}{\mathrm{d}\Theta} &= \frac{eV_0}{2\pi mc^2}(\sin\phi_s - \sin(\Phi + \phi_s)) \\ \frac{\mathrm{d}\Phi}{\mathrm{d}\Theta} &= h\eta \frac{\Gamma}{\beta_s^2 \gamma_s}, \end{aligned} \tag{2.23}$$

where $\Gamma = \gamma_s - \gamma$ and $\Phi = \phi - \phi_s$, with ϕ_s the synchronous phase. An Hamiltonian associated to these equations is given by:

$$H(\Phi, \Gamma; \Theta) = \frac{h\eta\Gamma^2}{2\beta_s^2\gamma_s} - \frac{eV_0}{2\pi mc^2}(\cos(\Phi - \phi_s) + \Phi \sin\phi_s) \tag{2.24}$$

For small amplitudes, *i.e.* Φ small, this Hamiltonian becomes:

$$H(\Phi, \Gamma; \Theta) \simeq \frac{h\eta\Gamma^2}{2\beta_s^2\gamma_s} + \frac{eV_0\cos\phi_s}{4\pi mc^2}\Phi^2. \tag{2.25}$$

When η and $\cos\phi_s$ have the same sign, this corresponds to the Hamiltonian of an harmonic oscillator, which number of so-called synchrotron oscillations per unit of Θ is given by:

$$2\pi\nu_s = \sqrt{\frac{h\eta eV_0\cos\phi_s}{2\pi\beta_s^2\gamma_s mc^2}}, \tag{2.26}$$

where ν_s, the number of synchrotron oscillations per turn, is commonly called the synchrotron tune.

2.3.2 Particularities of scaling FFAG accelerators

A consequence of the scaling field law given in Eq. A.20 is that the circumference of the closed orbits scales as:

$$C \propto p^{\frac{1}{k+1}} \tag{2.27}$$

The momentum compaction factor as defined in Eq. A.25 is then constant and given by:

$$\alpha = \frac{1}{k+1}. \tag{2.28}$$

The phase slip factor in scaling FFAG rings, thus given by:

$$\eta = \frac{1}{\gamma^2} - \frac{1}{k+1}, \tag{2.29}$$

is always non zero, except at the transition energy $\gamma_{tr} = \sqrt{k+1}$. Scaling FFAG are thus generally non-isochronous rings.

On the one hand, this non-isochronism is the source of longitudinal focusing, providing that η and thus the synchrotron tune ν_s are non-zero. One the other hand, the acceleration in such non-isochronous rings is usually achieved by sweeping the rf frequency to maintain the synchronization condition (Eq. 2.18), which is not suitable in the case of the fast acceleration of muon beams. Indeed, the possibility of changing rapidly the rf frequency with a reasonable amount of rf power requires rf cavities with a short time response, *i.e.* with a low quality factor, while a high quality factor is preferable to achieve high rf gradients required for rapid acceleration.

In this study two alternative acceleration methods are considered in order to use constant rf frequency in non-isochronous scaling FFAG rings. The

first one is based on the idea that, even if the ring is not isochronous, the synchrotron motion inside the area surrounding a stable fixed point of the longitudinal phase space can be used to accelerate particles. This is the principle of the so-called stationary bucket acceleration scheme discussed in the next chapter. In the second acceleration scheme considered, the idea is to maintain the synchronization condition given in Eq. 2.18 by changing the harmonic number by an integer number every turn. Particle thus jump every turn inside another stable area of the longitudinal phase space. This principle is called the harmonic number jump acceleration. Its application to the case of the muon acceleration in zero-chromatic FFAG rings is discussed in Chapter 4.

Chapter 3

Stationary bucket acceleration

The stationary bucket (SB) acceleration scheme has recently been proposed in Ref. [58]. In this chapter we proceed to a detailed study of this particular scheme.

After considering the longitudinal motion of particles inside the stationary bucket of a scaling FFAG ring, the relation between the achievable energy range and basic lattice parameters is exposed. A general study of the transverse acceptance in such a scheme, especially its dependence on the choice of the working point and the field index k, is then carried out. From the understanding of the achievable bucket height and transverse acceptance, it will be possible to identify suitable design parameters. The particular example of a 3.6 to 12.6 GeV scaling FFAG muon rings using this particular acceleration scheme is finally studied by means of step-wise particle tracking.

3.1 General considerations about SB acceleration

The principle of the SB acceleration is to increase the energy of particles making use of the synchrotron motion from the low energy part to the high energy part of a stationary rf bucket, as shown in Fig. 3.1. To that end, the bucket must be high enough to cover the required energy range. To study the achievable bucket height in such a scheme, one cannot adopt the classical approach of the synchrotron motion, as it is based on the assumption that the relative momentum variation is small [56]. it is indeed required that this variation is large, since the purpose is to increase the energy of particles by a significant amount.

Based on the fact that the momentum compaction factor α in scaling FFAGs is independent of momentum (see Eq. 2.28) the longitudinal Hamiltonian describing the motion inside a stationary rf bucket can be derived without approximation on the momentum variation. It has recently been proposed in Ref. [**?**], and is given by:

$$H(\phi,\gamma;\Theta) = h\left[\frac{1}{\alpha+1}\frac{\left(\gamma^2-1\right)^{\frac{\alpha+1}{2}}}{\gamma_s\left(\gamma_s^2-1\right)^{\frac{\alpha-1}{2}}} - \gamma\right] + \frac{eV_0}{2\pi mc^2}\cos\phi, \tag{3.1}$$

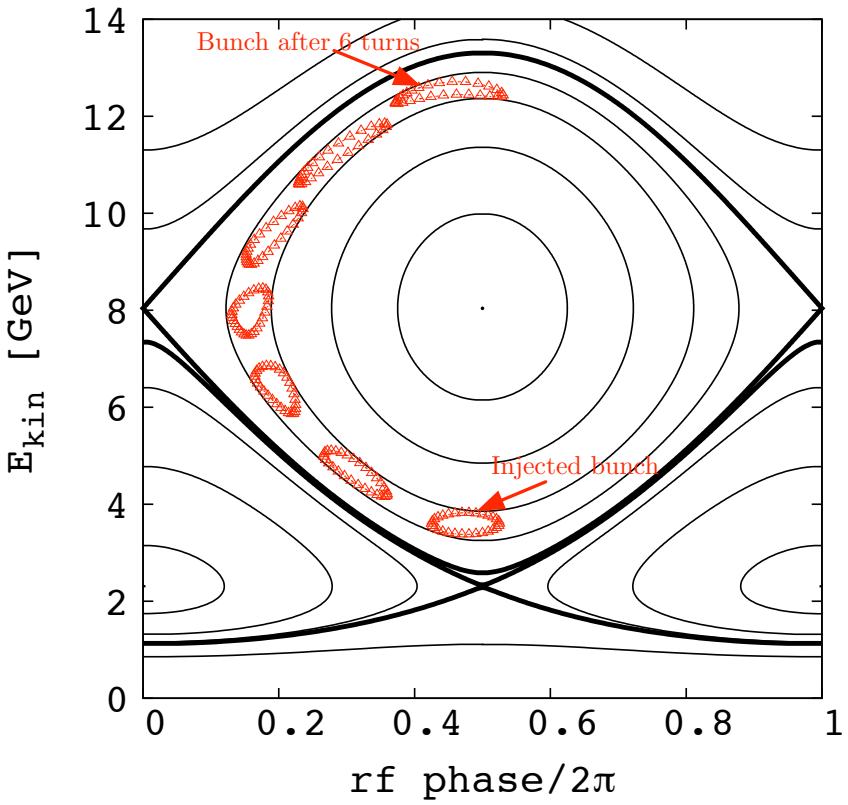

Figure 3.1: Longitudinal phase space showing the principle of SB acceleration of muons from about 3.6 to 12.6 GeV. Ring parameters are similar to the example detailed in Sec. 3.3.2. Black lines show hamiltonian contours calculated form Eq. 3.1. The red triangles shown the positions of particles plotted every turn, accelerated inside the above-transition stationary rf bucket, obtained from simple 2D longitudinal stepwise tracking.

where the canonical variables are the rf phase ϕ and the Lorentz factor γ of the particle. The independent variable is the azimuthal coordinate Θ. The particle charge is e, mc^2 is the particle rest mass, V_0 the sum over one turn of the rf cavities peak voltage, and h the harmonic number. Let γ_s be the Lorentz factor corresponding the the synchronous energy.

A derivation of this hamiltonian is proposed in App. A.2. Example of hamiltonian contours are plotted in Fig. 3.1. On this figure one can notice the existence of two stable fixed points surrounded by two distinct stable areas, called respectively the below-transition and the above-transition stationary buckets.

As we are concerned with the acceleration of high-energy muon beams, we consider the particular case of ultra-relativistic particles (γ and $\gamma_s \gg 1$)

accelerated in the above-transition rf bucket. The longitudinal Hamiltonian can then be approximated by:

$$\frac{1}{h\gamma_s} \cdot H(\phi, \gamma; \Theta) \simeq \frac{1}{\alpha+1}\left(\frac{\gamma}{\gamma_s}\right)^{\alpha+1} - \frac{\gamma}{\gamma_s} + \frac{v_0}{2\pi\gamma_s}\cos\phi, \tag{3.2}$$

where v_0 is a normalized rf voltage defined as:

$$v_0 = \frac{eV_0}{hmc^2}, \tag{3.3}$$

The right-hand side of Eq. 3.2 is a constant of motion, since neither γ_s nor h vary during acceleration. The maximum relative energy increase $\gamma_{max}/\gamma_{min}$ inside the rf bucket is then fully determined by two free parameters: the momentum compaction α (*i.e.* the field index k) and v_0/γ_s. Charts such as the one presented in Fig. 3.2, which shows how the height of the above-transition bucket depends on these two machine parameters, can then be obtained. As one can see on Fig. 3.2, large values of k and v_0/γ_s are preferable

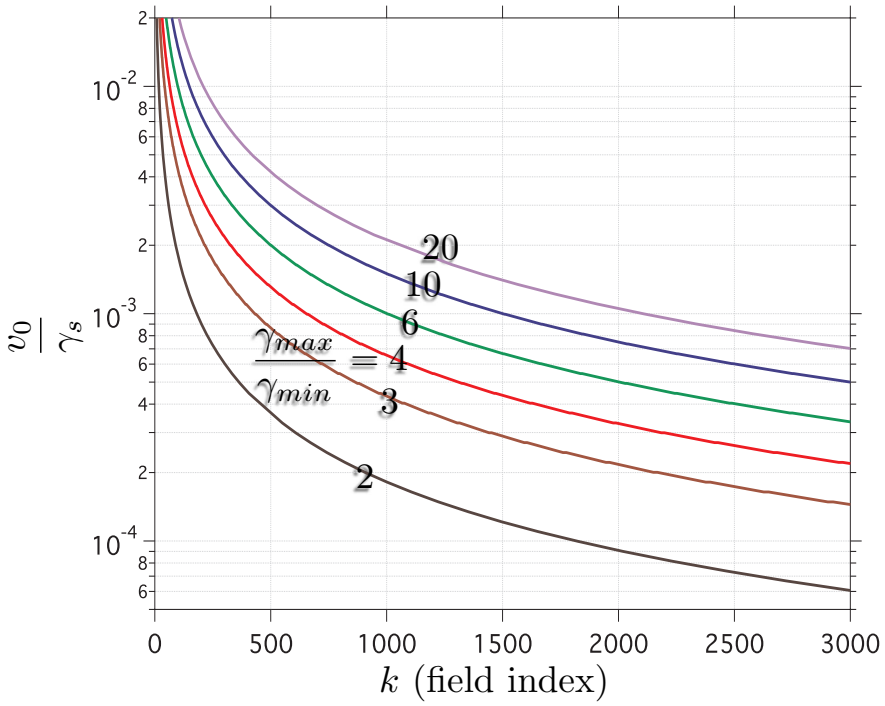

Figure 3.2: Maximum relative energy increase using acceleration inside the above-transition rf bucket of a scaling FFAG, function of the machine parameters k and $\frac{v_0}{\gamma_s}$.

to obtain larger bucket height.

The only ways to obtain high values v_0/γ_s once the energy range and the particle rest mass are given, are either to use a high rf voltage or a low harmonic number. On the one hand, one cannot choose arbitrary large rf voltages. It would indeed results in very large energy gain per turn, and then a very limited number of turns to complete the acceleration cycle, loosing at the limit the interest of using a circular structure. On the other hand, since the minimum rf frequency for the system to be compatible with the present baseline design is 200 MHz, the harmonic number can only be reduced decreasing the ring size. This requires basically stronger magnetic fields, which is also costly and technically limited by the performance of the superconducting types of magnets.

For these reasons, it is essential to consider the possibility of choosing high values of k. However the choice of the field index k is not only an essential parameter to determine the achievable bucket height, it also strongly constraints the transverse beam dynamics. In particular, the choice of a large k must not be done to the detriment of the large transverse acceptance required for the acceleration of the muon beams. It is thus essential to understand how to achieve large transverse acceptances while using large values of field index.

3.2 Effects of large k values on transverse beam dynamics

The variation of k may have two different types of consequences on the transverse beam dynamics: (i) the strength of non-linear field component is function of k, and (ii) the distance of the working point form the resonance lines may change when k is changed.

The approximate expression of the Taylor expansion of the field around a closed orbit in a scaling FFAG ring, given in Eq. 2.15, provides that the strength of the non-linear field components increase rapidly with k. For instance, once $k \gg 1$, the strength of the sextupole component is proportional to $(k/r_{co})^2$, the octupole component is proportional to $(k/r_{co})^3$, and so one.

To quantify the effect on the transverse acceptance of the increase in the strength of non-linear field itself, without being biased by other effects, we consider to varying k keeping r_{co}, ν_x, and ν_z constant, which is possible playing on the cell length (*i.e.* the ring periodicity). Such an approach, based on the canonical perturbation theory is presented in App. A.3. It provides that he transverse acceptance ϵ_{max} varies as with k as

$$\epsilon_{max} \propto \frac{1}{k^{3/2}}, \tag{3.4}$$

once r_{co}, ν_x, and ν_z are fixed. It is also shown that this expression is valid

for a large variety of working points.

Conversely, to understand the effect of the change in the distance of the working point from resonance condition, without being biased by the effect of variation of non-linear filed strength, tracking simulations are undertaken keeping k and r_{co} fixed, and changing the working point playing on the cell length. For simplicity reasons, we limit ourself to a study in one degree of freedom, *i.e.* without allowing vertical motion. Then, for each working point, the horizontal dynamic acceptance (DA) is estimated as described in App. B.2.4. Results of the simulation are presented in Fig. 3.3. On this

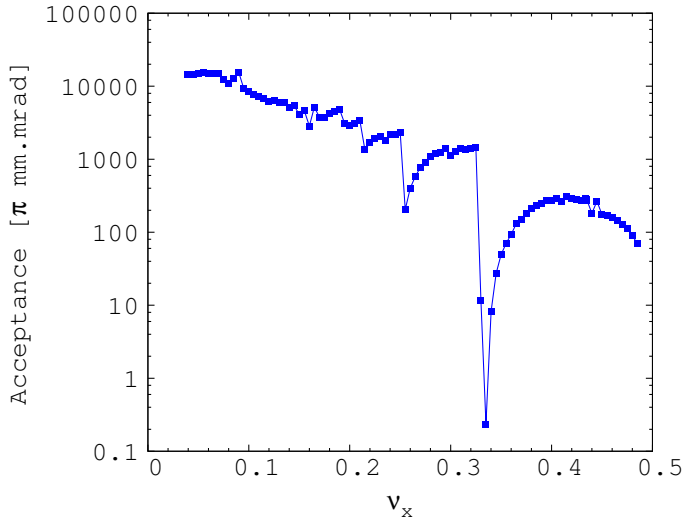

Figure 3.3: Variation of horizontal dynamic aperture with respect to the horizontal tune per cell, obtained from tracking simulations (without allowing vertical motion). The value of k is fixed and equal to 700. The cell structure assumed is F-D-F. The cell geometry is similar for each working point studied, *i.e.* the magnet size, position and fringe field extend are scaled in proportion with the cell length. The value of the closed orbit radius, measured at the center of the drift between F magnets is kept fixed and equal to 100 m.

picture one can clearly see sharp drops of DA corresponding to the effect of the third order ($\nu_x = 1/3$), the fourth order ($\nu_x = 1/4$) and, to a lesser extent, the fifth order ($\nu_x = 1/5$) resonances. One can also notice that it is essential to choose low values of cell tune to achieve very large transverse acceptances.

In summary, the effect of k on the position of the working point can fully be compensated by a proper choice of the ring periodicity, *i.e.* a proper choice of the cell tunes. However the effect of k due to the increase in non-linear field strength is unavoidable, and lead to a dependence like $k^{-3/2}$ of the DA.

3.3 Example of a 3.6 to 12.6 GeV muon rings

3.3.1 Choice of cell parameters

Since the aim is to design a lattice with a high k value, *i.e.* providing a very strong horizontal focusing, impractically large values of spiral angle would be required to ensure vertical stability. This is why the radial type of scaling FFAG is considered in this section. In this case, the F-D-F triplet structure is preferable to the D-F-D one, since slightly larger k values are achieved for a given working point with the F-D-F structure. This is explained by the fact that all edges are horizontally defocusing in this structure, but not in the other one (see App. B.1).

Next, to help in the choice of the the working point, we developed a procedure producing transverse acceptances scan in the region of the tune diagram surrounding a reference working point. To scan an area in the tune diagram, we move from a working point to another by varying the value of the field index k as well as the ratio between D and F magnets strength. However, the cell geometry (*i.e.* position and size of the magnets) is kept unchanged. For each working point considered, particle tracking at fixed energy is used to estimate horizontal and vertical acceptances, as described in App. B.2.4. Results obtained in the case of a ring made of 225 identical F-D-F triplet cells, in the region around ($\nu_x = 0.27$, $\nu_z = 0.15$), are presented in Fig. 3.5. The position of the working points presented in this figure are also shown plotted in the parameters space (k, BL_D/BL_F) in Fig. 3.4. The boundaries of the stability area are also presented on this figure. Here BL_D/BL_F represents the radio between the D and F magnet field integrals calculated along an arc centered on the machine center.

This figure shows a strong relation between the acceptances and the position of the working point with respect to normal structure resonance lines. This type of resonance is indeed the only one excited by the scaling FFAG magnet field without errors. In Fig. 3.5 one can thus notice that:

- The one-dimension resonances $\nu_x = 1/3$ and $\nu_x = 1/4$ affect strongly the horizontal acceptance, however this effect is not the same on both sides of the resonance lines. This can be explained considering the non-linear detuning which tends here to decrease the horizontal tune of particles with large amplitude motion, limiting the acceptance at working points located on the right of these resonances lines.

- The octupule sum resonance $2\nu_x + 2\nu_z = 1$ affects significantly both horizontal and vertical acceptances. As a sum resonance, it causes emittance growth in both planes simultaneously [54] and must therefore be avoided.

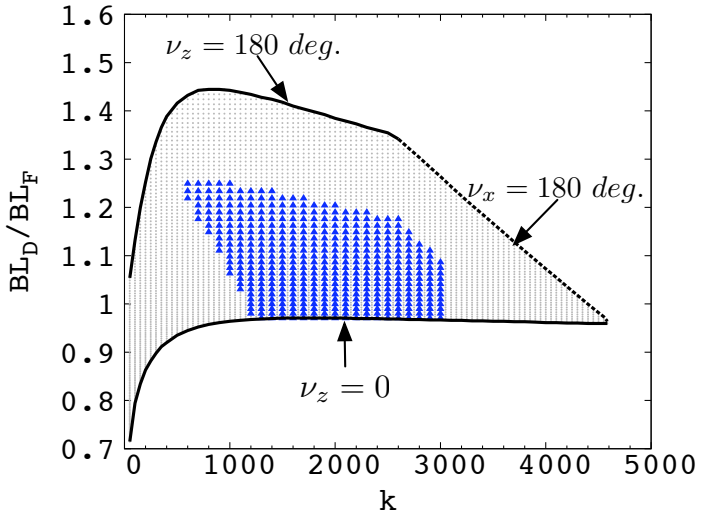

Figure 3.4: Stability area plotted in the parameters space (k, BL_D/BL_F). This area is filled with small gray dots and is delimitated by three lines: the solid lines corresponds to a vertical phase advance per cell equal to either 0 or 180 deg., while the dotted line corresponds to an horizontal phase advance per cell of 180 deg. The position of the points for which the transverse amplitude has been studied and presented in Fig.3.5 are superimposed (blue triangles).

- The difference resonances ($\nu_x - 2\nu_z = 0$ and $2\nu_x - 2\nu_z = 0$) are not always harmful. In this case, emittances are indeed exchanged between planes, and necessarily remain finite [54].

Considering together the choice of the working point with the constraints related to the longitudinal motion discussed at the beginning of this section, we are from now on able to choose suitable ring parameters.

3.3.2 Details of ring parameters

Let's now examine the example of the 3.6 to 12.6 GeV muon ring with parameters given in Tab. 3.1. It is assumed to use scaling FFAG magnets with a maximum field less than about 5 T. It is a reasonable assumption once superconducting magnets with left-right asymmetrical coil distribution [59] are employed to realize the scaling field law.

In order to allow the simultaneous acceleration of μ^+ and μ^- beams, the distance between rf cavity gaps cannot be arbitrarily chosen. It must be adjusted so that the path length of the synchronous particle between rf gaps is a multiple of $\frac{1}{2}\beta_s\lambda_{rf}$, with β_s the ratio of the synchronous particle velocity

Table 3.1: Muon ring parameters.

Lattice type	scaling FFAG FDF triplet
Injection/extraction kinetic energy	3.6/12.6 GeV
rf frequency	200 MHz
Mean radius	$\sim$ 161 m
Synchronous kinetic energy	8.04 GeV
Harmonic number h	675
Number of cells	225
Field index k	1390
Peak rf voltage (per turn)	1.8 GV
Number of turns	6
B_{max} (on closed orbit at 12.6 GeV)	3.9 T
Drift length	$\sim$ 1.5 m
Horizontal phase advance per cell	85.86 deg.
Vertical phase advance per cell	33.81 deg.
Excursion	14.3 cm

to the speed of light, and λ_{rf} the rf wavelength. In our design, the length of the triplet cell is thus adjusted so that the path length of the synchronous particle through each cell is $3 \cdot \beta_s \lambda_{rf}$.

3.4 Tracking simulations

To study lattice parameters and beam dynamics, we use a stepwise tracking code based on Runge-Kutta integration developed during this study. Results of cross-check with the tracking code Zgoubi [30] are also presented in this section. In our code like with the 'FFAG' procedure [60] of Zgoubi, we use a field distribution in the magnet mid-plane that follows the form:

$$B_z(r,\theta) = B_{z0}\,\mathcal{R}(r)\,\mathcal{F}(\theta), \tag{3.5}$$

with r the distance from the machine center and θ the azimuthal coordinate. The radial field law $\mathcal{R}(r)$ is proportional to r^k. The flutter $\mathcal{F}(\theta)$ is softened using Enge type of field fall-off [61]. Coefficients of the Enge distribution have been determined from a fit of field fall-off of a finite element model of the RACCAM prototype magnet [28]. With both codes, the field off the mid-plane is obtained, satisfying the Maxwell's equations, from a 4^{th} order Taylor expansion.

The phase advances given in Tab. 3.1 are obtained from stepwise tracking with small amplitude motion. Similar results are found between our code and

Zgoubi: position of the closed orbit is identical within a precision better than 10^{-5} m, values for the phase advance are identical within a relative precision better than 10^{-4}. Vertical component of the magnetic field along the closed orbits for 3.6, 8.0 and 12.6 GeV is plotted in Fig. 3.6. The beta functions presented in Fig. 3.7 are obtained with our code from particle tracking with small amplitude motion.

3.4.1 Transverse acceptance studied at fixed energy

To determine the horizontal acceptance at fixed energy of the lattice described in Tab. 3.1, 3.6 GeV muons are tracked through 1350 triplet cells (*i.e.* 6 turns). Particles are launched with 1 mm initial vertical displacement and various initial horizontal displacements. Result of particle tracking obtained with our code, and with Zgoubi, are presented in Fig. 3.9. These horizontal phase space plots show the positions of a particle close to the largest stable amplitude over 6 turns, as well as the positions of a particle with a lower amplitude. Both codes agree on a value of a normalized horizontal acceptance larger than 30 πmm.rad.

A similar approach is used to determine the vertical acceptance. Results are presented in Fig. 3.8. Both codes agree on a value of a normalized vertical acceptance of about 30 πmm.rad.

3.4.2 6D Simulation of a whole acceleration cycle

The acceleration of a 6D bunch of particles inside the stationary rf bucket of the ring described in Tab. 3.1 has been simulated using our tracking code. The bunch of particles is prepared as follows: 1000 particles are uniformly distributed inside a transverse 4D ellipsoid (Waterbag distribution); these particles are then independently distributed uniformly inside an ellipse in the longitudinal plane. Initial normalized bunch emittances are 30 πmm.rad in both horizontal and vertical planes and 150 mm in the longitudinal plane. Normalized emittances are defined in a similar way than in Ref. [45]. An rf kick that simulates the effect of a zero length rf cavity with 8 MV peak voltage is given in the middle of the long drift of every triplet cell.

Simulation results are presented in Figs. 3.10, 3.11, 3.12, 3.13, and 3.14. The decrease of the beam area visible in Figs. 3.11 and 3.13 is due to acceleration dumping. No significant emittance blow-up is observed in the longitudinal phase space (see Fig. 3.10).

3.4.3 Tracking with errors

The sensitivity to errors of this scheme is studied by introducing alignment errors. Let's consider first of all errors in the form of a translation of each triplet cell. The direction of the displacement is randomly and uniformly chosen in the 3D space. The amplitude of the displacement is chosen following a normal (Gaussian) distribution with null mean. Direction and amplitude of the displacement are chosen once for each of the 225 ring cells at the beginning of each simulation. Simulations proceed as follows: 200 particles chosen randomly in the same way than described in Sec. 3.4.2 are tracked over a whole acceleration cycle. Collimators placed in the middle of every long straight section stop particles going at $r < 160.7$ m, $r > 161.1$ m, and $|z| > 90$ mm. The number of surviving particles for several values of rms displacement amplitude obtained with 8×20 simulations with different initial distribution of the errors is presented in Fig. 3.15.

The same study using errors in the form of rotation around an axis passing by the triplet center (at $r = 160.9$ m), with a direction and an angle chosen in a similar way has been carried out. Results are presented in Fig. 3.16.

These two figures show that the effect of alignment errors on the machine acceptance is negligible for rms alignment errors smaller than about 1 mm in translation and 0.5 mrad in rotation.

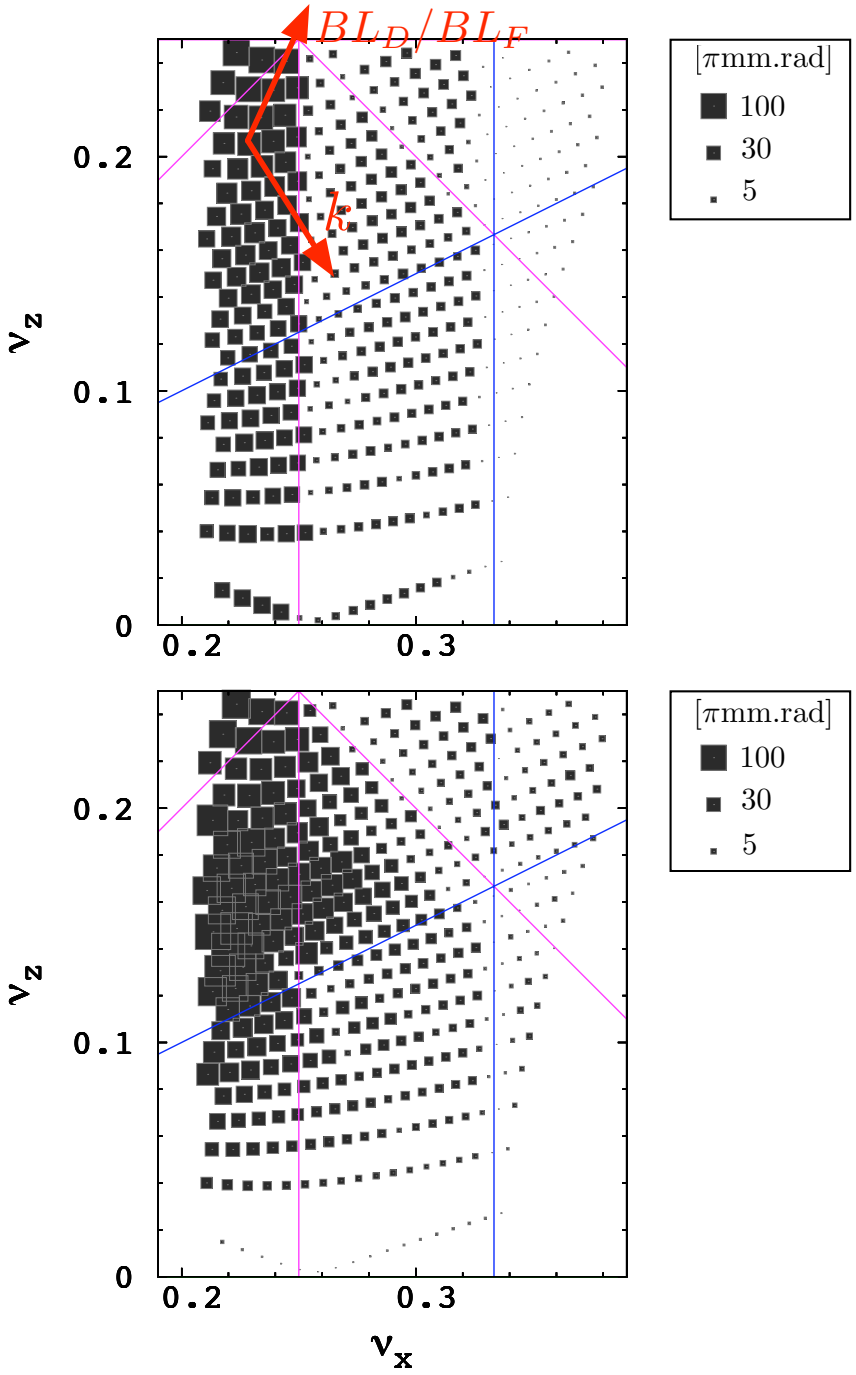

Figure 3.5: Result of a scan showing the horizontal (top) and vertical (bottom) acceptances for various positions in the one-cell tune diagram. The area of each square is proportional to the transverse (either horizontal or vertical) acceptance estimated as described in App. B.2.4. Legends in the top left corners give values of acceptances normalized for 3.6 GeV muons. Normal structure resonances lines, plotted up to the octupole, are superimposed.

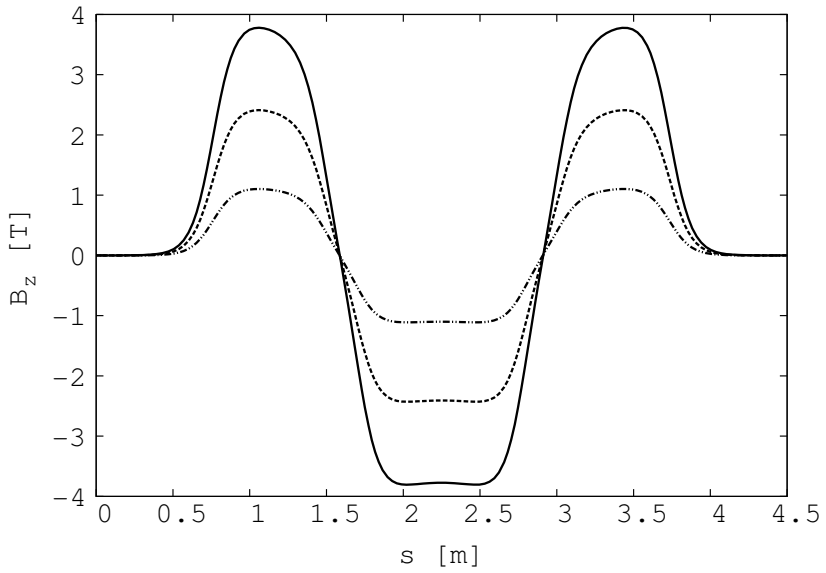

Figure 3.6: Vertical component of the magnetic field along the closed orbits at 3.6 GeV (dot-dashed line), 8.0 GeV (dotted line) and 12.6 GeV (solid line).

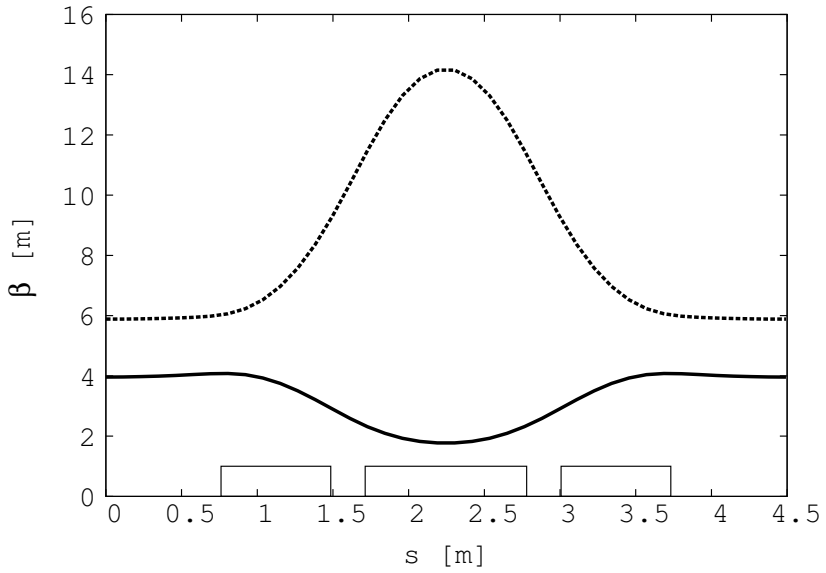

Figure 3.7: Horizontal (bold solid line) and vertical (dotted line) beta functions of a periodic cell. Rectangles in the bottom of the plot show the position of the magnets effective field boundaries.

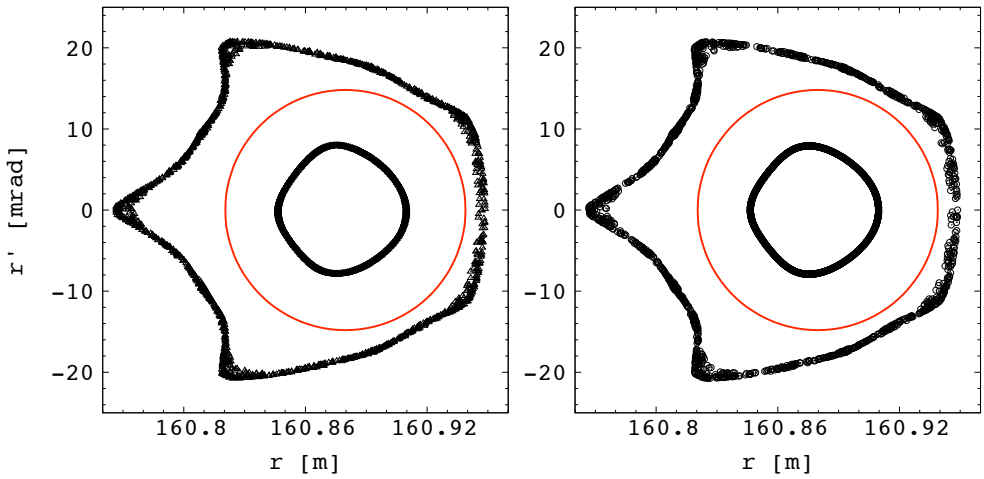

Figure 3.8: Horizontal (r,r') phase space plots, looking at the middle of long drifts, showing positions of two particles launched with different initial horizontal amplitudes, and with a 1 mm initial vertical displacement, tracked over 1350 cells. Results obtained with our code (right part) and with Zgoubi (left part) are presented. The area of the red ellipse superimposed corresponds to 30,000 π.mm.mrad normalized.

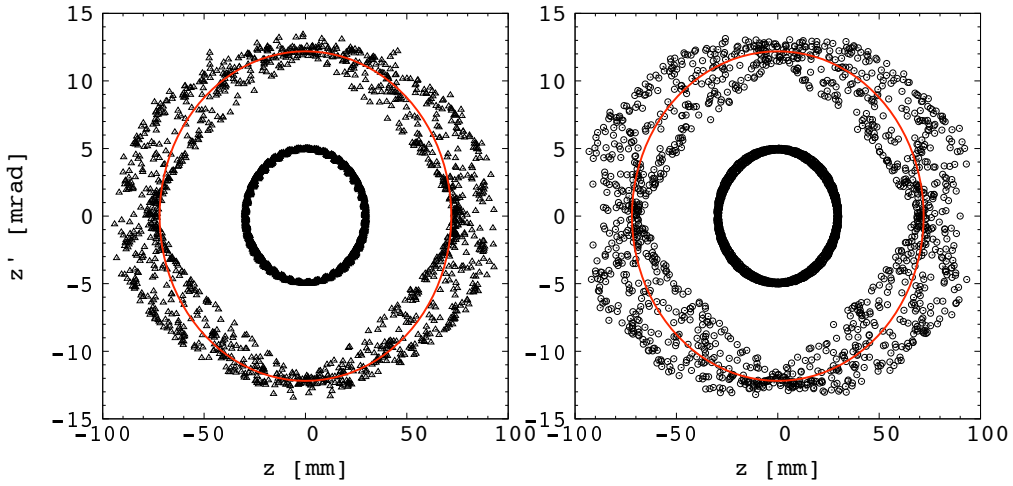

Figure 3.9: Vertical (z,z') phase space plots, looking at the middle of long drifts, showing positions of two particles launched with different initial vertical amplitudes, and with a 1 mm initial horizontal displacement, tracked over 1350 cells. Results obtained with our code (right part) and with Zgoubi (left part) are presented. The area of the red ellipse superimposed corresponds to 30,000 π.mm.mrad normalized.

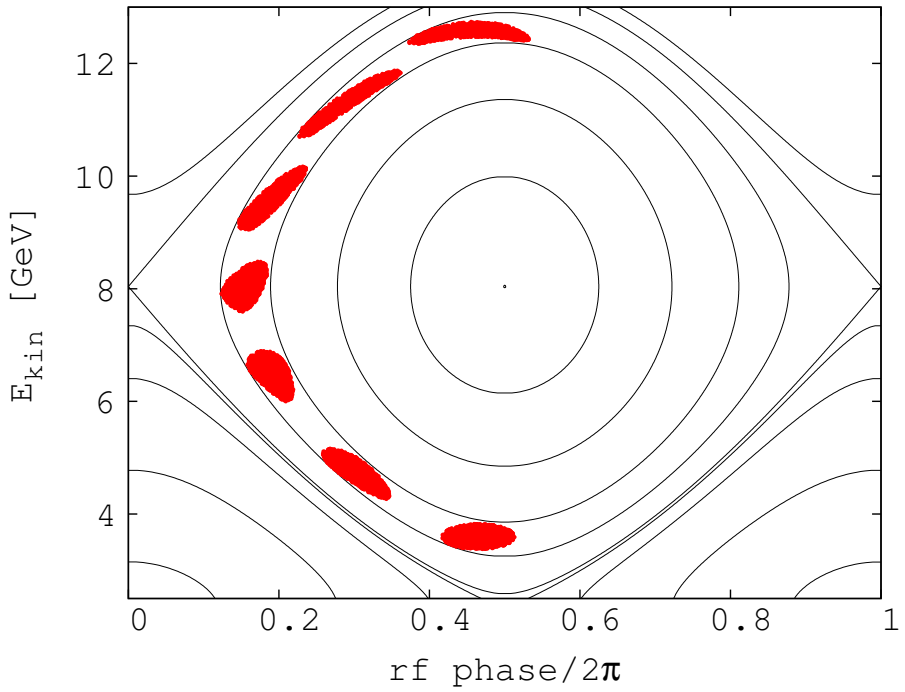

Figure 3.10: 6-turn acceleration cycle plotted in the longitudinal phase space. Hamiltonian contours obtained from Eq. 3.1 are superimposed.

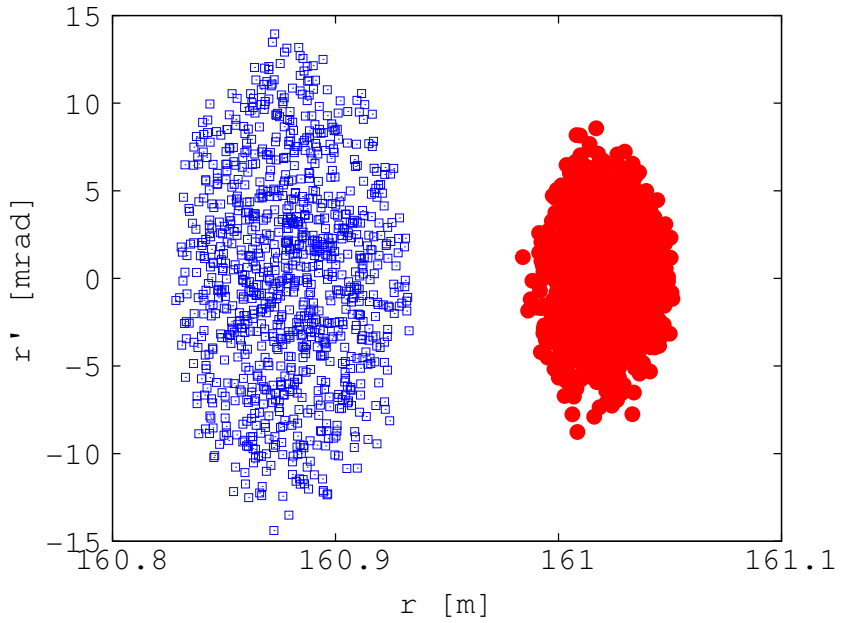

Figure 3.11: Initial (blue squares) and final (red dots) particles positions plotted in the horizontal (r,r') phase space.

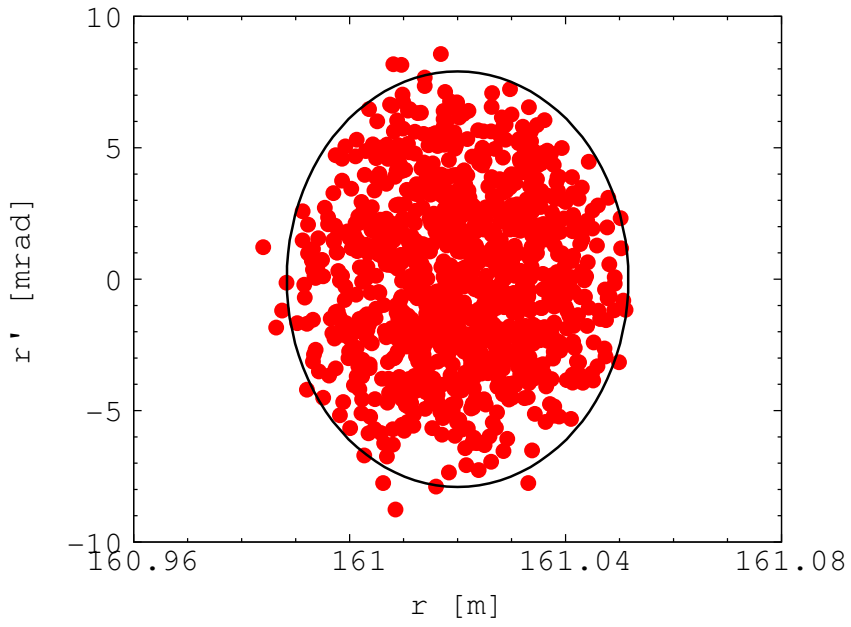

Figure 3.12: Practically, all particles are lying inside an the expected area in the horizontal phase space, the area of black ellipse shown on this plot corresponds to 30,000 π.mm.mrad normalized for 12.6 GeV muons.

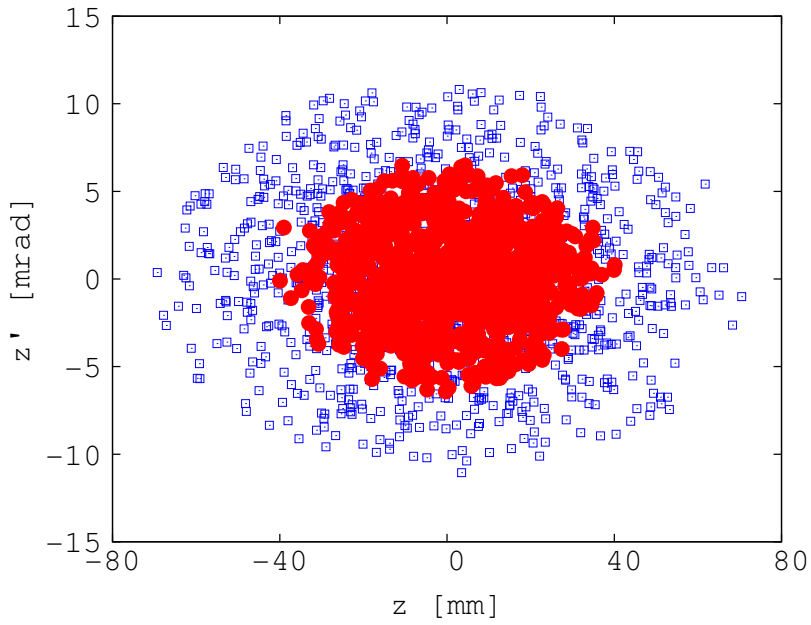

Figure 3.13: Initial (blue squares) and final (red dots) particles positions plotted in the vertical (z,z') phase space.

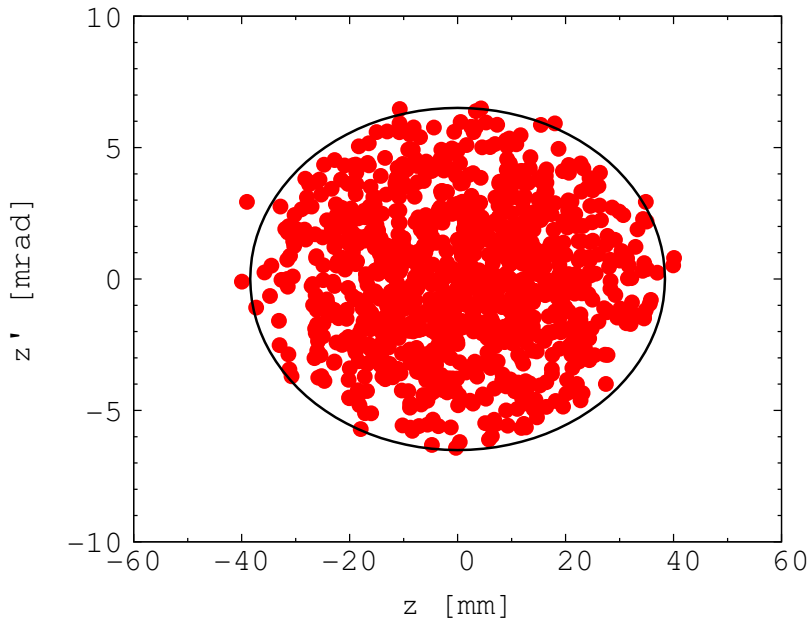

Figure 3.14: Similar plot than Fig. 3.12. In the vertical phase space also, practically all particles are lying inside an the expected area.

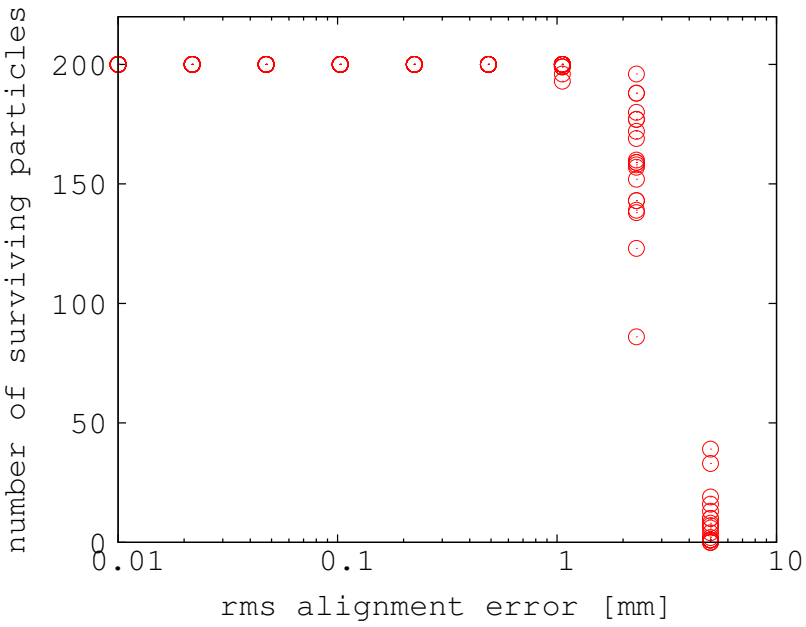

Figure 3.15: Number of surviving particles function of rms alignment error in translation.

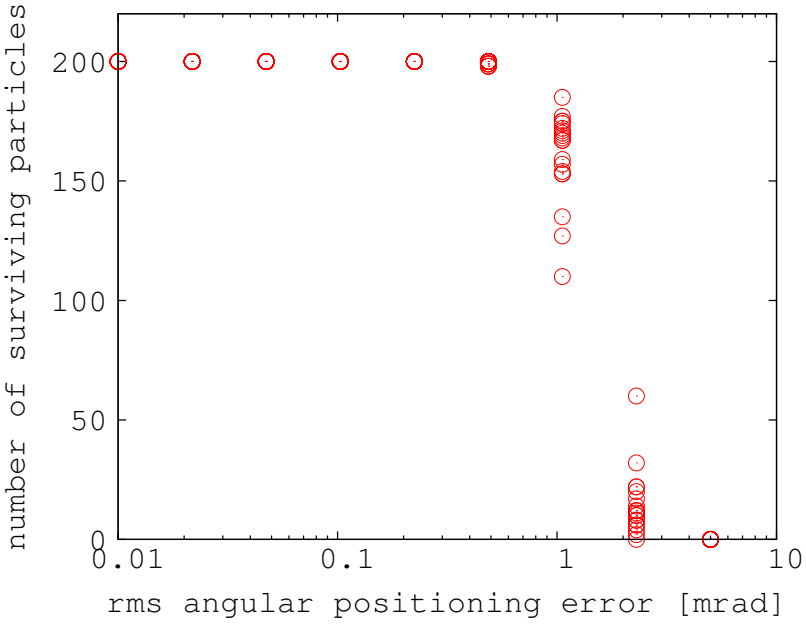

Figure 3.16: Number of surviving particles function of rms alignment error in rotation.

Chapter 4

Harmonic number jump acceleration

The application of the harmonic number jump scheme to the acceleration of muon beams in scaling FFAG rings is studied in this chapter. The essential properties of this acceleration methods and the strong constraints they impose of the lattice design are exposed. An new type of zero-chromatic FFAG lattice including insertions is presented as a way to satisfy these constraints. We thus undertake the design of a 3.6 to 12.6 GeV zero-chromatic FFAG muon ring. The 6D beam dynamics in this particular ring example is finally studied by means of step-wise particle tracking.

4.1 General considerations about harmonic number jump acceleration

Let's recall here the condition of synchronization between the revolution frequency f_{rev} of a particle and the frequency of oscillation of the rf field f_{rf} given in Eq. 2.18:

$$f_{rf} = h \cdot f_{rev},$$

where h is an integer called the harmonic number.

The principle of the HNJ acceleration is to maintain this synchronization condition in a non-isochronous ring by changing the harmonic number h of an integer number every turn. This way the rf frequency can be kept constant. To that end, one must give the right energy gain to change the revolution period of an integer number of rf period every turn. This principle has been proposed [62] and first used [63] in machines now referred as microtrons, in which ultra-relativistic particles can be accelerated in circular structures using a static and radially constant magnetic field. The use of this acceleration principles in other types of fixed field machines has recently be re-considered [64, 65]. The purpose of this chapter is to study the implementation of this principle into a particular kind of non-isochronous ring, the scaling type of FFAGs.

4.1.1 Required energy gain per turn

Examine first the simple case of a ring with a single rf kick given at the beginning of each turn. Let E_i be the energy of the particle during the turn number i, and $T(E_i)$ the revolution time of this particle. Choosing the rf frequency such as:

$$f_{rf} = \frac{h_i}{T(E_i)} \qquad h_i \in \mathbb{N}, \tag{4.1}$$

the condition to jump an integer number $\Delta_i h$ of harmonic(s) between the turns i and $i+1$ can be written as:

$$T(E_{i+1}) - T(E_i) = \frac{\Delta_i h}{f_{rf}}. \tag{4.2}$$

We use here an approach based on Ref. [65]. However, to apply this approach to the case of scaling FFAGs, it is essential to be able to take into account the non-linear variation of the time of flight over large energy ranges. For this purpose we proceed to a piecewise linearization of T around the energy of the particle at the beginning of each turn. One can write then:

$$T(E_{i+1}) = T(E_i) + (E_{i+1} - E_i) \cdot \left.\frac{\partial T}{\partial E}\right|_{E_i}. \tag{4.3}$$

The required energy gain for harmonic number jump is obtained combining Eqs. 4.2 and 4.3:

$$E_{i+1} - E_i = \frac{\Delta_i h}{f_{rf} \cdot \left.\frac{\partial T}{\partial E}\right|_{E_i}}. \tag{4.4}$$

4.1.2 Ring with many rf cavities

We now consider the use of HNJ acceleration in a ring with N rf cavities uniformly distributed around (see Fig. 4.1). We extend here the approach described in Ref. [65], taking into account the non-linear variation of the time of flight and considering the localized nature of rf gaps.

Let $E_{i,j}$ be the energy of a given reference particle right before it crosses the cavity number j during the turn number i. The function $T(E_{i,j})$ is henceforth a function of the position j around the ring. The time taken by the particle to do a whole turn, starting from the cavity number j, is not $T(E_{i,j})$ anymore, but can be written as the sum over one turn of the times of flight between every single cavity:

$$\mathfrak{T}_{i,j} = \sum_{k=1}^{N-j} \frac{T(E_{i,j+k})}{N} + \sum_{k=1}^{j} \frac{T(E_{i+1,k})}{N}. \tag{4.5}$$

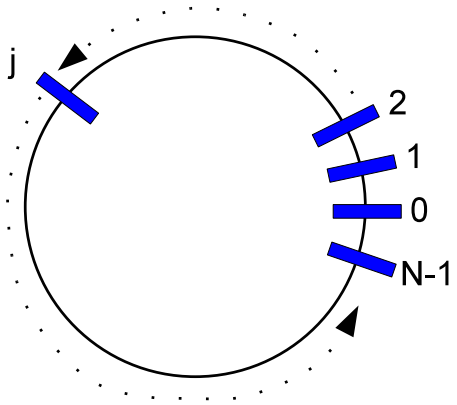

Figure 4.1: N cavities (numbered 0 to N-1) uniformly distributed around a circular ring.

If one wants to cross the rf cavity number j with the same rf phase every turn, its frequency $f_{i,j}$ must follow:

$$f_{i,j} = \frac{h_i}{\mathfrak{T}_{i,j}}, \tag{4.6}$$

with h_i the harmonic number for turn number i. To determine $f_{i,j}$ one must first of all express $\mathfrak{T}_{i,j}$.

For this purpose we choose $\Delta_i h$ independent of the turn number i, and we assume that the energy gain per turn of this reference particle follows Eq. 4.4:

$$E_{i+1,0} - E_{i,0} = \frac{\Delta h}{f_{ref}\ \frac{\partial T}{\partial E}\big|_{E_{i,0}}}. \tag{4.7}$$

With this assumption, the reference frequency f_{ref} is independent of the turn number i and satisfies:

$$f_{ref} = \frac{h_i}{T(E_{i,0})} \qquad \text{with} \qquad h_i = h_0 + i \cdot \Delta h. \tag{4.8}$$

Let's also assume that the energy gain is uniformly shared between cavities, which means that the energy gain per cavity is given by:

$$\delta E_{i,j} = \delta E_i = \frac{1}{N} \cdot \frac{\Delta h}{f_{ref}\ \frac{\partial T}{\partial E}\big|_{E_{i,0}}}, \tag{4.9}$$

We next proceed do a piecewise linearization of T around the energy of the particle at the beginning of each turn. It gives:

$$T(E_{i,j}) = T(E_{i,0}) + j \cdot \delta E_i \left.\frac{\partial T}{\partial E}\right|_{E_{i,0}}. \tag{4.10}$$

Combining Eqs. 4.5, 4.9, and 4.10 one gets:

$$\mathfrak{T}_{i,j} = \mathfrak{T}_{i,0} + \frac{j}{N}(T(E_{i+1,0}) - T(E_{i,0})), \tag{4.11}$$

where $\mathfrak{T}_{i,0}$ is given by:

$$\mathfrak{T}_{i,0} = T(E_{i,0}) + \frac{N+1}{2N} \cdot \frac{\Delta h}{f_{ref}}. \tag{4.12}$$

Using Eq. 4.8, one gets the following expression for $T(E_{i+1,0})$:

$$T(E_{i+1,0}) = T(E_{i,0}) \cdot \frac{h_i + \Delta h}{h_i}. \tag{4.13}$$

One thus can rewrite Eq. 4.11 in order to express $\mathfrak{T}_{i,j}$ as:

$$\mathfrak{T}_{i,j} = \mathfrak{T}_{i,0} + \frac{j}{N}\frac{\Delta h}{h_i} \cdot T(E_{i,0}). \tag{4.14}$$

The expression of $\mathfrak{T}_{i,j}$ in Eq. 4.14, used together with Eqs. 4.5 and 4.6, provides:

$$f_{i,j} = \frac{f_{ref}}{1 + \frac{2j+N+1}{2N} \cdot \frac{\Delta h}{h_i}}. \tag{4.15}$$

One may now remark that, as long as h_i is large and much larger than its variation during the acceleration cycle (*i.e.* $h_i \simeq h_0$), $f_{i,j}$ is independent of the turn number i and can be written as:

$$\boxed{f_j \simeq f_{ref}\left[1 - \frac{\Delta h}{h_0} \cdot \left(\frac{2j+1}{2N} + \frac{1}{2}\right)\right]} \tag{4.16}$$

Under these conditions, every cavity can work at constant frequency, but each frequency must be tuned at a slightly different frequency.

Since the frequency of each cavity is a monotonic function of its position j around the ring, acceleration is only possible in one direction of rotation when $N \leq 2$. If one wants to accelerate charged particles and their antiparticles simultaneously in the same ring, they must all circulate in the same direction.

4.1.3 Required excursion when accelerating ultra-relativistic particles

When HNJ is used to accelerate ultra-relativistic particles, the required variation of time of flight only comes from the variation of path length between each turn:

$$T(E_{i+1}) - T(E_i) = \frac{\Delta_i C}{c}, \tag{4.17}$$

where the particle velocity is assumed equal to the speed of light c, and $\Delta_i C$ is the variation of orbit circumference between turns i and $i+1$. Let's define the average orbit excursion between turns i and $i+1$ as:

$$\Delta_i R = \frac{\Delta_i C}{2\pi}. \tag{4.18}$$

Combining Eq. 4.17 with the required change in time of flight for harmonic number jump given in Eq. 4.2, one can get the required average excursion:

$$\Delta_i R = \Delta_i h \cdot \frac{\lambda_{rf}}{2\pi}, \tag{4.19}$$

where λ_{rf} is the rf wavelength defined as:

$$\lambda_{rf} = \frac{c}{f_{rf}}. \tag{4.20}$$

The rf wavelength is a parameter which, for a given geometry of the rf cavity, determines its size. For instance, in the simple case of a pillbox type rf cavity, its diameter d is approximately given by $d = 0.77\lambda_{rf}$ [66].

In case the acceleration is done over a number of turns N_t, with exactly one harmonic jump each turn, the average excursion from injection to extraction is then given by:

$$\text{total average orbit excursion} = \frac{N_t}{2\pi} \cdot \lambda_{rf}. \tag{4.21}$$

Thus, whatever the choice of the rf frequency, if the number of turns is larger than 5 the average excursion is necessarily larger than the diameter of a pillbox type rf cavity. Cavity design issues could thus drastically limit the achievable number of turns. To avoid this problem, one can vary the excursion along the ring, introducing reduced excursion insertions in which cavities could be installed.

4.2 Development of advanced zero-chromatic FFAG lattices

4.2.1 Reduce excursion insertions

To reduce the excursion at locations where rf cavities can be installed, let's consider the design of reduced excursion insertion in scaling FFAG rings. Such insertions can equally be seen as dispersion suppressors. At a given azimuth Θ around the ring, the excursion is indeed an integral expression of the periodic dispersion $\eta(\Theta)$:

$$\Delta_{p_1 \to p_2} R(\Theta) = \int_{p_1}^{p_2} \frac{\eta(\Theta)}{p} \mathrm{d}p, \tag{4.22}$$

where $\Delta_{p_1 \to p_2} R(\Theta)$ is the excursion measured between two arbitrary momentums p_1 and p_2.

Until recently, very few work have been dedicated to the study of possible insertions in FFAG lattices. A couple of design principle have nevertheless been described by Meads in 1983 [67] and 1993 [68], and were used as a starting point in this study. To achieve a significant amount of reduction in the orbit excursion, while keeping the zero-chromatic properties of the ring over the whole energy range, we however developed a new type of insertion constituted only of scaling type of FFAG magnets.

Before looking at the ring with insertions as a whole, it is useful to consider each type of cell separately. For a given momentum p, let's thus define the "reference orbit" of each cell as the orbit followed by a particle which enters and exits the cell with the same transverse coordinates (r,z) and angles (r',z') with respect to the azimuthal vector.

The excursion can be reduced by introducing, in a scaling FFAG ring made of cells with a field index k_1, two types of scaling FFAG cells with field indices k_2 and k_3 respectively. A schematic view of such an insertion is presented in Fig. 4.2. Reference orbits of this three type of cells are matched

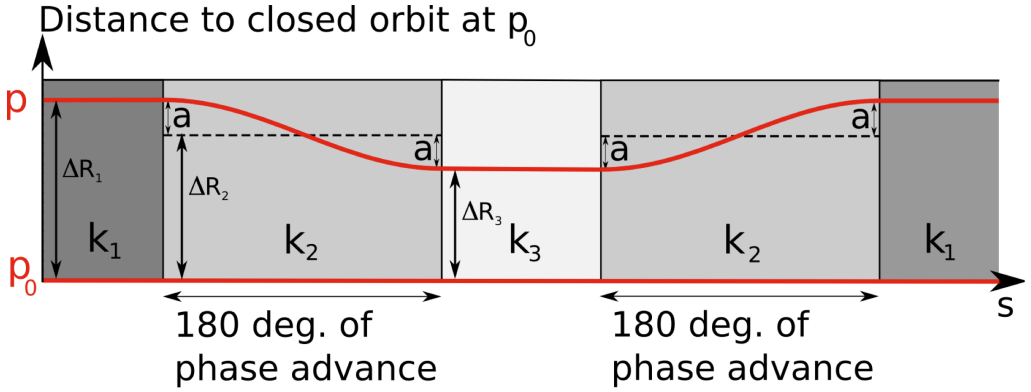

Figure 4.2: Schematic view of an excursion reduced insertion made of scaling FFAG cells.

at a given momentum p_0. The field indices k_1, k_2, and k_3 are chosen so that, for any momentum p:

$$\Delta R_1 - \Delta R_3 = 2 \cdot a = 2 \cdot (\Delta R_1 - \Delta R_2), \tag{4.23}$$

with a, ΔR_1, ΔR_2, and ΔR_3 as defined in Fig. 4.2. Let's now consider the exact relation in scaling FFAG cells:

$$p = p_0 \cdot \left(\frac{R}{R_0} \right)^{k+1}, \tag{4.24}$$

with R the reference orbit radius for the momentum p, and R_0 the reference orbit radius for the given momentum p_0. In our case, this may be re-written as:

$$p = p_0 \cdot \left(\frac{R_0 + \Delta R_i}{R_0} \right)^{k_i+1}, \qquad i = \{1, 2, 3\}. \tag{4.25}$$

Expanding it to first order in $\frac{\Delta R_i}{R_0}$ and using Eq. 4.23, one gets the relation between k_1, k_2, and k_3:

$$\frac{2}{k_2 + 1} = \frac{1}{k_1 + 1} + \frac{1}{k_3 + 1}. \tag{4.26}$$

The first order expansion in $\frac{\Delta R_i}{R_0}$ implies that this approach is valid as long as the maximum excursion is much smaller than the machine radius. In the present case, since we are dealing with large rings for which the machine radius is much larger than the orbit excursion, this condition is always valid.

For a momentum different from the reference momentum p_0, a mismatch appears in the positions of the reference orbits between the different types of cells. This mismatches induces a perturbation of the closed orbit shape, which can be seen as a coherent betatron oscillation around the reference orbit of the k_2 cells. Following the linear approach of the motion around this reference orbit one notice that, if the section made of k_2 cells has a horizontal phase advance of 180 degree, the closed orbit deformation is in the form of a half betatron oscillation. This way, the resulting closed orbit merges with the reference orbits in the sections made of k_1 and k_3 cells. The excursion is thus reduced by a factor of $\frac{k_3+1}{k_1+1}$.

The linear approach also provides that the phase advance calculated around the perturbed closed orbit is the same than the phase advance calculated around the reference orbits. The last one being independent of the particle energy, since the dispersion suppressor is made of scaling FFAG cells, this whole system remains zero-chromatic.

The principle of such an excursion suppressor relies on a linear approach of the motion around the reference orbit of the section made of k_2 cells. This principle is valid for any momentum, as long as the effect of non-linear field components is negligible.

4.2.2 Minimize the effect of non-linearities

Scaling FFAG magnets are generally source of non-linear field components, which may affect what is described as a half betatron oscillation around the reference orbit of the k_2 cells. This effect is negligible when the amplitude of the oscillation is small, and naturally increases with the amplitude of the oscillation. The amplitude of this oscillation can be measured by the

horizontal Courant-Snyder invariant:

$$U = \tilde{\gamma}x^2 + 2\tilde{\alpha}xx' + \tilde{\beta}x'^2, \tag{4.27}$$

where x is the distance and x' the angle with respect to the reference orbit. In the same way the reference orbit of a cell has been defined, let's introduce the "reference Twiss parameters" of each cell as the periodic Twiss parameters calculated around the reference orbit. The notations $\tilde{\alpha}$, $\tilde{\beta}$ and $\tilde{\gamma}$ are used to distinguish the reference Twiss parameters of a cell, from the periodic Twiss parameters α, β and γ of the ring.

Since at the entrance of the dispersion suppressor there is a position mismatch a and no angular mismatch, the corresponding horizontal invariant is given by:

$$U = a^2\ \tilde{\gamma}, \tag{4.28}$$

with $\tilde{\gamma}$ the value of the horizontal reference Twiss parameter $\tilde{\gamma}$ at the entrance of the dispersion suppressor.

Thus, for a given value of a, one can minimize the invariant U, and thus the effect of non-linearities, by choosing the entrance of the dispersion suppressor at a minimum of its horizontal $\tilde{\gamma}$-function.

4.2.3 Non-round ring made of scaling FFAG cells

To increase the length of drift spaces in the reduced excursion section, in which cavities can be installed, without increasing the required magnetic field, one can design cells with a greater orbit radius. Combining different FFAG cells with different orbit radii requires once again to consider the matching of reference orbit between these different types of cells. Starting form Eq. 4.25 and proceeding again to a first order expansion in $\frac{\Delta R_i}{R_0}$, one gets the condition of reference orbit matching between two cells, with orbit radii R_1 and R_2 respectively, as:

$$\frac{R_1}{k_1 + 1} = \frac{R_2}{k_2 + 1}. \tag{4.29}$$

4.2.4 Two-beam FFAG principle

The two-beam scaling FFAG doublet lattice was initially proposed to circulate one type of particle in both directions of rotation [69]. This kind of ring, which has successfully been tested in the two-way MURA 50-MeV electron accelerator [70], is composed of identical (but opposite field) F and D scaling FFAG magnets placed symmetrically.

Such a scheme can as well be used to circulate charged particles and their anti-particles in the same direction of rotation (see Fig. 4.3). As discussed in Sec. 4.1.2, this feature is essential to achieve simultaneous HNJ acceleration

of both μ^+ and μ^- beams. For this reason we consider thereafter to design a ring satisfying this two-beam property.

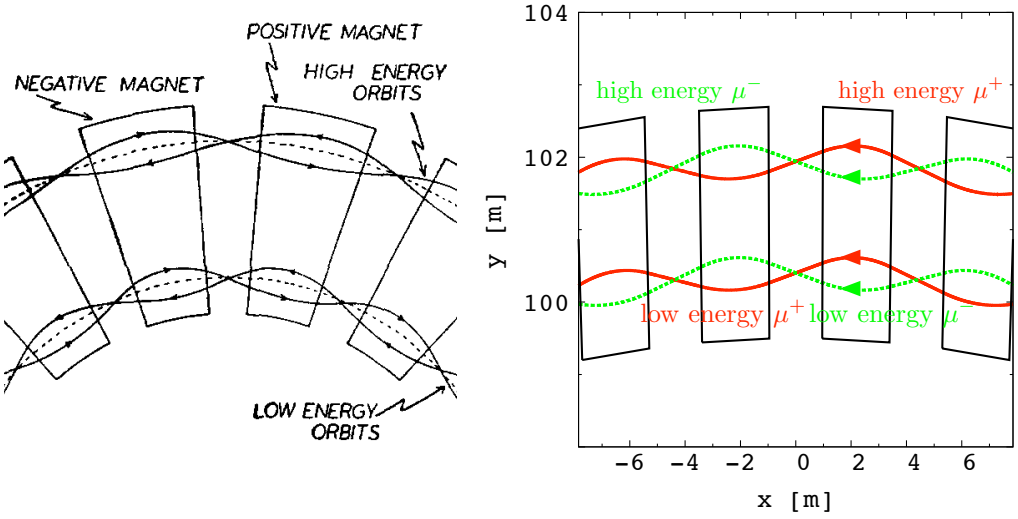

Figure 4.3: Left part: principle of the two-beam lattice as it is described in Ref. [69]. Right part: closed orbits for both μ^+ and μ^- beams circulating in the same direction of rotation, obtained from stepwise particle tracking in a hard-edge field model.

4.3 Matching issues with two-beam doublet FFAG cells

In this section, the lattice design principle presented hitherto are applied to the example of a 3.6 to 12.6 GeV muon FFAG lattice.

4.3.1 Ring made of two-beam FFAG doublet cells

Because of the effect of non-linear field components, it is not straightforward to design a ring with insertions made of two-beam FFAG doublet cells, while keeping the symmetry of behavior between both types of muons. In particular if one choose to enter in the dispersion suppressors at a point where the horizontal $\tilde{\gamma}$ for μ^+ and μ^- are not equal, the non-linear field component will affect in a different way both beams (see Sec. 4.2.2).

To demonstrate this effect, let's consider the design of a ring, with insertions, made of such two-beam scaling FFAG doublets. Since horizontal $\tilde{\gamma}$-functions are maximum for both μ^+ and μ^- beams in the center of the

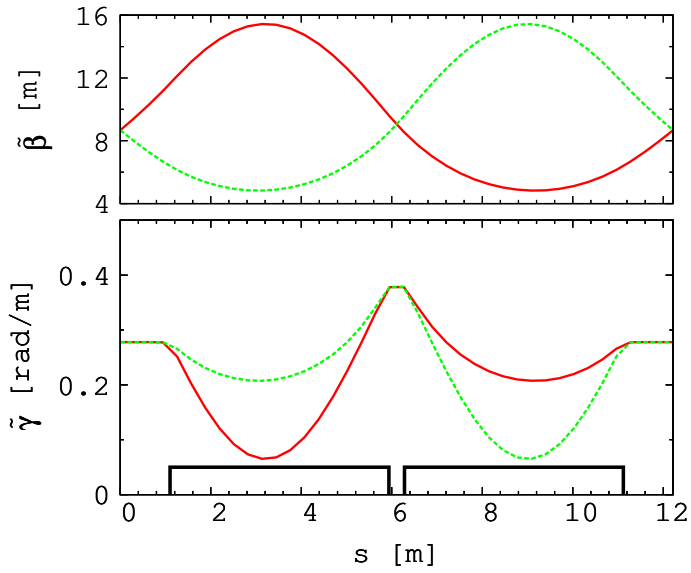

Figure 4.4: Reference horizontal $\tilde{\beta}$-functions (top part) and $\tilde{\gamma}$-functions (lower part) of a two-beam FFAG doublet cell. These functions are calculated from particle tracking with small horizontal displacements in the case of μ^+ (solid red lines) and μ^- (dotted green lines). Cells parameters are the followings: the geometrical field index k equal 130 and the average orbit radius equal 140 m; the two rectangles at the bottom of the plot show the position of the magnet effective field boundaries.

drifts, this is not a suitable place to locate the changeover between cells. From this point of view the middle of the magnets looks to be a better choice. However, at this location, the value of the $\tilde{\gamma}$-function is different for μ^+ and μ^-. Non-linear field components may thus affect in a different way both beams, inducing an asymmetrical behavior of both types of muons.

Moreover, with such doublet cells, the scalloping of the reference orbits is generally different between the different types of cells. Depending on the choice of the point of changeover between two different types of cells, it may results (i) a position mismatch for a changeover at the center of a magnet as illustrated on Fig. 4.5, (ii) an angular mismatch for a changeover at the center of a drift, (iii) or a combination of both for a changeover anywhere else.

Let's now consider the rings made of two-beam FFAG doublet cells which parameters are given Tab. 4.1. This ring comprises four excursion reduced insertions, in which the excursion is reduced by more than a factor two. A schematic layout of this ring is shown in Fig. 4.6.

The point of changeover between different types of cells has been chosen

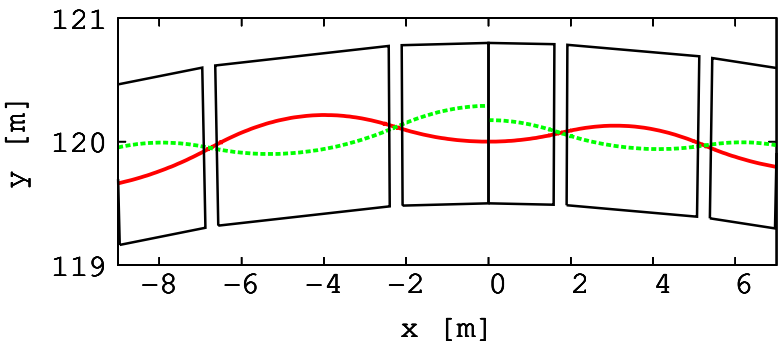

Figure 4.5: This figure shows the position mismatch between the reference orbits of the two types of cells called "first dispersion suppressor" (left part) and "second dispersion suppressor" (right part) in Tab. 4.1. The solid red lines show the reference orbit for 6 GeV μ^+, which are perfectly matched. The dotted green lines show the reference orbit for 6 GeV μ^-, with a mismatch of about 11.6 mm at the changeover between the two cells.

in the center of the positive field magnets, which are F magnets for μ^- beams and D magnets for μ^+. At this point the value of $\tilde{\gamma}$ is larger for μ^+ than for μ^-. One can thus anticipate that the μ^+ beam will be the most affected by the effect of non-linearities on the good-working of the dispersion suppressors.

Conversely, the matching of the reference orbits at the reference energy (6 GeV) is done perfectly for the μ^+ beam. The difference of scalloping of the reference orbits thus perturbs only the closed orbit of the μ^- beam. However, in this example, the difference of scalloping have been adjusted so that to cancel the closed orbit distortion in both the ring main part and the reduced excursion sections.

	Ring main part	Reduced excursion area	First dispersion suppressor	Second dispersion suppressor
Cell opening angle [deg.]	4.5	1.2425	4.3	3.34
Mean radius [m]	120	350	120	120
Field index k	145	1168.6	183.6	307.7
Horizontal phase adv./cell [deg.]	82.1	64.6	90.0	90.0
Vertical phase adv./cell [deg.]	31.8	12.6	27.6	20.4
Number of these cells in the ring	11×4	8×4	4×4	4×4

Table 4.1: Parameters of the doublet cells constituting a 3 to 10 GeV two-beam FFAG muon ring.

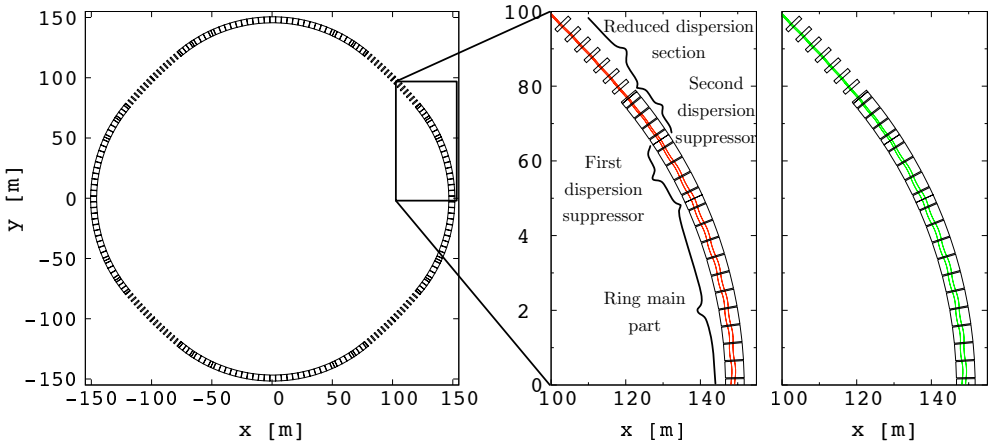

Figure 4.6: On the left: a schematic view of the ring with parameters detailed in Tab. 4.1. Position of the magnet effective field boundaries are shown. The two plots on the right: one part of the ring is detailed; the closed orbits corresponding to 3 and 10 GeV μ^+ (left, in red) and μ^- (right, in green) are superimposed.

The step-wise tracking code developed at Kyoto University and described in App. B.2 is used to determine the closed orbits of μ^+ and μ^- beams and study the linear tunes. Tune variations, from 3 to 10 GeV, are shown in Fig. 4.7. One can observe here an expression of the expected asymmetrical behavior between both types of muons. While around the reference energy (6 GeV), betatron tunes are identical and stable for both types of muons, the tune variation is much larger in the case of μ^+ below about 5 and above about 8 GeV. As expected, μ^+ is the most affected by the effect of non-linearities on the good-working of the dispersion suppressors.

This example shows that a low value of the horizontal $\tilde{\gamma}$ at the entrance of dispersion suppressors is essential to maintain the zero-chromaticity in such a ring.

In a two-beam doublet structure, the only points where the horizontal $\tilde{\gamma}$-functions of μ^+ and μ^- beams are equal correspond to maxima of the $\tilde{\gamma}$-functions (see Fig. 4.4). However, to minimize the effect of the non-linearities, one would like to enter in the dispersion suppressor at a minimum of the horizontal $\tilde{\gamma}$-functions. The ideal configuration, with horizontal $\tilde{\gamma}$-functions identical and minimum at the same location, does not exist in the doublet structure. We thus propose to modify the cell structure by introducing small additional magnets.

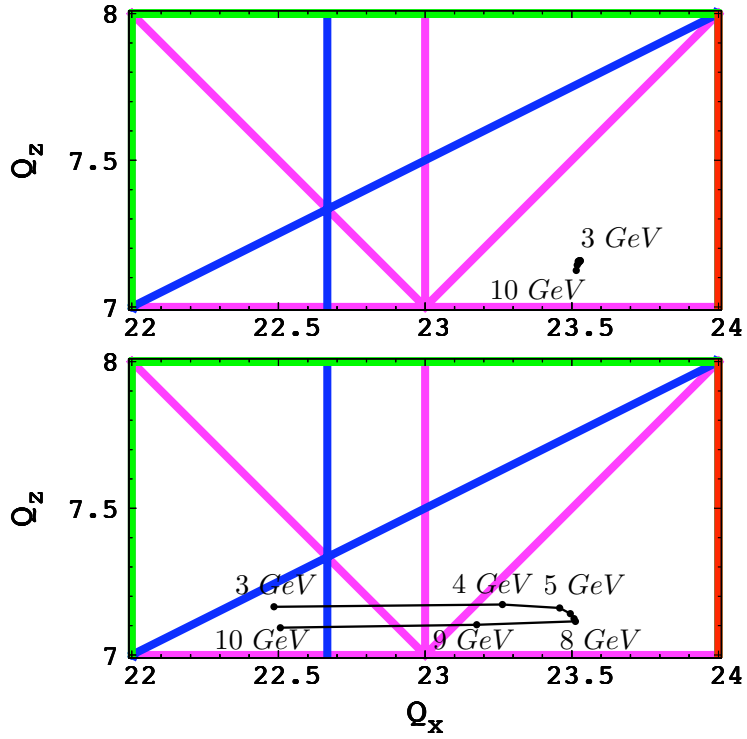

Figure 4.7: Variation of the betatron tunes in the ring made of two-beam doublet cells, plotted every 1 GeV form 3 to 10 GeV, presented in the tune diagram. The top part shows the case of the μ^- beam while the lower part shown the case of the μ^+ beam. Structure normal resonance lines up to octupole are superimposed.

4.3.2 Improved matching with two-beam quadruplet cells

The design a ring made of two-beam quadruplet cells is therefore considered. Each cell is composed of four magnets, two *main* magnets and two *small* magnets, following an f-D-F-d structure. The symmetry between all focusing and defocusing magnets is kept in order to maintain the two-beam property (see Fig. 4.8). As shown on Fig. 4.9, the horizontal $\tilde{\gamma}$-functions are identical and passes by a local minimum in the drift space between the two small magnets. Let's thus choose this point to locate the changeover between the different types of cells.

Moreover, the relative strength of the two types of magnets gives an additional degree of freedom. We choose to use it to make the closed orbits of μ^+ and μ^- beams merge at the point of changeover between cells, as shown in Fig. 4.8.

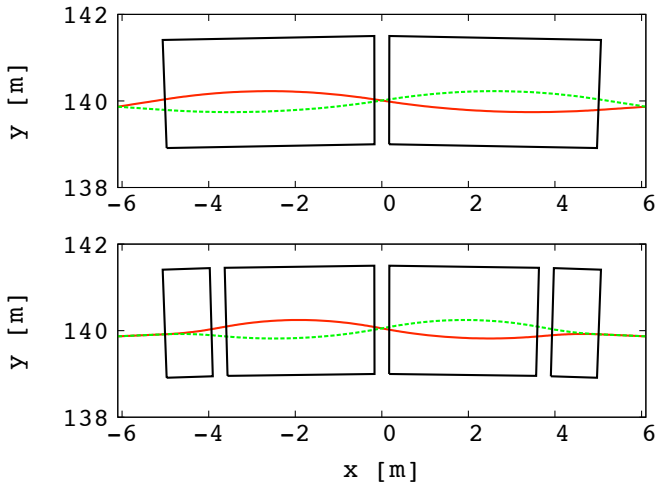

Figure 4.8: Reference orbits of μ^+ (solid red lines) and μ^- (dotted green lines) circulating in the same direction in two-beam doublet (top part) and quadruplet (lower part) FFAG cells. These two cells are identical to those used in Fig. 4.4, in the case of the doublet, and in Fig. 4.9, in the case of the quadruplet.

4.4 Example of a 3.6 to 12.6 GeV muon accelerator

Parameters of a ring made only of such two-beam quadruplet cells are given in Tab. 4.2. The maximum field on the closed orbit of 12.6 GeV muons is chosen to be below 4 T. It is a reasonable assumption once superconducting magnets with left-right asymmetrical coil distribution [71] are employed to realize the scaling field law. The excursion is reduced by a factor of two in each of the four insertions. A schematic layout of this ring is shown in Fig. 4.12. In this ring, each cell of the reduced excursion section include a 6.2 m long drift space, in which rf cavities as well as injection/extraction devices can be installed.

Thereafter, The step-wise tracking code developed at Kyoto University and described in App. B.2 is used to study the beams dynamics and the linear parameters of the lattice. Linear tunes and β-functions are calculated from the equivalent linear transfer matrix obtained from particle tracking with small amplitude motion.

With the lattice described in Tab. 4.2, horizontal and vertical betatron tunes are calculated at different energies between 3.6 and 12.6 GeV for both μ^+ and μ^-; results are shown in Fig. 4.13. As expected, one can observe a symmetric behavior between both types of muons.

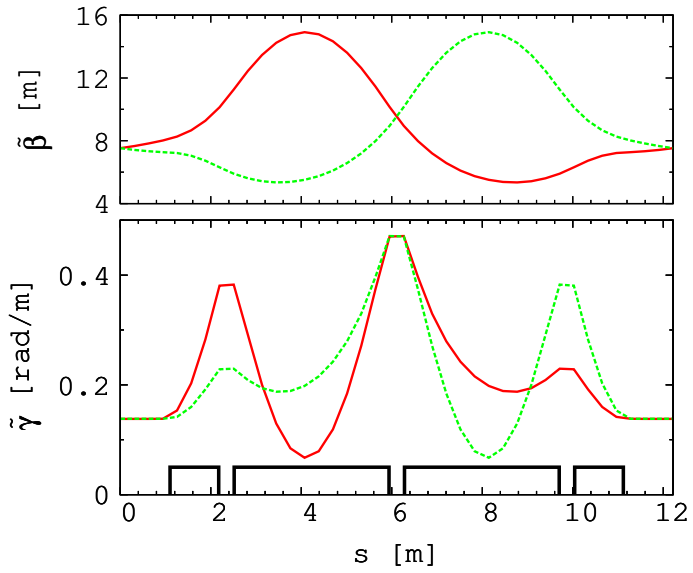

Figure 4.9: Reference horizontal $\tilde{\beta}$-functions (top part) and $\tilde{\gamma}$-functions (lower part) of a two-beam FFAG quadruplet cell. These functions are calculated from particle tracking with small horizontal displacements in the case of μ^+ (solid red lines) and μ^- (dotted green lines). Cells parameters are similar to those of the cell presented in Fig. 4.4 (same field index and orbit radius). The four rectangles at the bottom of the plot show the position of the magnet effective field boundaries.

Because of the non-linear field distribution assumed, a large number of resonances may be excited. A careful choice of the working point, far from harmful resonance lines, is thus essential to achieve large transverse acceptances. Considering that the mid-plane of scaling FFAG magnets is an anti-symmetry plane of the field distribution, normal components may exist, but skew components are excluded. Thus, in the absence of error, only normal structure resonances may be excited. Let's try therefore to choose our working point as far as possible from such resonance lines.

As one can see on this figure, the tune variation is limited to about 0.15 in horizontal, and less than 0.1 in vertical. With a proper choice of the working point, it has thus been possible to stay far from normal structure resonance lines up to the 4^{th} order (octuple). Corresponding horizontal and vertical β-functions, calculated at the reference energy (5 GeV) for both types of muons are shown in Fig. 4.10.

To achieve large transverse acceptances it is also essential to avoid the periodic β-functions to reach very large values at some position along the ring. One thus would like to avoid large modulations of the periodic β-

	Ring main part	Reduced excursion area	First dispersion suppressor	Second dispersion suppressor
Cell opening angle [deg.]	5.	2.25	4.5	3.5
Mean radius [m]	136.2	332.3	155.5	184.9
Field index k	130	638	169.9	283.5
Horiz. phase adv./cell [deg.]	87.4	86.4	90.0	90.0
Vert. phase adv./cell [deg.]	50.6	32.0	44.4	34.6
Number of these cells /ring	8×4	8×4	4×4	4×4

Table 4.2: Parameters of the quadruplet cells constituting a 3.6 to 12.6 GeV two-beam muon FFAG ring.

functions, which may arise from betatron mismatches between the different cells. To that end let's adopt the following strategy: when it is possible we minimize the betatron mismatch by choosing similar values of reference $\tilde{\beta}$-functions at the changeovers between the different types of cells; otherwise we minimize resulting modulation in one part of the lattice by making the rest of the lattice transparent, *i.e.* with phase advance multiple of 180 deg. (within a precision of few degrees).

Moreover, non-linear effects induce, in addition to the residual tune variation, a variation of the β-functions. This variation is significant in the case of the horizontal β-function, as shown in Figs. 4.11. One would like to avoid these modulations to affect the geometrical acceptance where it is the most needed, *i.e.* around the injection energy. For this reason the reference energy is chosen close to the injection energy. In this example the reference energy is 5 GeV.

4.5 Tracking simulations

4.5.1 Particle tracking at fixed energy

The transverse acceptance at fixed energy are studied with the help of single particle tracking. Muons are tracked anti-clockwise over 100 turns (*i.e.* 400 super-periods). Particles are launched with 1 mm initial vertical displacement and various initial horizontal displacements.

Results of particle tracking, plotted in the horizontal phase space, are presented in Fig. 4.14. Horizontal acceptances for both types of muons are of the order of 30 πmm.rad normalized at the injection energy (3.6 GeV). Horizontal acceptances are significantly larger than 30 πmm.rad normalized at the extraction energy (12.6 GeV) because of the greater normalization factor.

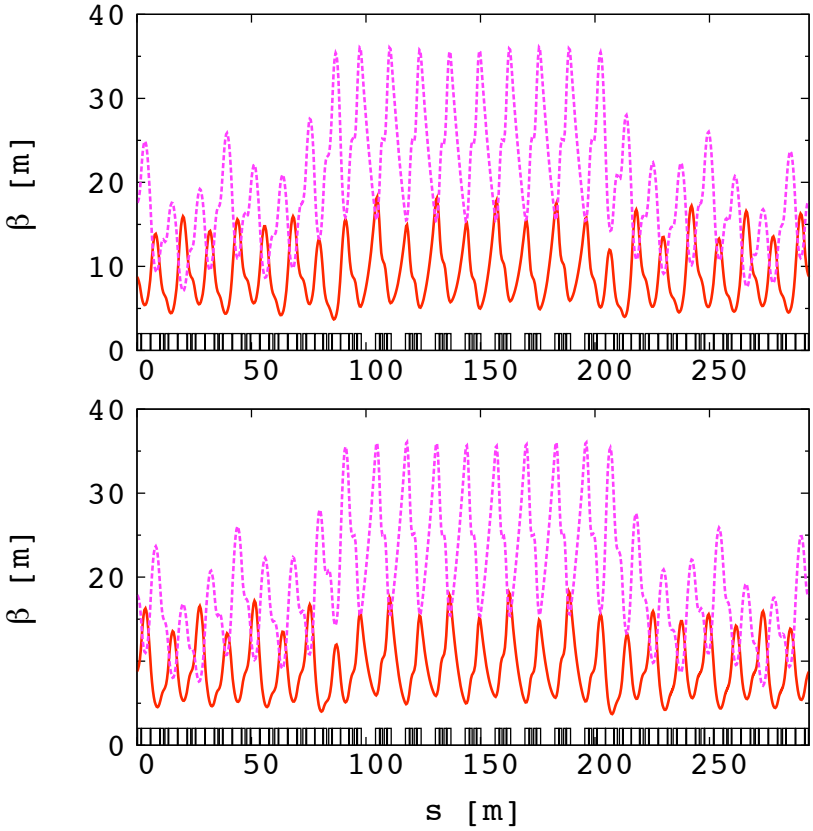

Figure 4.10: Horizontal (red solid line) and vertical (dotted purple line) β-functions in the case of 5 GeV μ^- (upper part) and μ^+ (lower part) circulating anti-clockwise in the ring described in Tab. 4.2. Notice that the β-functions of one type of muon is the mirror symmetric of the β-functions of the other type. One quarter on the ring is presented, with the plot centered on the reduced excursion section.

A similar approach is used to study the vertical acceptance at fixed energy. Muons are launched with 1 mm initial horizontal displacement and various initial vertical displacements, and then tracked anti-clockwise over 100 turns. Results are presented in Fig. 4.15. Vertical acceptances for both types of muons are also of the order of 30 πmm.rad normalized at the injection energy (3.6 GeV).

4.5.2 6D tracking simulations and results

To study the HNJ acceleration of muon beams, rf kicks are given in every cell of the reduced excursion areas. Four different rf frequencies are used, one in each reduced excursion section. These four frequencies, chosen close to

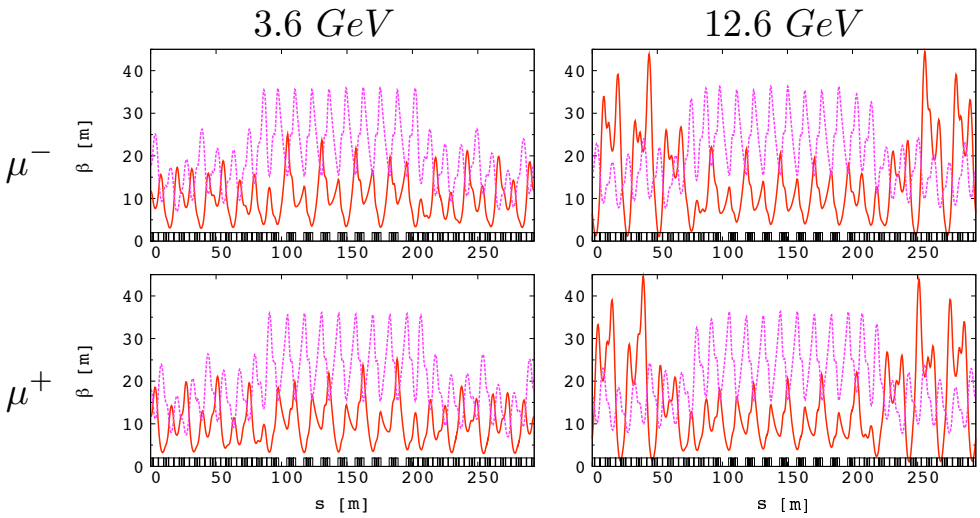

Figure 4.11: Similar plot than in Fig. 4.10, but showing the β-functions in the case of 3.6 GeV (left part) and 12.6 GeV (right part) muons circulating anticlockwise in the ring described in Tab. 4.2. The top part corresponds to μ^- while the bottom part corresponds to μ^+.

400 MHz, are calculated based on Eq. 4.16. The initial phasing of rf cavities is chosen so that particles lying at the center of the first beam crosses all rf cavities with the same rf phase during the first turn. A different initial timing corresponding to a phase difference of π is set between μ^+ and μ^- beams. Detailed parameters of the rf scheme are presented in Tab. 4.3.

The bunches of particles are prepared as follows: 1000 particles are uniformly distributed inside a transverse 4D ellipsoid (Waterbag distribution); these particles are then independently distributed uniformly inside an ellipse in the longitudinal plane. Initial normalized bunch emittances are chosen following the requirements of the International Design Study for the Neutrino Factory (IDS-NF) [45]: 30 πmm.rad in both horizontal and vertical planes and 150 mm in the longitudinal plane. The bunches of particles are put on the closed orbit at the entrance the first cell in the first reduced dispersion section, and then tracked over 8.25 turns.

Simulation results plotted in the longitudinal phase space are presented in Fig. 4.16. No significant longitudinal emittance blow-up is observed. The gradual change in the phase at which the beam crosses the cavity observed on this figure is due to synchrotron motion. This change in phase provides a variation in energy gain per turn comparable to the one described in Eq. 4.4, as shown in the plot on the right in Fig. 4.17.

The position of these particles at the beginning and at the end of the acceleration cycle is presented, plotted in horizontal and vertical phase spaces

Assumed peak rf voltage per kick	65 MV
Sum of the rf peak voltages over one turn	2.08 GV
Initial rf phase for μ^+	$0.45 \cdot 2\pi$
Initial rf phase for μ^-	$0.95 \cdot 2\pi$
Initial harmonic number	1568
Frequency of cavities in:	
the 1^{st} reduced excursion section	399.6752 MHz
the 2^{nd} reduced excursion section	399.6115 MHz
the 3^{rd} reduced excursion section	399.5477 MHz
the 4^{th} reduced excursion section	399.4840 MHz

Table 4.3: Parameters of the rf scheme assumed for the acceleration tracking simulation.

in Figs. 4.18 and 4.19. No particle has been lost during acceleration. The decrease in transverse geometrical emittance cause by acceleration dumping is visible on these figures, although a limited amount of increase in normalized emittances is observed.

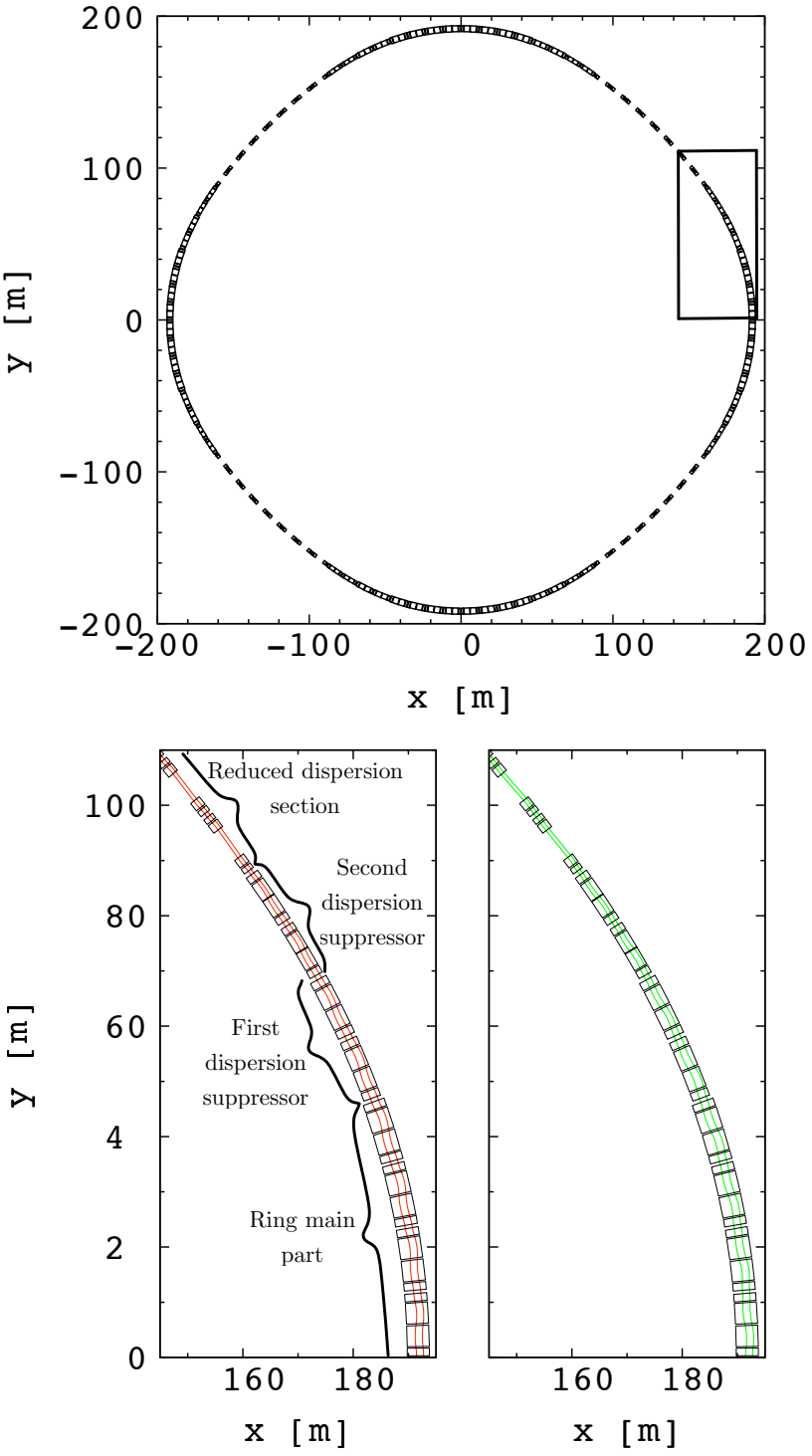

Figure 4.12: Higher part: schematic view of the ring made of quadruplet two-beam cells, which parameters are detailed in Tab. 4.2. Lower part: detailed view; the closed orbits corresponding to 3.6 and 12.6 GeV μ^+ (left, in red) and μ^- (right, in green) are superimposed.

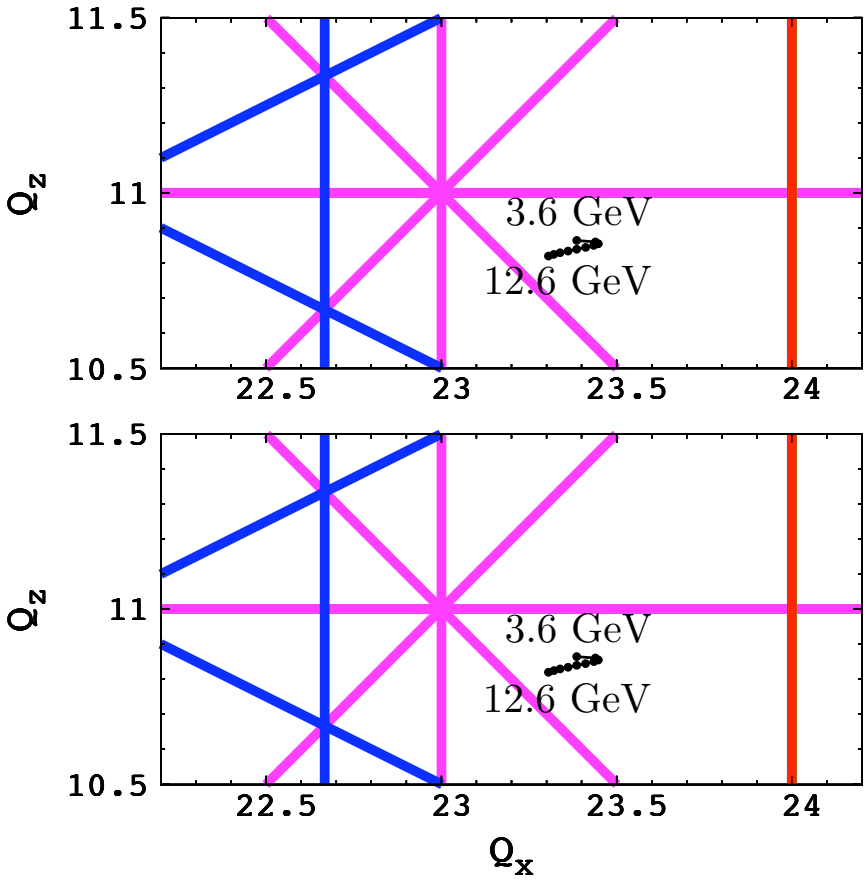

Figure 4.13: Variation of the betatron tunes, plotted every 1 GeV form 3.6 to 12.6 GeV, presented in the tune diagram. The top part shows the case of the μ^- beam while the lower part shows the case of the μ^+ beam. Structure normal resonance lines up to octupole are superimposed.

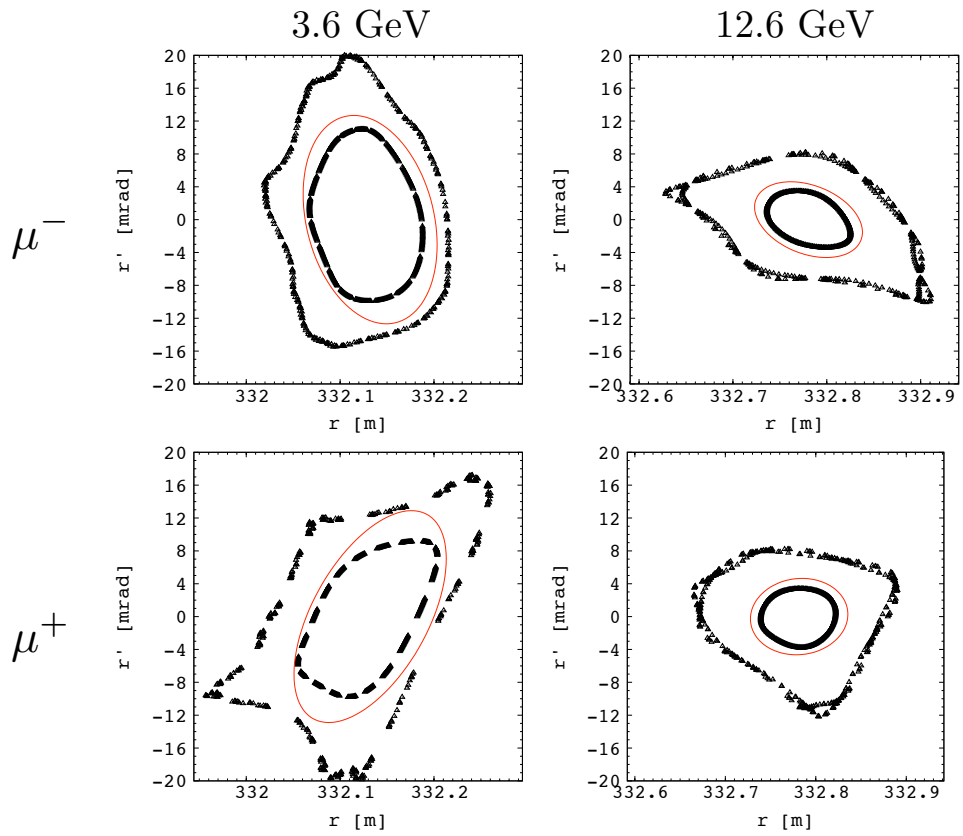

Figure 4.14: Single particle tracking results plotted in the horizontal (r,r') phase space, with the observation point located at the entrance of the first cell in a reduced dispersion section. In each plot black triangles shows the positions of two particles with different initial amplitudes, tracked over 400 super-periods. The largest amplitudes are in all case close to the largest amplitude for which the motion stays stable over 400 super-periods. Red dotted-line ellipses are superimposed. The area of these ellipses correspond to a normalized emittance of 30 πmm.rad. The parameters of these ellipses are chosen with respect to the periodic Twiss parameters calculated at the observation point. The left part corresponds to 3.6 GeV muons, while the right part corresponds to 12.6 GeV muons. The top part shows the case of μ^- while the bottom part shows the case of μ^+, both circulating anti-clockwise.

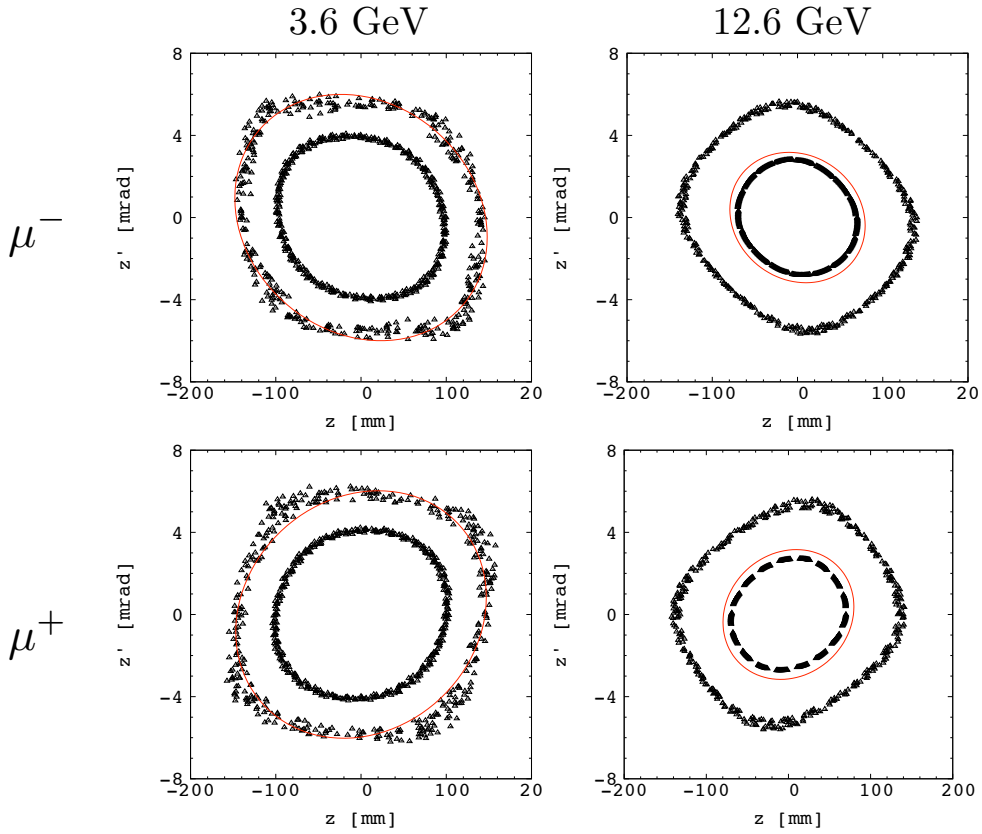

Figure 4.15: Similar plots than in Fig. 4.14 but in the case of the study of the vertical motion.

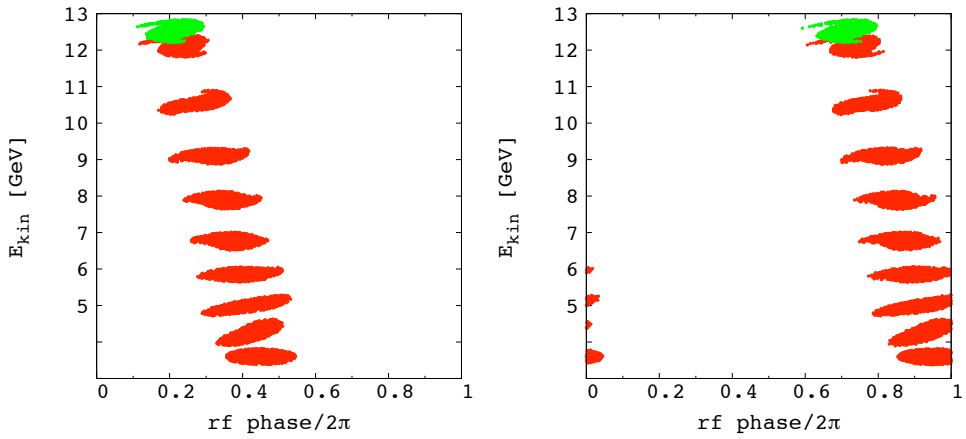

Figure 4.16: Longitudinal phase space plot showing the 8.25-turn acceleration cycle. The left plot shows the μ^+ bunch, while the right plot shows the μ^- bunch. Particles positions are plotted at the beginning of each turn as well as at the end of the acceleration cycle (after 8.25 turns), where the kinetic energy of the particle lying at the center of the bunches reaches 12.6 GeV.

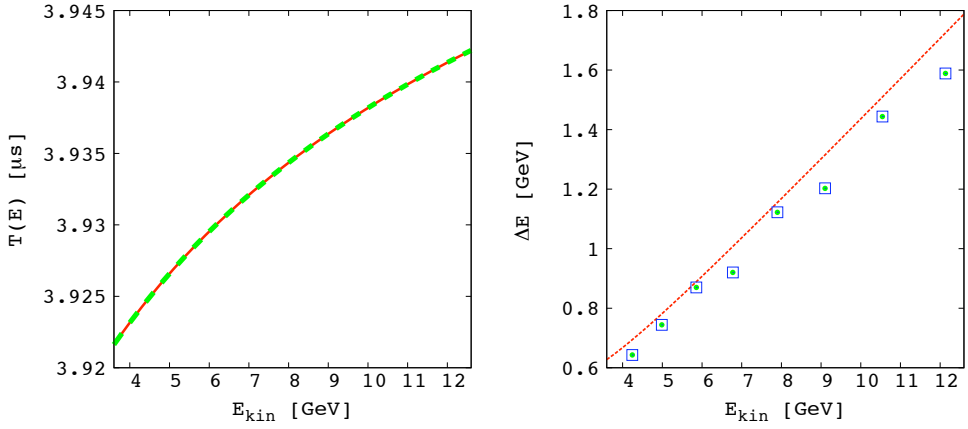

Figure 4.17: The left figure shows the revolution period $T(E)$ calculated from tracking of μ^+ (thin red solid line) and μ^- (thick green dotted line) at various energies. The required energy gain per turn for HNJ acceleration, computed from the slope of this curve as described in Eq. 4.4, is presented in the figure on the right (with red dotted line). This required energy gain is compared to the actual energy gain of the particle lying at the center of μ^+ (green dots) and μ^- (blue squares) bunches, as a function of their energy at the beginning of each turn.

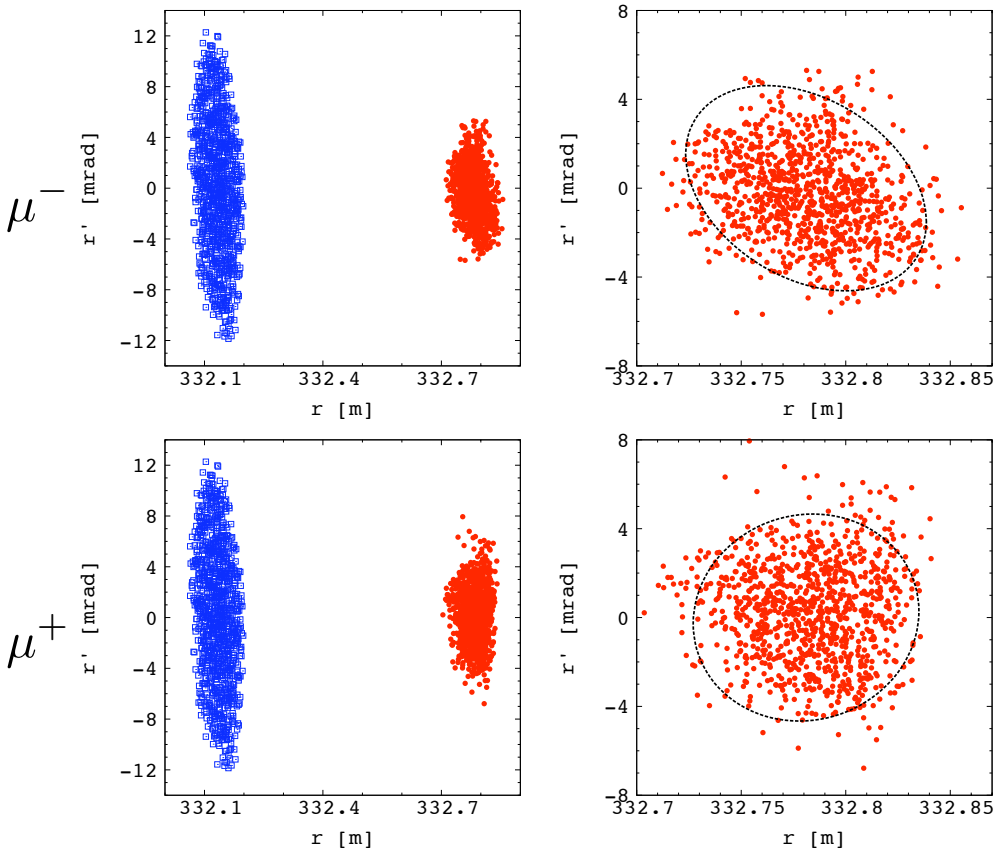

Figure 4.18: Horizontal (r,r') phase space plots showing the position of μ^- (upper plots) and μ^+ (lower plots) at the beginning (blue squares) and at the end (red dots) of the acceleration cycle. In the plots on the right, dotted-line ellipses are shown together with the position of particle at the end of the acceleration cycle. The area of these ellipses correspond to a emittance of 30 πmm.rad normalized at 12.6 GeV. The parameters of these ellipses are chosen with respect to the periodic Twiss parameters calculated at 12.6 GeV. Here less than about 10 % of the particles are lying outside of these ellipses, which indicates a certain amount of emittance blow-up.

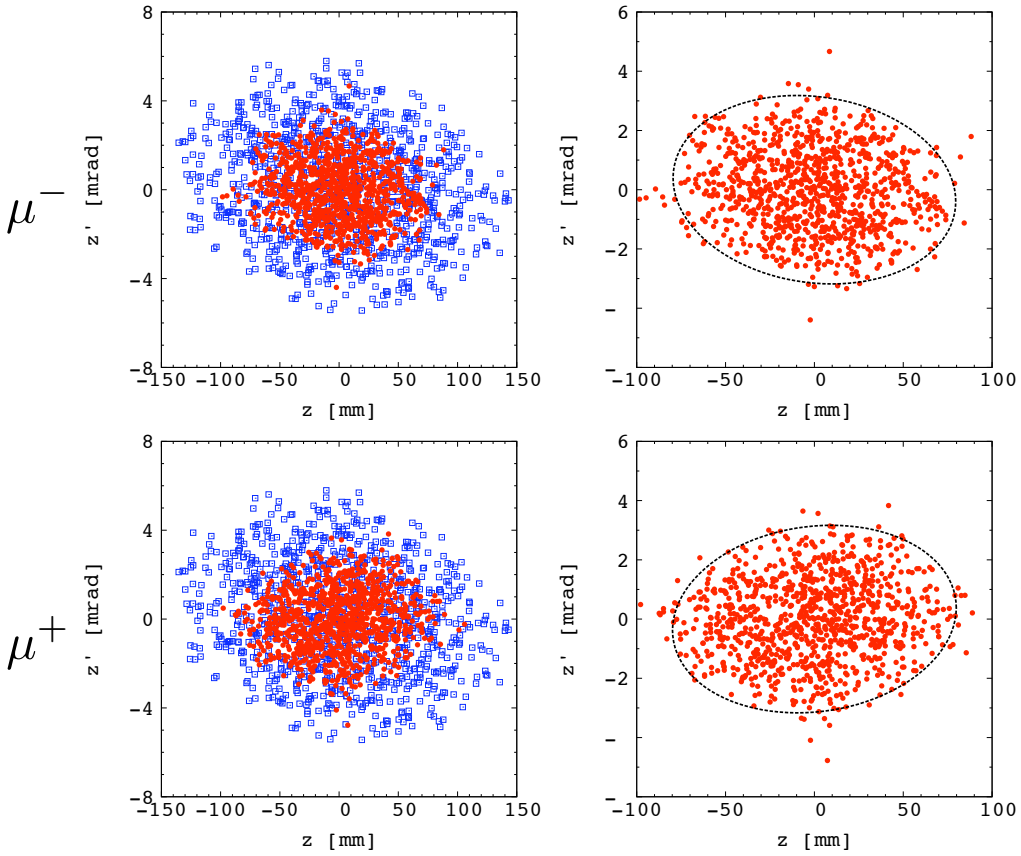

Figure 4.19: Vertical (z,z') phase space plots showing the position of μ^- (upper plots) and μ^+ (lower plots) at the beginning (blue squares) and at the end (red dots) of the acceleration cycle. In the plots on the right, dotted-line ellipses are shown together with the position of particle at the end of the acceleration cycle. The area of these ellipses correspond to a emittance of 30 πmm.rad normalized at 12.6 GeV. The parameters of these ellipses are chosen with respect to the periodic Twiss parameters calculated at 12.6 GeV. Here, about 3 % of the particles are lying outside of these ellipses.

Chapter 5
Summary

In the recent baseline designs of a neutrino factory, the acceleration of muon beams is relying on RLAs at intermediate energies, and linear non-scaling FFAGs at higher energies to reduce the cost by multiplying the number of path through the rf cavities. Since FFAG rings are more cost-efficient than RLA, due to the ring structure and the larger number of path, it is preferable to use them as much as possible. However, the large chromaticity of linear non-scaling FFAG lattices makes that, in practice, only one ring of this type can be used, and only in the last stage of the acceleration process.

A way to overcome this limitation is to use zero-chromatic type of lattices. The only type of zero-chromatic FFAG lattice known at the beginning of this study was the so-called scaling type of FFAG. However, the non-isochronism of scaling FFAGs makes that usual acceleration methods are incompatible with constant rf frequency acceleration as it is required by the IDS-NF baseline scenario.

The basic idea of this study was to develop alternative acceleration methods allowing scaling FFAG synchrotrons to achieve the rapid acceleration of muon beams in a way fully compatible with the requirements of the IDS-NF baseline scenario. The aim was thus to take advantage of their zero-chromatic optics to achieve muon acceleration from lower energies than non-scaling FFAGs, and in a more cost-efficient way than RLAs.

Two different alternative acceleration methods have been developed during this study. The first one is called the stationary bucket acceleration. The principle of this acceleration method is to use a constant rf frequency and relay on the synchrotron motion inside a wide stable area of the longitudinal phase space to accelerated particles. From an analytical understanding of the longitudinal motion in such a scheme, we highlighted that a cost-efficient use of this method requires FFAG lattices with large values of field index k. Both analytical and numerical tools have then been developed to understand how to achieve large transverse acceptances in scaling FFAGs with large field indices.

From these approaches, an example of 3.6 to 12.6 GeV muon rings based on conservative technological assumptions has been designed. This scheme uses 200 MHz rf frequency, and achieves simultaneous acceleration of μ^+ and μ^- beams within 6 turns. Tracking simulations have then been used to demonstrate the large 6D acceptance of this system. Finally, tracking

simulation with alignment errors have been carried out. These simulations have shown the relatively good robustness of this scheme.

The second alternative acceleration method studied is the so-called harmonic number jump acceleration. The principle is to use rf cavities working at constant frequencies in a non-isochronous ring in such a way that the revolution period of the particles changes every turn of an integer number of rf period. Considering the implementation of the HNJ principle to the case of scaling FFAG rings, fundamental constraints on the lattice design have been highlighted:

(i) the simultaneous acceleration of μ^+ and μ^- beams is only possible if both particles can circulate in the same direction of rotation;

(ii) the average beam excursion is necessarily large with respect to the rf wavelength, which strongly limits the achievable turn number once a usual scaling FFAG lattice is employed.

To overcome these limitations, an new type of FFAG lattice, which includes excursion reduced insertions, has been developed. The design principles of such FFAG lattices have been detailed.

These principles have been applied to the example of a 3.6 to 12.6 GeV muon ring. The lattice example thus developed combines all the following features:

(i) it includes insertions where the excursion is reduced by a factor of two;

(ii) inside these insertions, long drift spaces (6.2 m each) are available to install rf cavities, and also possibly injection and extraction devices;

(iii) both μ^+ and μ^- beams can circulate in the same direction of rotation;

(iv) the residual amount of chromaticity is small enough to avoid structure resonance crossing (up to the octupole), and eliminate the longitudinal emittance blow-up.

6D particle tracking simulations have been carried out. With these simulations it has been highlighted that, because of synchrotron motion, the phase at which particles crosses rf cavities changes slightly turn after turn providing automatically the required energy gain per turn. These 6D simulation have also shown the expected property of such a zero-chromatic lattice in terms of limitation of the longitudinal emittance blow-up. With a proper choice of the working point, it has also been shown that the transverse acceptance of such a scheme was compatible with the very large acceptances required for the acceleration of muon beams.

Chapter 6

Discussion and conclusion

It has clearly been demonstrated during this study that zero-chromatic types of FFAG can actually be used to accelerate muon beams from lower energy than the linear non-scaling FFAG rings. The important issue is now to determine whether or not it is possible to significantly improve the present baseline design of a neutrino factory, especially on the point of view of the cost of the facility.

6.1 Possibility to improve the neutrino factory baseline

To answer this question with a maximum of objectivity, we need to compare the different schemes based on criteria which essentially determine the cost and performances of the system.

6.1.1 Definition of the criteria of comparison

First, one would like to compare the transparency of these systems, *i.e.* the number of muons surviving after acceleration. Since large 6D emittance beams are assume, the transparency is first of all determined by the longitudinal and transverse acceptances of the scheme. In addition, since muons are unstable particles, the transparency of the system is also related to the rate of muons lost by decay during acceleration. Given that the rate of muon decay is given by:

$$\frac{\mathrm{d}N}{N} = -\frac{\mathrm{d}t}{\tau_0 \gamma}, \tag{6.1}$$

where N is the number of muons, t is the time variable, τ_0 is the muon lifetime in the particle rest frame and γ is its Lorentz factor. Assuming that the acceleration gradient $\mathrm{d}\gamma/\mathrm{d}s$ is constant, with s the particle path length, one can write the rate of muon lost during acceleration as [72]:

$$\eta_{decay} = 1 - \frac{N_f}{N_i} = 1 - \left(\frac{\gamma_i}{\gamma_f}\right)^{1/(c\tau_0 \mathrm{d}\gamma/\mathrm{d}s)}, \tag{6.2}$$

where c is the speed of light, and the subscripts i and f stand for "initial" and "final" respectively. Since the path length of particles in each system is different, the number of muons lost by decay is different.

	RLA-II (3.6 to 12.6 GeV)	SB acceleration in scaling FFAG	HNJ acceleration in zero-chromatic FFAG
Normalized transverse acceptance [πmm.rad]	30	30	30
Normalized longitudinal acceptance [mm]	150	150	150
Max. B field along the reference particle orbit [T]	4	4	4
Number of pass through the rf system	4.5	6	8.25
Total path length of particles [km]	2.7	6.0	9.9
Rate of muon decaying during acceleration	5.5%	12%	19%
Total length of the system [km]	1.8	1.0	1.2
Sum of the rf peak voltage per pass [GV]	2.*	1.8	2.1
Total available drift space [m]	$\sim$ 200	340	200
Minimum required accelerating gradient [MV/m]	10.	5.3	10.
"Lattice simplicity"	-	+	-

Table 6.1: Comparison between the different acceleration schemes. Parameters put in the column RLA are taken from the following reference [73]. The $*$ mark has been affixed to the value of the rf peak voltage since this value could not directly be found in this reference. It actually corresponds to the value required once on-crest acceleration is assumed. However to achieve large longitudinal acceptance, the acceleration must be slightly off-crest [44]. The actual value of the required rf peak voltage must actually be slightly larger. The value of the total available drift space is also an estimation, obtained for a figure presented in p. 28 of this Ref. [73].

In case of FFAG rings, the path length of particles tends to be longer that in RLAs due to the rings structure. The total path length is indeed given by the circumference of the rings times the number of turns; in RLAs however, it is given by the length of the linac times the number of passes, plus the sum of the length of each arc.

Next, one would like to compare the total length of each system. This is given by the perimeter in case of the FFAG rings, and by the sum of the linac and arcs length in case of the RLA. This parameters determines the length of the vacuum pipe and, to a certain extend, the total length of magnet required to guide particles. It is thus strongly related to the cost of the overall system.

Next are the parameters which essentially determine the cost of the rf system. This cost is strongly related to the sum of the cavity peak voltages. It is also related to the required rf gradient, given by the sum of the rf peak voltage divided by the space available to install rf cavities.

Finally, the criterion called "lattice simplicity" while not purely objective expresses the fact that only one single type of cell is used all around the ring in the SB scheme, while several different types of cells are used in the RLA and in the HNJ scheme.

6.1.2 Comparison between the three schemes

Based on these criteria, a comparison between the RLA assumed in the present baseline design for the acceleration of muons from 3.6 to 12.6 GeV and the two schemes proposed for the same energy range during this study is presented in Tab. 6.1.1.

As one can see in this table, the longitudinal and transverse acceptance of the three schemes are similar. However the longer path length of particles in the FFAG-based schemes tends to increase the rate of muon lost by decay during acceleration. One can notice that the about 7 % additional muon lost in the SB acceleration scheme (and 14 % for the HNJ scheme) compared to the RLA is not a critical issue. It is actually relatively small, and can thus be compensated by a slight increase in either the initial beam current or the operating time of the experiment.

The other criteria, related to the cost of the installation, are all in favor of the SB acceleration scheme. In particular the total length of the system is about half of the length of the linac plus arcs of the RLA. This implies a significant potential of cost reduction of the present baseline scenario. Moreover, this scheme makes a slightly more efficient use of the rf, with about 10 % less peak voltage required, and also a significantly lower requirement ($\sim$50 %) on the rf gradient. Finally the great simplicity of this lattice, which is indeed made of a single type of cell repeated all around the ring, is also a potential source of cost reduction of the magnet production.

The HNJ scheme however does not show obvious possibility of significant improvement of the present baseline design of a neutrino factory.

6.2 Further work

It has been highlighted that the SB scheme presents a strong potential of cost-reduction of the acceleration stage of future neutrino factories, but further studies are needed to evaluate precisely the cost of this scheme. A precise cost estimation study would especially required a detailed magnet design. Another unknown comes for the cost of the injection and extraction schemes. A preliminary design of the injection/extraction schemes for this scheme has already been proposed in Ref. [74]. A detailed technical design of such injection/extraction systems is also necessary for a precise cost estimation.

Although the interest of the HNJ scheme for the acceleration of muon is not obvious, the new type of zero-chromatic FFAG lattice developed for this purposed worth further study. The lack of flexibility of the usual scaling FFAG lattices can indeed be overcome with such lattices with insertions. Further studies dedicated to this topic may lead to significant innovations in various fields of applications of FFAG accelerators.

6.3 Conclusion

During this study, the acceleration of muon beams in zero-chromatic FFAG synchrotrons has been established. To that aim, the study of two innovative methods to accelerate particles using constant rf frequency cavities in non-isochronous FFAG rings have been carried out. An analytical understanding of the beam dynamics in such schemes has been developed. From this theoretical understanding, examples of machine parameters based on conservative technological assumption could be designed. Numerical simulations have then been carried out to verify the expected large 6D acceptance of the designed scheme, and provide a more detailed description of the longitudinal and transverse beams dynamics in such schemes.

The main results of this work are summarized below.

- From a general point of view, it has been demonstrated that it is possible to use zero-chromatic FFAG lattices to accelerate muon beams in ways which fully satisfy the requirements of the present baseline scenario of a neutrino factory.

- Concerning the stationary bucket acceleration scheme, the following results could be obtained.

  - It has been shown that this scheme can be used with rf frequencies as high as 200 MHz. For this purpose lattices with large values of field index are however preferable.
  - A detailed understanding of the transverse acceptances in scaling FFAG lattices has then been developed, allowing to determine how to achieve large transverse acceptance while using relatively large value of field index.
  - On a particular lattice example, the large 6D acceptance as well as the good tolerance to errors of this scheme have been highlighted by means of particle tracking simulations.
  - It has finally shown that this SB scheme presents a strong potential of significant cost reduction of the acceleration stage of future neutrino factories.

- Another scheme, based on harmonic number jump acceleration, has been developed.
  - By studying the implementation of this acceleration method to the case of scaling FFAG rings, a fundamental limitation on the achievable turn number has been established. This limitation comes from the necessary large excursion with respect to the rf wave length when accelerating ultra-relativistic particles.
  - To overcome this limitation, a new type of zero-chromatic FFAG ring, based on scaling type of FFAG magnets but allowing the use of insertions has been developed.
  - The interest of this scheme in the case of the acceleration of muon beams is less than the SB scheme. However, the new type of zero-chromatic FFAG lattice developed for this purposed brings an answer to the more general issue of the lack of flexibility of the usual scaling type of FFAG lattices. For this reason, the implementation of this concept to other fields of application is now being considered by research groups in Japan and overseas (see. Refs [75, 76, 77]).

- Last but not least, the SB acceleration in a scaling FFAG ring has already been admitted by the IDS-NF group, as indicated the section dedicated to this topic in the latest progress report [51].

Appendix A

Orbit analysis

A.1 Scaling field law

The Eq. 2.13.a expresses the condition of geometrical similarity of the closed orbits. It can be re-written into an integrated form:

$$\rho(p, \Theta) = R(p) \cdot f(\Theta). \tag{A.1}$$

where f is independent of p and determines the shape of the closed orbits. Equation A.1 is equivalent to:

$$r_{co}(p, \Theta) = R(p) \cdot g(\Theta), \tag{A.2}$$

where g, independent of p, is a "shape factor" common to all closed orbits, and $R(p)$ plays the role of a "scaling factor" between the closed orbits for different momenta.

From the relation

$$p = eB\rho, \tag{A.3}$$

where e is the charge of the particle, we can re-write the field index n as:

$$n = \left(\frac{\partial \rho}{\partial x}\right)_{\perp} - \frac{\rho}{p}\left(\frac{\partial p}{\partial x}\right)_{\perp}. \tag{A.4}$$

As long as R actually depends on p, the similarity of the closed orbits provides that R is bijectively associated to p. We make a last hypothesis:

Hypothesis 3. *The different closed orbits never crosses each other.*

With this hypothesis, any couple (r, θ) is thus bijectively associated to a couple (R, Θ). It allows us to use either (p, Θ, z) or (R, Θ, z) as possible systems of coordinates.

To change the system of coordinate from (x, s, z) to (R, Θ, z), we use the relation:

$$\left(\frac{\partial}{\partial x}\right)_{\perp} = \left(\frac{\partial R}{\partial x}\right)_{\perp}\left(\frac{\partial}{\partial R}\right)_{\Theta} + \left(\frac{\partial \Theta}{\partial x}\right)_{\perp}\left(\frac{\partial}{\partial \Theta}\right)_{R}. \tag{A.5}$$

We thus re-write Eq. A.4 as:

$$n = \mathcal{Q} \cdot \left(\frac{\partial R}{\partial x}\right)_{\perp} + \left(\frac{\partial \Theta}{\partial x}\right)_{\perp} R\left(\frac{\partial(\rho/R)}{\partial \Theta}\right)_{R}, \tag{A.6}$$

with $\mathcal{Q}$ defined as:

$$\mathcal{Q}(p,\Theta) = R\left(\frac{\partial(\rho/R)}{\partial R}\right)_{\Theta} - \frac{\rho}{R}\left(\frac{R}{p}\frac{\mathrm{d}p}{\mathrm{d}R} - 1\right) \tag{A.7}$$

The geometrical similarity provides that:

$$\left(\frac{\partial(\rho/R)}{\partial R}\right)_{\Theta} = 0 \quad \text{and} \quad \left[\frac{\partial}{\partial p}\left(\frac{\partial(\rho/R)}{\partial \Theta}\right)_{R}\right]_{\Theta} = 0. \tag{A.8}$$

The origin of Θ (i.e origin of s) on each closed orbit has not yet been specified. It must however be chosen so that the curves $\Theta = const.$ are continuous and at least two times differentiable. It must also vary with θ "slowly enough" to avoid contradiction with Hyp. 3.

From now on we choose to set the origin $\Theta = 0$ following a logarithmic spiral:

$$\theta_{\Theta=0}(r) = \tan\zeta \cdot \ln\left(\frac{r}{r0}\right) + \theta_0, \tag{A.9}$$

where ζ define the spiral angle, and $\theta_0 = \theta_{\Theta=0}(r_0)$. The similarity of the closed orbits provides that every curve $\Theta = const.$ follows as well a logarithmic spiral (with same ζ but different θ_0).

We define α as the angle measured between the normal to the closed orbit and the tangent to the curve $\Theta = const.$ Looking at Fig. A.1, one can write:

$$R\left(\frac{\partial\Theta}{\partial x}\right)_{\perp} = \tan\alpha\,, \tag{A.10}$$

$$\left(\frac{\partial R}{\partial x}\right)_{\perp} = \frac{\mathrm{d}R}{\mathrm{d}l}\cos\alpha, \tag{A.11}$$

where l represents the longitudinal abscissa measured along curves $\Theta = const.$

The particular properties of the logarithmic spirals provide that: (i) the angle between the tangent to the spiral and the radial vector is everywhere equal to ζ; (ii) the ratio of the longitudinal abscissa l measured along the spiral to the radius r is constant.

The first property, together with the similarity of the closed orbits, gives that the angle α is only function of Θ. The second property, together with the similarity provides:

$$\left(\frac{\partial}{\partial p}\frac{\mathrm{d}R}{\mathrm{d}l}\right)_{\Theta} = \left(\frac{\partial}{\partial p}\frac{\mathrm{d}r}{\mathrm{d}l}\right)_{\Theta} = 0. \tag{A.12}$$

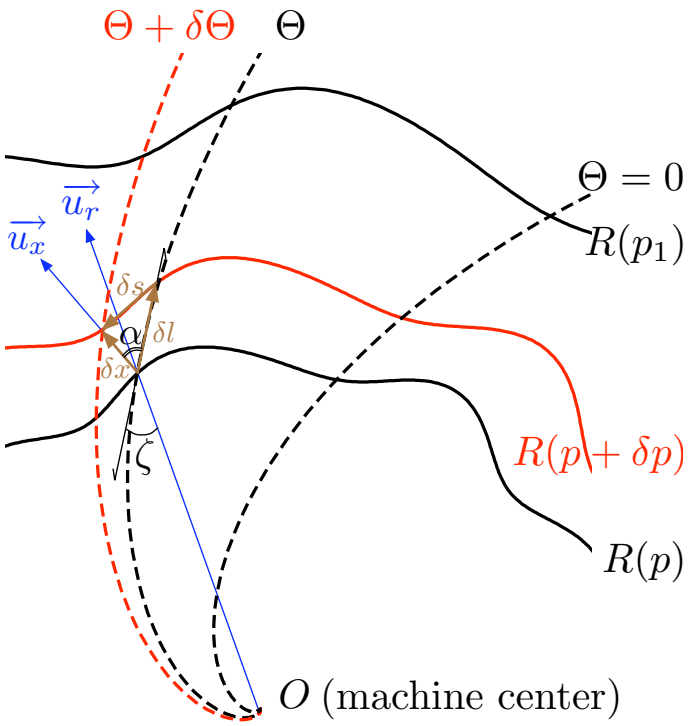

Figure A.1: The angle α is defined as the sum of the angle between the normal to the closed orbit and the radial vector and the angle between the radial vector and the tangent to the curve $\Theta = const.$

Thus:

$$\left[\frac{\partial}{\partial p}\left(R\left(\frac{\partial \Theta}{\partial x}\right)_{\perp}\right)\right]_{\Theta} = 0\,, \tag{A.13}$$

$$\left[\frac{\partial}{\partial p}\left(\frac{\partial R}{\partial x}\right)_{\perp}\right]_{\Theta} = 0. \tag{A.14}$$

If we define k as:

$$k = \frac{R}{p}\frac{\mathrm{d}p}{\mathrm{d}R} - 1, \tag{A.15}$$

we obtain that, *given the similarity of the closed orbits and the assumption set in Eq. A.9*:

$$\left(\frac{\partial n}{\partial p}\right)_{\Theta} = 0 \quad \Longleftrightarrow \quad \left(\frac{\partial k}{\partial p}\right)_{\Theta} = 0. \tag{A.16}$$

Solving Eq. A.7 with the help of Eq. A.8, this is equivalent to:

$$\frac{p}{p_0} = \left(\frac{R}{R_0}\right)^{k(\Theta)+1}, \tag{A.17}$$

with R_0 is defined as $R_0 = R(p_0)$. The geometrical similarity providing that everywhere

$$\frac{R}{R_0} = \frac{r_{co}(\Theta, p)}{r_{co}(\Theta, p_0)}, \tag{A.18}$$

we can write:

$$r_{co}(\Theta, p) = r_{co}(\Theta, p_0) \left(\frac{p}{p_0}\right)^{1/(k(\Theta)+1)} . \tag{A.19}$$

Identifying this to Eq. A.2 gives that k must not depend on Θ.

The Eq. A.19, combined with Eqs. A.2, A.3, and 2.13.a, provides, *once Eq. A.9 is assumed*, a necessary and sufficient condition of the invariance with momentum of the betatron oscillations: the magnetic field distribution in the machine mid-plane must follow

$$\boxed{B(r, \theta) = B_0 \left(\frac{r}{r_0}\right)^k \mathcal{F}(\theta - \tan\zeta \ln \frac{r}{r_0}) \,,} \tag{A.20}$$

where $\mathcal{F}$ is a function independent of p.

The approach followed in this section is based on the one described in this reference paper [2]. However, it introduce minor improvements compared to the original demonstration:

- the required field distribution in the machine mid-plane is expressed in the global polar coordinate system (r, θ) (and not (R, Θ));
- the parameters ϵ, and η used in Ref. [2], which physical meaning is difficult to comprehend, are replaced by the geometrical parameters α (angle) and l (longitudinal abscissa measured along curve $\Theta = const.$);
- the fact that the spiral geometry is an *ad-hoc* hypothesis introduced to simplify the resolution of Eq. 2.13.b is emphasized;
- the fact that k must be independent of the azimuthal position around the ring is clarified.

The last point has an essential role to play in the considerations discussed in Chapter 4.

A.2 General Considerations about Stationary Bucket Acceleration

We examine the possibility of using, in a circular accelerator with a static guide field and a constant frequency rf system, the motion inside a stationary rf bucket to accelerate particles. For practical use, one would like to increase the momentum of the particles of a significant amount going from the low to the high momentum parts of the rf bucket. The study of the longitudinal motion in such a scheme, where the relative change in momentum must not be considered as small, is discussed in this appendix.

A.2.1 Equations of Longitudinal Motion with Constant rf Frequency in the Large $\frac{\Delta p}{p}$ Regime

We consider the azimuthal coordinate Θ defined as:

$$\Theta = \int_0^s \frac{2\pi}{C} \mathrm{d}s, \tag{A.21}$$

with C the circumference of the particle closed orbit for a momentum p, and s the distance traveled by the particle. The rf frequency f_{rf} is chosen so that the revolution frequency for the momentum p_s of the synchronous particle is:

$$f_{rev_s} = \frac{f_{rf}}{h}, \tag{A.22}$$

where h, the harmonic number, is an integer. Assuming that the rf cavities are uniformly distributed around the ring, we can write the general equations of the longitudinal motion as:

$$mc^2 \frac{\mathrm{d}\gamma}{\mathrm{d}\Theta} = \frac{eV_0}{2\pi} \sin\phi \tag{A.23}$$

$$\frac{\mathrm{d}\phi}{\mathrm{d}\Theta} = f_{rf} \cdot \frac{C}{\beta c} - h, \tag{A.24}$$

with the phase ϕ defined as $\phi = 2\pi f_{rf}\, t - h\Theta$. βc is the particle velocity, m is its rest mass, γ is its Lorentz factor, t is its time coordinate. V_0 is the sum over one turn of the rf cavities peak voltage.

We would like to introduce the momentum compaction factor in the equations of motion. The momentum compaction factor in its most general definition applied to static guide field accelerators is given by [78]:

$$\alpha = \frac{\mathrm{d}\ln C}{\mathrm{d}\ln p}. \tag{A.25}$$

The momentum compaction factor is thus generally function of the momentum p. Integrating Eq. A.25 between the momentum p_s of the synchronous particle and an arbitrary momentum p we obtain:

$$\frac{C}{C_s} = \exp\left(\int_{p_s}^{p} \frac{\alpha}{p} \mathrm{d}p\right), \tag{A.26}$$

with C_s the circumference of the closed orbit for the momentum p_s. Equation A.24 can thus be written:

$$\frac{\mathrm{d}\phi}{\mathrm{d}\Theta} = h\left[\frac{\beta_s}{\beta} \cdot \exp\left(\int_{p_s}^{p} \frac{\alpha}{p} \mathrm{d}p\right) - 1\right], \tag{A.27}$$

with β_s the ratio of the synchronous particle velocity to the speed of light. Equations A.23 and A.27 are general equations of the longitudinal motion in static guide field accelerators.

A.2.2 Particular Case of Scaling FFAG Rings

In scaling FFAG rings the average magnetic field $\langle B \rangle$ increases with the orbit radius R following:

$$\langle B \rangle = \langle B_0 \rangle \left(\frac{R}{R_0}\right)^k, \tag{A.28}$$

with k constant and $\langle B_0 \rangle$ the average magnetic field for a given orbit radius R_0. The closed orbit length thus scales with $p^{\frac{1}{k+1}}$. The momentum compaction factor as defined in Eq. A.25 is then constant and given by:

$$\alpha = \frac{1}{k+1}. \tag{A.29}$$

With α independent of momentum, the term $\frac{\alpha}{p}$ in Eq. A.27 can easily be integrated. Equation A.27 thus becomes:

$$\frac{\mathrm{d}\phi}{\mathrm{d}\Theta} = h\left[\frac{\beta_s}{\beta} \cdot \left(\frac{p}{p_s}\right)^{\alpha} - 1\right] = h\left[\frac{\gamma}{\gamma_s}\left(\frac{\gamma^2-1}{\gamma_s^2-1}\right)^{\frac{\alpha-1}{2}} - 1\right]. \tag{A.30}$$

From Eqs. A.23 and A.30, we then obtain the exact Hamiltonian of the longitudinal motion in scaling FFAG, similar to the one already described in [79], and given by:

$$H(\phi, \gamma; \Theta) = h\left[\frac{1}{\alpha+1}\frac{(\gamma^2-1)^{\frac{\alpha+1}{2}}}{\gamma_s\left(\gamma_s^2-1\right)^{\frac{\alpha-1}{2}}} - \gamma\right] + \frac{eV_0}{2\pi mc^2}\cos\phi, \tag{A.31}$$

where γ_s is the Lorentz factor of the synchronous particle. The longitudinal motion in scaling FFAG rings can thus be described analytically without any assumption on the relative value of γ and γ_s.

A.3 Dynamic acceptance dependence on k, tune per cell being fixed

To understand the effect of these non-linear field components on the dynamic acceptance (DA), we follow the approach presented in the reference papers [80, 81]. Considering first of all the very small amplitude motion of particles around a stable equilibrium orbit, the effect of non-linear field components can be neglected, and the particle motion is described by linear equations of motion, such as Eq. 2.2. In each plane particles oscillate then around the equilibrium orbit at a frequency which is independent of the amplitude. As the initial amplitude of the particle is increased, the effect of non-linear field components become significant, and the oscillation frequencies change because of non-linear forces. The oscillation frequencies continue to change if the initial amplitude is increased, until they reach a resonant condition:

$$m_x(\nu_x + \Delta\nu_x) + m_z(\nu_z + \Delta\nu_z) = q, \tag{A.32}$$

where $\Delta\nu_x$ and $\Delta\nu_z$ quantify the variation with amplitude of the tunes per cell, and m_x, m_z and q are *small* integers. For larger amplitudes, the motion is assumed unstable.

For simplicity reasons we reduce our study to the case of one degree of freedom. The resonance condition thus reduces to:

$$\nu + \Delta\nu = n/m, \tag{A.33}$$

Where ν stands for either the horizontal of the vertical linear tune per cell.

To go further we assume that the main source of amplitude detuning is the lowest order non-linear component, i.e. the sextupole component. With this assumption, the canonical perturbation theory [55] provides that $\Delta\nu$ varies as:

$$\Delta\nu = -\frac{J_1}{64\pi}\int_0^C \left[\beta(s)^{3/2}S(s)\int_s^{s+C}\beta(\tilde{s})^{3/2}S(\tilde{s})A(\nu,s,\tilde{s})\mathrm{d}\tilde{s}\right]\mathrm{d}s \tag{A.34}$$

where J_1 can be assimilated to the emittance ϵ of the particle. Here, the independent variable is the longitudinal abscissa s measured along the closed orbit. Symbol $\beta(s)$ stands for the local values of the Curant-Synder linear β-function, while $S(s)$ represent the local value of the sextupole field component. The integrals are done over one period, which means that C corresponds the length of one periodic cell. The resonating term A is defined as:

$$A(\nu,s,\tilde{s}) = \frac{3\cos(\psi(\tilde{s}) - \psi(s) - \pi\nu)}{\sin\pi\nu} + \frac{\cos 3(\psi(\tilde{s}) - \psi(s) - \pi\nu)}{\sin 3\pi\nu}, \tag{A.35}$$

where ψ can be assimilated to the phase of the betatron oscillation. Once integrated with respect to s and $\tilde{s}$, this term depends only on ν.

We now would like to determine how $\Delta\nu$ depends on k at a given working point (ν_x and ν_z fixed). To that end we use the *smooth approximation*, assimilating the functions $\beta(s)$ and $S(s)$ to their average values $\langle\beta\rangle$ and $\langle S\rangle$. It thus provides that:

$$\Delta\nu \propto \epsilon\langle\beta\rangle^3\langle S\rangle^2 C^2. \tag{A.36}$$

From Eq. 2.15, for $k \gg 1$, we obtain that

$$\langle S\rangle \propto k^2. \tag{A.37}$$

As described in Ref. [2] the values of tunes can be approximated for radial sector machines, in frame of the *smooth approximation*, as:

$$\begin{aligned}(N\nu_x)^2 &\simeq 1 + k + \frac{(k+1)^2\langle g_1^2\rangle f^2}{N^2},\\ (N\nu_z)^2 &\simeq -k + \frac{f^2}{2} + \frac{(k-1)^2\langle g_1^2\rangle f^2}{N^2},\end{aligned} \tag{A.38}$$

where N is the number of periodic cells in the ring, f is the flutter factor which characterize the amplitude of the azimuthal variation of filed. If we assume once again $k \gg 1$, we can write:

$$\nu_x^2 - \nu_z^2 \simeq \frac{2k - \frac{1}{2}f^2}{N^2}. \tag{A.39}$$

If we want to vary k while keeping the tunes per cell fixed, and if f is scaled with N, the number of cells in the ring must be scaled as $\sqrt{k}$. This means that, if the orbit radius is fixed, the cell length should scale as:

$$C \propto \frac{1}{\sqrt{k}}. \tag{A.40}$$

Finally providing that

$$\nu = \frac{1}{2\pi}\int_0^C \frac{\mathrm{d}s}{\beta(s)} = \frac{C}{2\pi\langle\beta\rangle}, \tag{A.41}$$

once ν is fixed we get:

$$\langle\beta\rangle \propto \frac{1}{\sqrt{k}}. \tag{A.42}$$

Injecting these equations in Eq. A.36 one gets:

$$\Delta\nu \;\propto\; \epsilon\, k^{3/2}. \tag{A.43}$$

Then providing the definition of the amplitude limit given in Eq. A.33, the largest emittance after which the motion is not stable anymore depends on

k as:

$$\boxed{\epsilon_{max} \propto k^{-3/2}} \tag{A.44}$$

This result is consistent with the estimation of the maximum stable emittance ϵ_{max} derived in the particular case of a working point in the vicinity of a third integer resonance derived in Ref. [80]:

$$\epsilon_{max} = \nu N \left(\frac{8}{3} \frac{N^2}{B_1} \left(\nu - \frac{1}{3} \right) \right)^2, \tag{A.45}$$

where B_1 is the sextupole driving term. With $B_1 \propto k^2$ and, once the working point (ν_x, ν_z) is fixed, $N \propto \sqrt{k}$ (see Eq. A.39), we find also that ϵ_{max} goes with $k^{-3/2}$.

However we have demonstrated here that this dependence on k is actually much more general and can be applies to a large variety of working points, as long as the sextupole filed component is the main source of amplitude detuning.

A cross-check study based on tracking simulations has been carried out. To study the dependence on k of the acceptance, the value of k is varied but the position of the working point is kept fixed, by changing the cell opening angle and the relative strength between F and D magnets. A large variety of working points have been studied. The horizontal and transverse acceptances are estimated as described in App. B.2.4. Results are plotted in Log-Log scale are presented in Fig. A.2. One can notice that both horizontal and vertical acceptance tend to decrease, in Log-Log scale, following lines with a slope close to -1.5. This tends to confirm the dependence as $k^{-3/2}$ of the transverse acceptances.

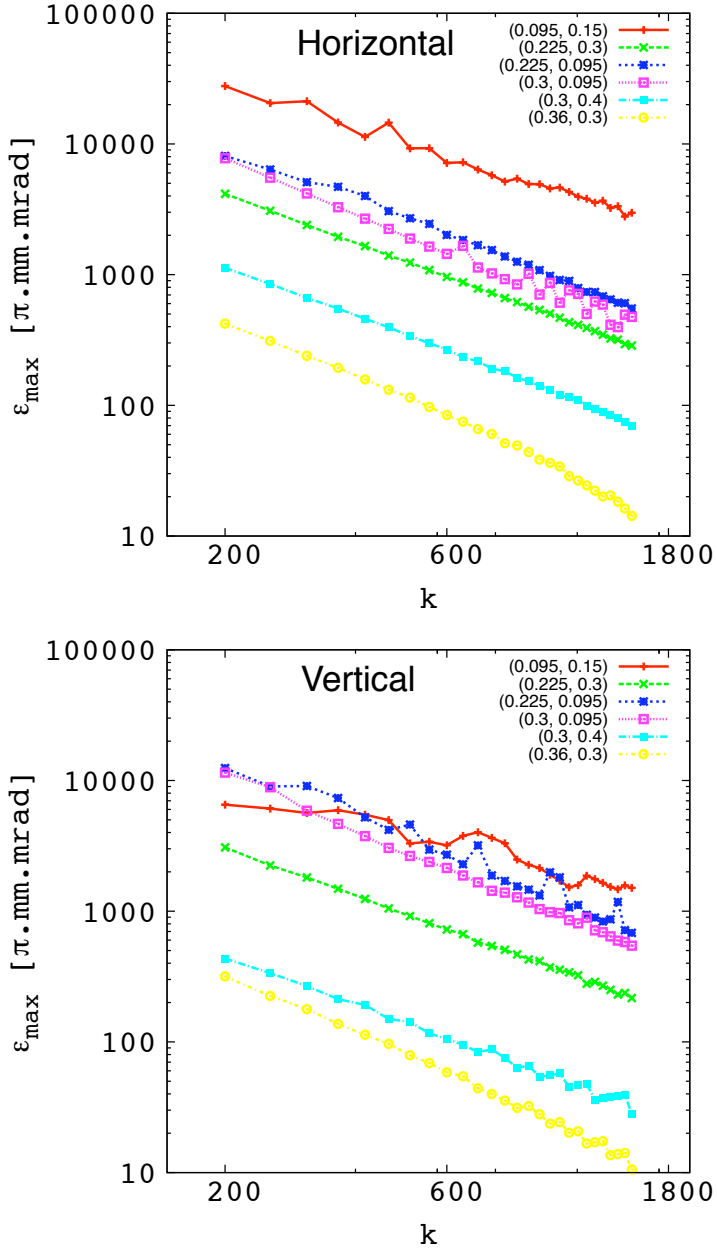

Figure A.2: Horizontal (top figure) and vertical (bottom figure) acceptance function of the field index k, once the position of the working point in the cell tune diagram is kept fixed. Several working points (ν_x, ν_z) are presented (see legend on the top-right corner of each figure), plotted in Log-Log scale.

Appendix B

Numerical simulation tools

B.1 Matrix calculation

Before starting precise but time-consuming particle tracking simulations, it is essential to determine roughly the cell parameters to ensure beam stability and come close to the required optical properties. In this section we thus describe a simple way to approach the linear parameters of an FFAG lattice.

B.1.1 Closed orbit parameters

The first step is to determine the characteristics of the closed orbit for given geometrical parameters of the cell (*i.e.* opening angle, and position, size and relative strength of the different magnets).

To illustrate how we proceed, we consider first the example of a scaling FFAG cell with an F-D-F structure. For simplicity reasons we assume that the curvature of the closed orbit is constant in the gap of each magnet, and null in the drift spaces between magnets. From geometrical considerations,

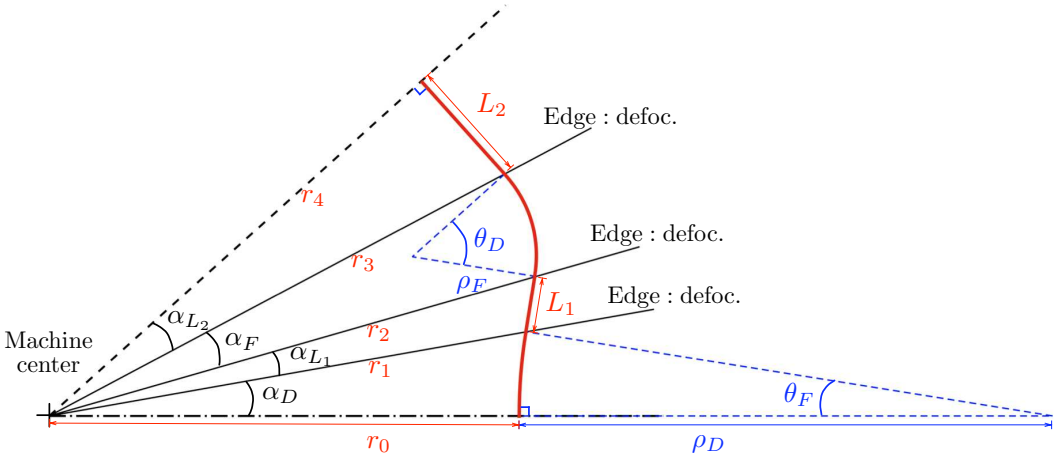

Figure B.1: Determination of the closed orbit parameters in the case of an F-D-F type of FFAG cell. On this drawing one half of the cell is presented.

and using the notations defined in in Fig. B.1, the relations the closed orbit

must satisfy write as:

$$\begin{aligned}
\theta_F - \theta_D &= \alpha_F + \alpha_D + \alpha_{L_1} + \alpha_{L_2} && \text{(B.1)}\\
\rho_D \sin\theta_D &= r_1 \sin\alpha_D && \text{(B.2)}\\
r_1 \cos\alpha_D &= r_0 + \rho_D(1-\cos\theta_D) && \text{(B.3)}\\
r_4 &= r_3\cos(\alpha_{L_2}) && \text{(B.4)}\\
r_2\cos\alpha_F &= r_3 - 2\rho_F \sin\frac{\theta_F}{2}\sin(\frac{\theta_F}{2} - \alpha_{L_2}) && \text{(B.5)}\\
r_3\sin\alpha_F &= 2\rho_F \sin\frac{\theta_F}{2}\cos(\frac{\theta_F}{2} - \alpha_{L_2} - \alpha_F) && \text{(B.6)}\\
r_2\sin\alpha_{L_1} &= L_1\cos(\theta_D + \alpha_D) && \text{(B.7)}\\
r_2\cos\alpha_{L_1} &= r_1 + L_1\sin(\theta_D + \alpha_D) && \text{(B.8)}\\
L_2 &= r_3\sin\alpha_{L_2} && \text{(B.9)}
\end{aligned}$$

Making the approximation that angles are small, and developing these equations to the first order one gets:

$$\begin{aligned}
\theta_F - \theta_D &= \alpha_F + \alpha_D + \alpha_{L_1} + \alpha_{L_2} && \text{(B.10)}\\
\rho_D\theta_D &\simeq r_1\alpha_D && \text{(B.11)}\\
r_1 &\simeq r_0 && \text{(B.12)}\\
r_4 &\simeq r_3 && \text{(B.13)}\\
r_2 &\simeq r_3 && \text{(B.14)}\\
r_3\alpha_F &\simeq \rho_F\theta_F && \text{(B.15)}\\
r_2\alpha_{L_1} &\simeq L_1 && \text{(B.16)}\\
r_2 &\simeq r_1 + L_1(\theta_D + \alpha_D) && \text{(B.17)}\\
L_2 &\simeq r_3\alpha_{L_2} && \text{(B.18)}
\end{aligned}$$

The remaining two degrees of freedom are the choice of the closed orbit radius defined as:

$$\langle r\rangle = \frac{r_1 + r_2}{2}, \qquad \text{(B.19)}$$

and the relative strength between F and D magnets, so-called F/D ratio, defined as:

$$\text{fdr} = \frac{\rho_F\theta_F}{\rho_D\theta_D}. \qquad \text{(B.20)}$$

In the approximation of small angles, the system of equations satisfied by

a closed orbits thus writes:

$$\begin{cases} \langle r \rangle = \dfrac{r_1 + r_2}{2} \\ \text{fdr} = \dfrac{\rho_F \theta_F}{\rho_D \theta_D} \\ \theta_F - \theta_D = \alpha_F + \alpha_D + \alpha_{L_1} + \alpha_{L_2} \\ \rho_1 \theta_D = r_D \alpha_D \\ r_2 \alpha_F = \rho_F \theta_F \\ L_1 = r_2 \alpha_{L_1} \\ r_2 = r_1 + L_1(\theta_D + \alpha_D) \\ L_2 = r_2 \alpha_{L_2} \end{cases} \tag{B.21}$$

with the following eight unknowns: θ_F, θ_D, r_1, r_2, ρ_F, ρ_D, L_1, L_2. Although this system is non-linear, it has a unique solution given by:

$$\begin{cases} \theta_D = \dfrac{\alpha_D \text{fdr} - \alpha_F - \alpha_D^2 \alpha_{L_1} \text{fdr}}{\alpha_D \alpha_{L_1} \text{fdr}} \\ \theta_F = \theta_D + \alpha_F + \alpha_D + \alpha_{L_1} + \alpha_{L_2} \\ r_1 = \langle r \rangle \dfrac{2\alpha_F}{\alpha_F + \alpha_D \text{fdr}} \\ r_2 = \langle r \rangle \dfrac{2\alpha_D \text{fdr}}{\alpha_F + \alpha_D \text{fdr}} \\ \rho_F = \langle r \rangle \dfrac{-2\alpha_D^2 \alpha_F \alpha_{L_1} \text{fdr}^2 (\theta_F - \theta_D)}{(\alpha_F + \alpha_D \text{fdr})((\theta_F - \theta_D)(\alpha_F - \alpha_D \text{fdr} + \alpha_D^2 \alpha_{L_1} \text{fdr}) - \alpha_D \alpha_{L_1} \text{fdr})} \\ \rho_D = \langle r \rangle \dfrac{-2\alpha_D^2 \alpha_F \alpha_{L_1} \text{fdr}}{(\alpha_F + \alpha_D \text{fdr})(\alpha_F - \alpha_D \text{fdr} + \alpha_D^2 \alpha_{L_1} \text{fdr})} \\ L_1 = r_2 \alpha_{L_1} \\ L_2 = r_2 \alpha_{L_2} \end{cases} \tag{B.22}$$

This solution has been first obtained using the computational software Mathematica©.

D-F-D triplet case

In a similar way, we derive the closed orbit parameters in the case of a D-F-D triplet cell. With the notation defined in Fig. B.2, it gives:

$$\begin{cases} \theta_F = \dfrac{-\alpha_F + \alpha_F^2\alpha_{L_1} + \alpha_D \mathrm{fdr}}{\alpha_F \alpha_{L_1}} \\ \theta_D = \theta_F - \alpha_F - \alpha_D - \alpha_{L_1} - \alpha_{L_2} \\ r_1 = \langle r \rangle \dfrac{2\alpha_D \mathrm{fdr}}{\alpha_F + \alpha_D \mathrm{fdr}} \\ r_2 = \langle r \rangle \dfrac{2\alpha_F}{\alpha_F + \alpha_D \mathrm{fdr}} \\ \rho_F = \langle r \rangle \dfrac{2\alpha_D \alpha_F^2 \alpha_{L_1} \mathrm{fdr}}{(\alpha_F + \alpha_D \mathrm{fdr})(-\alpha_F + \alpha_F^2 \alpha_{L_1} + \alpha_D \mathrm{fdr})} \\ \rho_D = \langle r \rangle \dfrac{-2\alpha_D \alpha_F^2 \alpha_{L_1} (\theta_F - \theta_D)}{(\alpha_F + \alpha_D \mathrm{fdr})((\theta_F - \theta_D)(\alpha_F - \alpha_F^2 \alpha_{L_1} - \alpha_D \mathrm{fdr}) + \alpha_F \alpha_{L_1})} \\ L_1 = r_2 \alpha_{L_1} \\ L_2 = r_2 \alpha_{L_2} \end{cases} \tag{B.23}$$

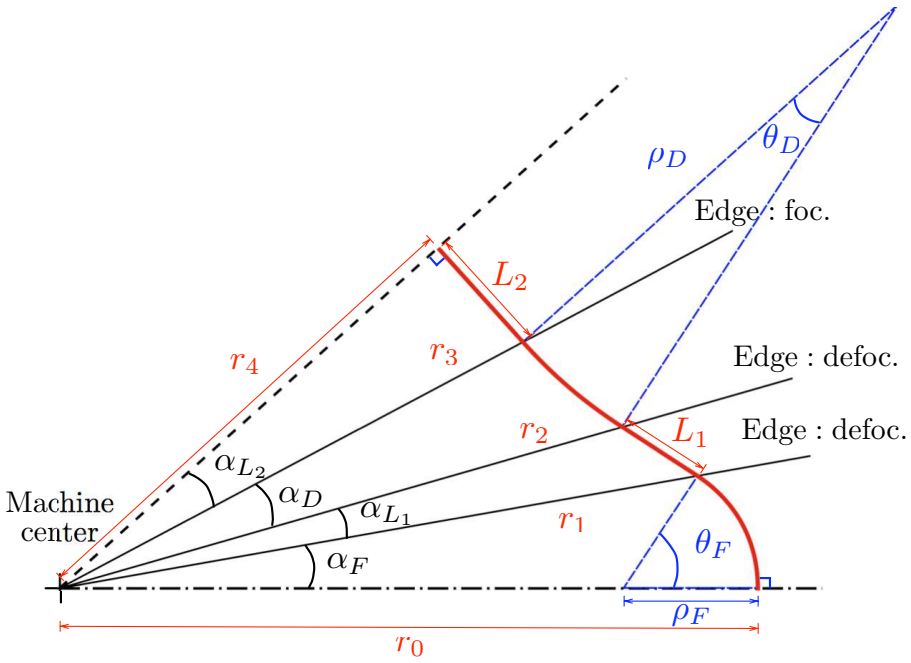

Figure B.2: Determination of the closed orbit parameters in the case of an D-F-D type of FFAG cell. On this drawing one half of the cell is presented.

Particular case of two-beam FFAG cells

In the case of two-beam FFAG cells, the number of degree of freedom is degreased because of the required symmetry between F and D magnets.

$$\begin{cases} \theta_F = \dfrac{-1+\alpha_M\alpha_L+\mathrm{fdr}}{\alpha_L} \\ \theta_D = \dfrac{-1-\alpha_L^2-\alpha_M\alpha_L+\mathrm{fdr}}{\alpha_L} \\ r_1 = \langle r\rangle \dfrac{2\mathrm{fdr}}{1+\mathrm{fdr}} \\ r_2 = \langle r\rangle \dfrac{2}{1+\mathrm{fdr}} \\ \rho_F = \langle r\rangle \dfrac{2\alpha_M\alpha_L\mathrm{fdr}}{(1+\mathrm{fdr})(-1+\alpha_M\alpha_L+\mathrm{fdr})} \\ \rho_D = \langle r\rangle \dfrac{-2\alpha_M\alpha_L}{(1+\alpha_L^2+\alpha_L\alpha_M-\mathrm{fdr})(1+\mathrm{fdr})} \\ L = \langle r\rangle \dfrac{2\alpha_L}{1+\mathrm{fdr}} \end{cases} \tag{B.24}$$

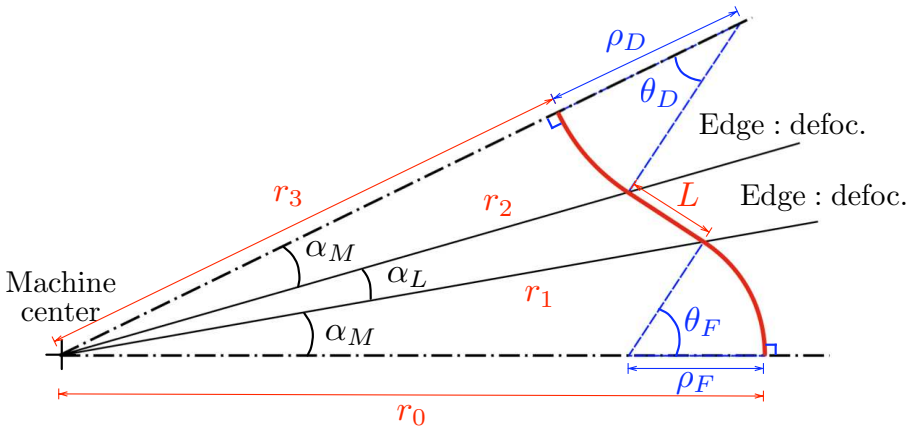

Figure B.3: Determination of the closed orbit parameters in the case of a double two-beam FFAG cell. On this drawing one half of the cell is presented.

The fewer degree of freedom in such lattice make that the value the F/D ratio fdr is fully determined by the cell geometry and the value of the geometrical field index k. From the scaling field law ($\langle B\rangle \propto r^k$), we deduce the approximate relation between k and the closed orbit parameters:

$$k\ln\left(\frac{r_1}{r_2}\right) = \ln\left(\frac{\rho_D}{\rho_F}\right) \quad \Rightarrow \quad k = \frac{\ln(\mathrm{fdr})}{\ln\left(\frac{\rho_D}{\rho_F}\right)} \tag{B.25}$$

B.1.2 Linear transfer matrices

The linear transfer matrix of combined function magnets, such a scaling FFAG magnets, can be written as follows [56]:
when $K > 0$:

$$\mathbf{M_{K>0}} = \begin{pmatrix} \cos(l\sqrt{K}) & \frac{1}{\sqrt{K}}\sin(l\sqrt{K}) \\ -\sqrt{K}\sin(l\sqrt{K}) & \cos(l\sqrt{K}) \end{pmatrix}, \tag{B.26}$$

and, when $K < 0$:

$$\mathbf{M_{K<0}} = \begin{pmatrix} \cosh(l\sqrt{-K}) & \frac{1}{\sqrt{-K}}\sinh(l\sqrt{-K}) \\ \sqrt{-K}\sinh(l\sqrt{-K}) & \cosh(l\sqrt{-K}) \end{pmatrix}. \tag{B.27}$$

The optical length l of the magnets is defined as $l = \rho\theta$. The coefficient K is defined in the horizontal plane as:

$$\begin{aligned} K = & \quad \frac{|n|+1}{\rho_F^2} \quad \text{for F magnets} \\ K = & \quad \frac{|n|-1}{\rho_D^2} \quad \text{for D magnets,} \end{aligned} \tag{B.28}$$

and in the vertical plane as:

$$\begin{aligned} K = & \quad \frac{-|n|}{\rho_F^2} \quad \text{for F magnets} \\ K = & \quad \frac{|n|}{\rho_D^2} \quad \text{for D magnets,} \end{aligned} \tag{B.29}$$

where n is the effective field index calculated around the closed orbit. With scaling FFAG, a relation between n and the geometrical field index k can be obtained form Eq.A.6. To calculate the effective field index, we average this expression over one magnet. Using the assumption that the curvature of the closed orbit is constant in the magnet, one can write:

$$n \simeq -\frac{\rho}{R}k \cdot \left\langle \left(\frac{\partial R}{\partial x}\right)_{\perp} \right\rangle + \; R\left(\frac{\partial(\rho/R)}{\partial\Theta}\right)_R \left\langle \left(\frac{\partial\Theta}{\partial x}\right)_{\perp} \right\rangle, \tag{B.30}$$

where the notation $\langle\rangle$ represents the average over one magnet. From geometrical considerations we make the following approximations:

$$R \simeq \langle r \rangle \tag{B.31}$$

and,

$$\left\langle \left(\frac{\partial\Theta}{\partial x}\right)_{\perp} \right\rangle \simeq 0 \tag{B.32}$$

and,

$$\left\langle \left(\frac{\partial R}{\partial x} \right)_{\perp} \right\rangle \simeq \pm 1, \tag{B.33}$$

the + and − signs corresponding to the case of F and D magnets, respectively. With these approximations, one can write:

$$\boxed{n \simeq \mp \frac{\rho}{\langle r \rangle} k,} \tag{B.34}$$

providing n function of given parameters. In this equation the + sign corresponds to the case of D magnets, while the − corresponds to the case of F magnets.

The transfer matrix representing the effect of edge focusing in the horizontal plane writes:

$$\mathbf{M_{edge}} = \begin{pmatrix} 1 & 0 \\ \frac{\tan \epsilon}{\rho} & 1 \end{pmatrix}, \tag{B.35}$$

with ϵ the edge angle. In the vertical plane, the edge focusing is approximated by:

$$\mathbf{M_{edge}} = \begin{pmatrix} 1 & 0 \\ -\frac{\tan \epsilon}{\rho} & 1 \end{pmatrix}. \tag{B.36}$$

Finally, the transfer matrix corresponding to drift spaces simply writes:

$$\mathbf{M_{edge}} = \begin{pmatrix} 1 & 0 \\ 0 & l \end{pmatrix}, \tag{B.37}$$

with l the drift length.

This way, the linear transfer matrix of each element of the cell can be obtained. It is then straightforward to obtain the linear parameters such as the phase advance (from the half-trace of the product of matrices) and the Twiss parameters (from the non-diagonal terms).

B.2 Step-wise tracking simulation code

During this study a step-wise tracking simulation code has been developed to study lattice parameters and 6D beam dynamics in FFAG accelerators. It is written in C language. In this section we describe the basic principles of this simulation code.

B.2.1 Particle tracking in static magnetic fields

We first of all consider the motion of a charged particle in a static magnetic field. In this case, since the magnetic force does not work, the total momentum p of the particle is invariant. The effect of electric fields coming from rf cavities is considered later (in Sec. B.2.2). The exact equations of motion express in cartesian coordinates (x, y, z) can thus be written as:

$$\begin{cases} \dfrac{\mathrm{d}u_x}{\mathrm{d}s} = \dfrac{(u_y B_z - u_z B_y)}{B\rho} \\ \dfrac{\mathrm{d}u_y}{\mathrm{d}s} = \dfrac{(u_z B_x - u_x B_z)}{B\rho} \\ \dfrac{\mathrm{d}u_z}{\mathrm{d}s} = \dfrac{(u_x B_y - u_y B_x)}{B\rho} \\ \dfrac{\mathrm{d}x}{\mathrm{d}s} = u_x \\ \dfrac{\mathrm{d}y}{\mathrm{d}s} = u_y \\ \dfrac{\mathrm{d}z}{\mathrm{d}s} = u_z \end{cases} , \tag{B.38}$$

where s is the longitudinal abscissa measured along the orbit of the particle, and $B\rho$ is the magnetic rigidity of the particle, also given by:

$$B\rho = \frac{p}{q}, \tag{B.39}$$

with q the charge of the particle. The magnetic field is $\vec{B}$ =(B_x, B_y, B_z), and $\vec{u}$ =(u_x, u_y, u_z) is a unit vector defined as:

$$\vec{u} = \frac{\vec{p}}{p}. \tag{B.40}$$

Analytical field modeling

To compute the trajectory of a particle, we need a description of the magnetic field produced by the scaling type of FFAG magnets. We choose to use

analytical field models similar to those used in the 'FFAG' proceedure of the tracking code Zgoubi, and described in Ref. [60].

We start by modeling the field distribution in the machine mid-plane. Since it is an anti-symmetry plane of the field distribution, only the vertical component B_z of the magnetic field may exist along this plane. In the case of radial sector type of FFAG cells, it is convenient to describe the field distribution in the mid-plane using the polar coordinates (r, θ). The contribution of each magnet is obtained following the equation:

$$B_z(r,\theta) = B_0\,\mathcal{F}(\theta)\,\left(\frac{r}{r_0}\right)^k, \tag{B.41}$$

where $B_0 = B_z(r_0, \theta)$. The function $\mathcal{F}(\theta)$ describes the azimuthal variation of the field. In our study we limit ourself to the case where $\mathcal{F}$ do not depend on r. The general form of this function is obtained using Enge type of field fall-off [61]:

$$\mathcal{F}(\theta) = \mathcal{F}_{en}(\theta)\,\cdot\,\mathcal{F}_{ex}(\theta) \tag{B.42}$$

with:

$$\mathcal{F}_{en,ex}(\theta) = \frac{1}{1+\exp\left(P(d_{en,ex})\right)}, \tag{B.43}$$

where d_{en} and d_{ex} the distance of the particle from the entrance and exit effective fringe field boundaries (EFB). These distances are calculated as follows:

$$\begin{aligned} d_{en} &= r\,\left(\theta_{EFB_{en}} - \theta\right) \\ d_{ex} &= r\,\left(\theta - \theta_{EFB_{ex}}\right) \end{aligned} \tag{B.44}$$

with $\theta_{FFB_{en}}$ and $\theta_{FFB_{ex}}$ the azimuth of the entrance and exit EFB. The polynomial $P(d)$ is given by:

$$P(d) = C_0 + C_1\frac{d}{\lambda} + C_2\left(\frac{d}{\lambda}\right)^2 + ... \tag{B.45}$$

where λ represents the fringe field extend. The value of λ is chosen proportional to r, providing that $\mathcal{F}$ only depends on θ.

The value of the coefficients $C_{0,1,...}$, which characterize the shape of the field fall-off, are obtained from a fit of the field distribution in the finite element model of the RACCAM prototype magnet [28]. In this study we thus always use $C_0 = 0$, $C_1 = 2.24$, and $C_i = 0$, $\forall i \geq 2$, since it fits quite well the fringe field shape at the injection radius of the RACCAM prototype magnet (model without field clamp), as shown if Fig. B.4.

Now that we know the contribution of each magnet to the mid-plane field, we use the Maxwell's equations to obtain the field components off the

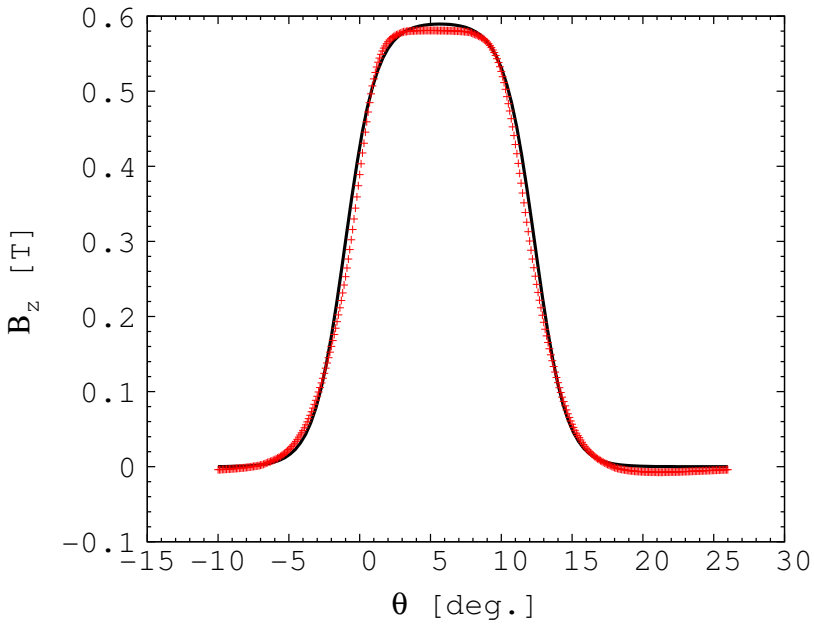

Figure B.4: Red points: field distribution along an arc of radius 2.8 m ($\sim$ injection radius) obtained from the 3D model without field clamp of the RACCAM prototype magnets. The black line shows the field distribution obtained following Eq. B.41, with λ = full gap height = 12 cm and $C_0 = 0$, $C_1 = 2.24$, and $C_i = 0,\ \forall i \geq 2$.

mid-plane. We thus consider the Taylor expansion of the field around the mid-plane:

$$B_u(r,\theta,z) = B_u(r,\theta,0) + \sum_{i=1}^{\infty} \frac{z^i}{i!} \frac{\partial^i B_u}{\partial z^i}\,, \tag{B.46}$$

with u standing for either r, θ or z, partial derivatives being taken at $z = 0$. Since the machine mid-plane is an anti-symmetry plane of the field distribution, we can write that:

$$\begin{aligned} B_r(r,\theta,0) &= 0 \\ B_\theta(r,\theta,0) &= 0 \\ B_r(r,\theta,-z) &= -B_r(r,\theta,z) \\ B_\theta(r,\theta,-z) &= -B_\theta(r,\theta,z) \\ B_z(r,\theta,-z) &= B_z(r,\theta,z) \end{aligned} \tag{B.47}$$

The Taylor expansion thus simplifies to:

$$\begin{aligned} B_r(r,\theta,z) &= z\frac{\partial B_r}{\partial z} + \frac{z^3}{6}\frac{\partial^3 B_r}{\partial z^3} + O(z^5) \\ B_\theta(r,\theta,z) &= z\frac{\partial B_\theta}{\partial z} + \frac{z^3}{6}\frac{\partial^3 B_\theta}{\partial z^3} + O(z^5) \\ B_z(r,\theta,z) &= B_0 + \frac{z^2}{2}\frac{\partial^2 B_z}{\partial z^2} + \frac{z^4}{24}\frac{\partial^4 B_z}{\partial z^4} + O(z^6) \end{aligned} \tag{B.48}$$

To express the partial derivatives used in the Taylor expansion as a function of the partial derivatives we can easily get from Eq. B.41, we use the Maxwell's equations. From the Maxwell-Ampère equation one gets:

$$\begin{aligned} \frac{\partial B_r}{\partial z} &= \frac{\partial B_z}{\partial r} && \text{(a)} \\ \frac{\partial B_\theta}{\partial z} &= \frac{1}{r}\frac{\partial B_z \theta}{\partial \theta} && \text{(b)} \\ \frac{\partial B_r}{\partial \theta} &= \frac{\partial B_\theta}{\partial r} && \text{(c)} \end{aligned} \quad . \tag{B.49}$$

From Eqs. B.49.a and B.49.b one can get the first order terms in Eq. B.48. Using together the Maxwell-Ampère and Maxwell-Gauss equations, one gets $\nabla^2 \vec{B} = \vec{0}$, and thus:

$$\begin{aligned} \frac{\partial^2 B_r}{\partial z^2} &= \frac{2}{r^2}\frac{\partial B_\theta}{\partial \theta} + \frac{B_r}{r^2} - \frac{\partial^2 B_r}{\partial r^2} - \frac{1}{r^2}\frac{\partial^2 B_r}{\partial \theta^2} - \frac{1}{r}\frac{\partial B_r}{\partial r} && \text{(a)} \\ \frac{\partial^2 B_\theta}{\partial z^2} &= \frac{B_\theta}{r^2} - \frac{\partial^2 B_\theta}{\partial r^2} - \frac{1}{r^2}\frac{\partial^2 B_\theta}{\partial \theta^2} - \frac{1}{r}\frac{\partial B_\theta}{\partial r} - \frac{2}{r^2}\frac{\partial B_r}{\partial \theta} && \text{(b)} \\ \frac{\partial^2 B_z}{\partial z^2} &= -\frac{\partial^2 B_z}{\partial r^2} - \frac{1}{r^2}\frac{\partial^2 B_z}{\partial \theta^2} - \frac{1}{r}\frac{\partial B_z}{\partial r} && \text{(c)} \end{aligned} \quad . \tag{B.50}$$

From Eqs. B.50.c one can get the second order term in Eq. B.48. Differentiating Eqs. B.50.a and B.50.b with respect to z and using again Eqs. B.49.a and B.49.b one can get the third order terms in Eq. B.48, and so on. In our code we do this extrapolation up to the 4^{th} order in z.

The magnetic field components at an arbitrary position (r, θ, z) of the cell is obtained summing the contribution of each magnet of the cell. Finally we move from cylindrical to cartesian coordinates by a straightforward change of variables.

We have thus described the principle used for the analytical field modeling. For the detail of the formula used, we show below the subroutine used to compute and add the field contribution of each FFAG magnet:

```
extern void add_onemag_FFAGradial_purescale(double x, double y, double z, double *bx, ↩
    double *by, double *bz, struct Cell *cell, int ic)
{
    double r, th, ffbe, ffbs, r0, bz0, k, role, c1e, rols, c1s,
        ee, es, u, dudt, d2udt2, d3udt3, d4udt4, f, dfdt, d2fdt2, d3fdt3, d4fdt4,
        b, dbdr, d2bdr2, d3bdr3, d4bdr4,
        dbzdr, d2bzdr2, d3bzdr3, d4bzdr4, dbzdt, d2bzdt2, d3bzdt3, d4bzdt4,
        dbrdz, dbtdz, d2bzdz2, d3brdz3, d3btdz3, d4bzdz4, br, bth;

    //-----------------------------------------------------------------//
    //convert cartesian local framework coordinates into cylindrical
    //-----------------------------------------------------------------//
    r = sqrt(x*x + y*y);
    th = atan_ratio(y, x);

    //-----------------------//
    //get magnet parameters
    //-----------------------//
    ffbe = cell->mpara[ic][0] + cell->efben[ic][0]; //azimuth of the entrance EFB
    ffbs = cell->mpara[ic][0] + cell->efbex[ic][0]; //azimuth of the exit EFB
    r0 = cell->mpara[ic][1];          //r0
    bz0 = cell->mpara[ic][2];         //B0
    k = cell->mpara[ic][3];           //geometrical field index
    role = r0/cell->efben[ic][1];     //r0/lambda0 entrance face
    c1e = cell->efben[ic][3];         //Enge coeff. c1 entrance face
    rols = r0/cell->efbex[ic][1];     //r0/lambda0 exit face
    c1s = cell->efbex[ic][3];         //Enge coeff. c1 exit face

    //-----------------------//
    //compute br, bth, bz
    //-----------------------//
    if(c1e*role*(ffbe - th) < NOOVFLOW_DOUBLE && c1s*rols*(th - ffbs) < ↩
        NOOVFLOW_DOUBLE) {//avoid ee and es to overflow the largest double when far ↩
        from the EFB

        ee = exp(c1e*role*(ffbe-th));
        es = exp(c1s*rols*(th-ffbs));
        u = (1+es)*(1+ee);
        dudt = c1s*rols*es*(1+ee)-c1e*role*ee*(1+es);
        d2udt2 = pow(c1s*rols, 2)*es*(1+ee)-2*c1s*rols*c1e*role*es*ee+pow(c1e*role, 2)↩
            *ee*(1+es);
        d3udt3 = pow(c1s*rols, 3)*es*(1+ee)-ee*es*(3*pow(c1s*rols, 2)*c1e*role-3*c1s*↩
            rols*pow(c1e*role, 2))-pow(c1e*role, 3)*ee*(1+es);
        d4udt4 = pow(c1s*rols, 4)*es*(1+ee)-ee*es*(4*pow(c1s*rols, 3)*c1e*role-6*pow(↩
            c1s*rols, 2)*pow(c1e*role, 2)+4*c1s*rols*pow(c1e*role, 3))+pow(c1e*role, ↩
            4)*ee*(1+es);

        b = bz0*pow(r/r0, k);
        dbdr = b*k/r; //radial component of the mid-plane Bz field
        d2bdr2 = dbdr*(k-1)/r; //and its derivatives...
        d3bdr3 = d2bdr2*(k-2)/r;
        d4bdr4 = d3bdr3*(k-3)/r;

        f = 1/u; //flutter
        dfdt = -dudt/(u*u); //dflutter/dth
        d2fdt2 = (2*dudt*dudt-u*d2udt2)/(u*u*u); //d2flutter/dth2
        d3fdt3 = (6*u*dudt*d2udt2-u*u*d3udt3-6*dudt*dudt*dudt)/(u*u*u*u); //d3flutter/↩
            dth3
        d4fdt4 = (u*(6*u*d2udt2*d2udt2-u*u*d4udt4+4*u*dudt*d3udt3-12*dudt*dudt*d2udt2)↩
            -4*dudt*(6*u*dudt*d2udt2-u*u*d3udt3-6*dudt*dudt*dudt))/(u*u*u*u*u); //↩
            d4flutter/dth4

        //derivatives of the mid-plane Bz field /dr and /dth
        dbzdr   = f*dbdr;
        d2bzdr2 = f*d2bdr2;
        d3bzdr3 = f*d3bdr3;
        d4bzdr4 = f*d4bdr4;
        dbzdt   = b*dfdt;
        d2bzdt2 = b*d2fdt2;
        d3bzdt3 = b*d3fdt3;
        d4bzdt4 = b*d4fdt4;

        //derivatives /dz used to get the coeff. of the Taylor expansion
        dbrdz   = dbzdr;
        dbtdz   = 1/r*dbzdt;
        d2bzdz2 = -1/r*dbzdr-d2bzdr2-1/(r*r)*d2bzdt2;
        d3brdz3 = 2/(r*r*r)*d2bzdt2-d3bzdr3+1/(r*r)*dbzdr-1/r*d2bzdr2-1/(r*r)*d2fdt2*↩
            dbdr;
        d3btdz3 = -1/r*d2bdr2*dfdt-1/(r*r*r)*d3bzdt3-1/(r*r)*dfdt*dbdr;
        d4bzdz4 = 1/(r*r*r*r)*d4bzdt4+d4bzdr4+2/(r*r)*d2bdr2*d2fdt2+2/r*d3bzdr3-2/(r*r↩
            *r)*d2fdt2*dbdr-1/(r*r)*d2bzdr2+1/(r*r*r)*dbzdr+4/(r*r*r*r)*d2bzdt2;

        //compute br, bth
        br  = z*dbrdz+z*z*z/6*d3brdz3;
        bth = z*dbtdz+z*z*z/6*d3btdz3;

        //-----------------------------------------------------------//
```

```
        //add contribution of this magnet (in the local cartesian framework)
        //-------------------------------------------------------------------//
        *bx += br*cos(th)-bth*sin(th);
        *by += bth*cos(th)+br*sin(th);
        *bz += f*b+z*z/2.*d2bzdz2+z*z*z*z/24*d4bzdz4;
    }
}
```

Integration of the equations of motion

Now that we have a description of the 3D field distribution, we use numerical integration to solve step-by-step the equations of motion (Eq. B.38). To that end we use standard 4^{th} order Runge-Kutta integration algorithms (see Ref. [82]). Such integrators are wildly used in many fields of research because they provide a high level of precision for a limited amount of computation time. They moreover do not require to specify a reference orbit around which the motion is integrated, by contrast to symplectic integrators. This is a essential feature for simulating acceleration in the case of FFAGs, in which the closed orbit moves during acceleration.

However, the main drawback of such integrators is that the errors coming from the truncated terms, although very small for each step, can be accumulated over a large number of steps, which may lead to artificial non-symplectic behaviors.

For the standard code Zgoubi (which is also non-necessarily symplectic) as for the code we developed during this study, a careful use is required. One must for instance always use simple tests such as single particle tracking; if one observe trajectories in the transverse phase spaces which are not bounded, this may come from either a resonant behavior or a problem of symplecticity. Doing again the same simulation with a smaller step-size, one can distinguish between these two effects. In this study such tests are presented in Secs. 3.4.1 and 4.5.1. They all show bounded motion in both horizontal and vertical planes.

B.2.2 Acceleration: effect of the rf field

We simulate the effect of thin rf gaps by incrementing the kinetic energy of the particle of qV_{rf}, with q the charge of the particle, and the rf gap voltage V_{rf} is given by:

$$V_{rf} = V_0 \sin(2\pi f_{rf} t + \phi_0), \tag{B.51}$$

where the cavity peak voltage V_0, the rf frequency f_{rf}, and the initial phase ϕ_0 are kept unchanged during acceleration. It is thus necessary to know the time of flight t of the particle. This required to integrate an additional differential equation:

$$\frac{\mathrm{d}t}{\mathrm{d}s} = \frac{\gamma}{c(\gamma^2 - 1)}, \tag{B.52}$$

where c is the speed of light and γ is the Lorentz factor of the particle. While only the knowledge of the particle rigidity ($B\rho$) was enough to solve the equation of motion without acceleration (Eq. B.38), we need here to know also the particle rest mass m_0 and charge q to be able to determine its Lorentz factor since:

$$\gamma = \sqrt{1 + \left(\frac{qB\rho}{m_0 c}\right)^2}. \tag{B.53}$$

B.2.3 Calculation of the linear parameters

If we neglect the effect of non-linear field components, the particle motion with respect to its closed orbit can be described in either the horizontal of the vertical planes by means of linear transfer matrices:

$$\begin{pmatrix} y_1 \\ y'_1 \end{pmatrix} = \begin{pmatrix} a_{11} & a_{12} \\ a_{21} & a_{22} \end{pmatrix} = \begin{pmatrix} y_0 \\ y'_0 \end{pmatrix}, \tag{B.54}$$

where y stands either for x or z. To determine such transfer matrices, we track five particles with initial positions as described in Fig. B.5.

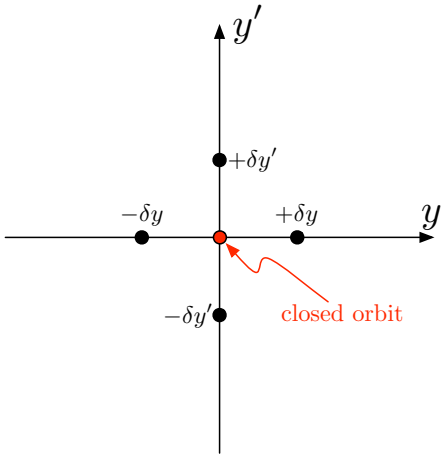

Figure B.5: Initial position in a transverse phase space (either horizontal or vertical) of the five particles used to compute the equivalent linear transfer matrix. The notation δy represents a small displacement perpendicularly to the closed orbit, while the notation $\delta y'$ represents a small angular deviation with respect to the closed orbit.

Taking into account non-linear forces, the positions of these particle after

tracking can be written as:

$$\begin{aligned} y_{+\delta y} &= a_{11}\delta y + b_{11}\delta y^2 + O(\delta y^3) \\ y_{-\delta y} &= -a_{11}\delta y + b_{11}\delta y^2 + O(\delta y^3) \\ y'_{+\delta y} &= a_{21}\delta y + b_{21}\delta y^2 + O(\delta y^3) \\ y'_{-\delta y} &= -a_{21}\delta y + b_{21}\delta y^2 + O(\delta y^3) \\ &... \end{aligned} \tag{B.55}$$

Here again the distance are measures perpendicularly to the closed orbit. The linear matrix coefficients is thus be determined as:

$$\begin{aligned} a_{11} &= \frac{y_{+\delta y} - y_{-\delta y}}{2\delta y} + O(\delta y^3) \\ a_{12} &= \frac{y'_{+\delta y} - y'_{-\delta y}}{2\delta y} + O(\delta y^3) \\ &... \end{aligned} \tag{B.56}$$

This way the contribution of the second order terms is thus cancelled out with this method. Values for δy and $\delta y'$ are chosen small (typically 0.1 mm and 0.1 mrad), so that the truncation error $O(\delta y^3)$ is negligible.

Once the equivalent transfer matrix between two arbitrary points of the lattice can be obtained, it is straightforward to get the values linear tunes tunes, as well as phase advances and periodic Twiss-parameters all along the lattice.

B.2.4 Estimation of the dynamic aperture

To estimate the dynamic aperture of a given FFAG lattice, we use particle tracking at fixed energy to estimate the largest horizontal amplitude for which the motion stays stable over a large number of periods (= 1350 in the example plotted in 3.5). Several particles are thus launched with various initial horizontal displacements (with a step size of 1 mm) and 1 mm initial vertical displacement, and then tracked over 6 turns (without introducing errors). Far horizontal and vertical collimators ($\pm$ 1 m from the closed orbit) are used to identify unstable particle motion. Once we determined the largest initial displacement $x_{0_{max}}$ for which particle is not lost on collimators during tracking, we define the corresponding horizontal acceptance ϵ_x, using the linear approximation:

$$\epsilon_x = \gamma_x \cdot x_{0_{max}}^2, \tag{B.57}$$

with γ_x the Twiss parameter at the position where the particle was initially launched.

The vertical acceptance is estimated using a similar method, replacing the initial horizontal displacements by vertical displacements (and inversely), and using the linear approximation:

$$\epsilon_z = \gamma_z \cdot z_{0_{max}}^2, \tag{B.58}$$

with γ_z the Twiss parameter at the position where the particle was initially launched.

B.2.5 Basic code structure and interfaces

essential to track in rings with complicated geometries!!!

B.3 Zgoubi.dat

We give below the detail of a Zgoubi input file (zgoubi.dat) used in simulations described in Sec. 3.4.1.

```
SBA 3.6 to 12.6 GeV muon ring (WP04)
'OBJET'                                                                    1
12355.7                                        3.6GeV muon
2
2 2
16090.972097     0.    0.1    0.    0.    1.    'o'      3.6GeV on closed orbit + 3cm
16094.872097     0.    0.1    0.    0.    1.    'o'      3.6GeV on closed orbit + 6.9cm
1   1
'FAISTORE'                                                                 3
zgoubi.fai
1

'COLLIMA'                                                                  4
2
1 100 100 16100 0.

 'FFAG'                                                                    5
 0

 3    1.6      16100.                          NMAG, AT=tetaF+2tetaD+2Atan(XFF/R0), R0
 0.4   0.   32.118   1390              mag 1 : ACNT, dum, B0, K
 16.   -1.                                    EFB 1 : lambda, gap constant/var=0/.ne.0
 4   0.    2.24   0.   0.  0.  0.   0.
 0.129  0.     1.E6   -1.E6   1.E6   1.E6
 16.   -1.                                    EFB 2
 4   0.    2.24   0.   0.  0.  0.   0.
-0.129   0.     1.E6   -1.E6   1.E6   1.E6
 0. -1                                        EFB 3 : inhibited by iop=0
 0   0.       0.       0.       0.       0.  0.   0.
 0.   0.    0.     0.     0.  0.

 0.8   0.   -44.927   1390               mag 2 : ACNT, dum, B0, K
 16.   -1.                                    EFB 1 : lambda, gap constant/var=0/.ne.0
 4   0.    2.24   0.   0.  0.  0.   0.
 0.19  0.     1.E6   -1.E6   1.E6   1.E6
 16.   -1.                                    EFB 2
 4   0.    2.24   0.   0.  0.  0.   0.
-0.19   0.     1.E6   -1.E6   1.E6   1.E6
 0. -1                                        EFB 3 : inhibited by iop=0
 0   0.       0.       0.       0.       0.  0.   0.
 0.   0.    0.     0.     0.  0.

 1.2   0.   32.118   1390              mag 3 : ACNT, dum, B0, K
 16.   -1.                                    EFB 1 : lambda, gap constant/var=0/.ne.0
 4   0.    2.24   0.   0.  0.  0.   0.
 0.129  0.     1.E6   -1.E6   1.E6   1.E6
 16.   -1.                                    EFB 2
 4   0.    2.24   0.   0.  0.  0.   0.
-0.129   0.     1.E6   -1.E6   1.E6   1.E6
 0. -1                                        EFB 3 : inhibited by iop=0
 0   0.       0.       0.       0.       0.  0.   0.
 0.   0.    0.     0.     0.  0.

 4 500.                      KIRD anal/num (=0/2,25,4), resol(mesh=step/resol)
 0.5                             integration step size (cm)
 2    0.   0.  0.  0.         (comp anal/num yield best num prec for resol=1e3*step)

'MARKER'     BEG    .plt                                                   6

'REBELOTE'                                                                 7
1350 0.2 99

'END'                                                                      8
```

Bibliography

[1] T. Ohkawa, in: Symposium on Nuclear Physics of the Physics Society of Japan, 1953, y. Mori, private communication.

[2] K. R. Symon, D. W. Kerst, L. W. Jones, L. J. Laslett, K. M. Terwilliger, Fixed-field alternating-gradient particle accelerators, Phys. Rev. 103 (6) (1956) 1837–1859. doi:10.1103/PhysRev.103.1837.

[3] F. T. Cole, O CAMELOT! A memoir of the MURA years, (section 6.1), april 1994, published in: Proc. Cycl. Conf., 2001.
URL http://cern.ch/AccelConf/c01/cyc2001/extra/Cole.pdf

[4] E. D. Courant, M. S. Livingston, H. S. Snyder, The strong-focusing synchroton—a new high energy accelerator, Phys. Rev. 88 (5) (1952) 1190–1196. doi:10.1103/PhysRev.88.1190.

[5] F. T. Cole, R. O. Haxby, L. W. Jones, C. H. Pruett, and K. M. Terwilliger, Electron model fixed field alternating gradient accelerator, Rev. Sci. Instrum. 28 (6) (1957) 403–420. doi:10.1063/1.1715895.

[6] D. W. Kerst, E. A. Day, H. J. Hausman, R. O. Haxby, L. J. Laslett, F. E. Mills, T. Ohkawa, F. L. Peterson, E. M. Rowe, A. M. Sessler, J. N. Snyder, and W. A. Wallenmeyer, Electron model of a spiral sector accelerator, Rev. Sci. Instrum. 31 (10) (1960) 1076–1106. doi:10.1063/1.1716818.

[7] F. T. Cole, G. Parzen, C. H. Pruett, W. A. Wallenmeyer, and D. E. Young, MURA 50-MeV electron accelerator general description and review, Rev. Sci. Instrum. 35 (11) (1964) 1393–1397. doi:10.1063/1.1719171.

[8] D. W. Kerst, *et al.*, Fixed field alternating gradient accelerators with spirally ridged poles, Phys. Rev. 98 (4) (1955) 1153, in: Minutes of the Meeting of the Division of Fluid Dynamics, Virginia, November, 1954, p. 1153. doi:10.1103/PhysRev.98.1139.

[9] M. Craddock, The rebirth of the FFAG, CERN Courier July 2004.
URL http://cerncourier.com/cws/article/cern/29119

[10] Y. Mori, FFAG proton driver for muon source, Nucl. Instr. and Meth. A 451 (1) (2000) 300 – 303. doi:10.1016/S0168-9002(00)00555-6.

[11] A. G. Ruggiero, FFAG accelerator proton driver for neutrino factory, Nuclear Physics B - Proceedings Supplements 155 (1) (2006) 315–317, proceedings to the 7th International Workshop on Neutrino Factories and Superbeams. doi:10.1016/j.nuclphysbps.2006.02.109.

[12] G. Rees, An FFAG proton driver for a Neutrino Factory, ICFA Beam Dynamics Newsletter 43 (2007) 102–110.

[13] M. Aiba, *et al.*, Development of a FFAG proton synchrotron, in: Proc. of EPAC'00 Conf., 2000, pp. 581–583.

[14] S. Machida, *et al.*, Beam optics design of an FFAG synchrotron, in: Proc. of EPAC'00 Conf., 2000, pp. 557–559.

[15] S, Machida, *et al.*, Commissioning of 150MeV FFAG synchrotron, in: Proc. of EPAC'04 Conf., 2004, pp. 2643–2645.

[16] C. H. Pyeon, T. Misawa, J-Y. Lim, H Unesaki, Y. ishi, Y Kuriyama, T. Uesugi, Y. Mori, M. Inoue, K. Nakajima, K. Mishima, and S. Shiroya, First injection of spallation neutrons generated by high-energy protons into the Kyoto University Critical Assembly, J. Nucl. Sci. Tech. 46 (12) (2009) 1091–1093. doi:10.3327/jnst.46.1091.

[17] M. Tanigaki, *et al.*, Construction of FFAG accelerators in KURRI for ADS study, in: Proc. of APAC2004 Conf., 2004, pp. 517–519.

[18] K. Yoshimura, Prism overview, Nucl. Instr. and Meth. A 503 (1-2) (2003) 254 – 257. doi:10.1016/S0168-9002(03)00688-0.

[19] Y. Arimoto, T. Oki, M. Hossain, Y. Takubo, M. Aoki, T. Itahashi, Y. Kuriyama, N. Miyamoto, A. Sato, M. Yoshida, Y. Kuno, Magnetic field measurement of large aperture FFAG magnet for muon-phase-rotation ring, Nucl. Instr. and Meth. B 268 (2) (2010) 200 – 208. doi:10.1016/j.nimb.2009.10.173.

[20] J. Pasternak, *et al.*, Accelerator and particle physics research for the next generation muon to electron conversion experiment - the PRISM task force, in: Proc. of IPAC'10 Conf., 2010, pp. 3473–3475.

[21] Y. Mori, Development of FFAG accelerators and their applications for intense secondary particle production, Nucl. Instr. and Meth. A 562 (2) (2006) 591 – 595. doi:10.1016/j.nima.2006.02.044.

[22] K. Okabe, *et al.*, An intense neutron source with emittance recovery internal target (ERIT) using ionization cooling, in: Proc. of EPAC'08 Conf., 2008, pp. 3512–3514.

[23] S. Antoine, B. Autin, W. Beeckman, J. Collot, M. Conjat, F. Forest, J. Fourrier, E. Froidefond, J.L. Lancelot, J. Mandrillon, P. Mandrillon, F. Méot, Y. Mori, D. Neuvéglise, C. Ohmori, J. Pasternak and T. Planche, Principle design of a proton-therapy, rapid-cycling, variable energy spiral FFAG, Nucl. Instr. and Meth. A 602 (2) (2009) 293 – 305. doi:10.1016/j.nima.2009.01.025.

[24] K. Peach, *et al.*, PAMELA - a model for an FFAG based hadron therapy machine, in: Proc. of PAC'07 Conf., 2007, pp. 2880–2882.

[25] J. S. Berg, The emma main ring lattice, Nucl. Instr. and Meth. A 596 (3) (2008) 276 – 284. doi:10.1016/j.nima.2008.08.068.

[26] M. Aiba, *et al.*, A 150MeV FFAG synchrotron with "return-yoke free" magnet, in: Proc. of PAC'01 Conf., 2001, pp. 3254–3256.

[27] K. Okabe, T. Uesugi, Y. Kuriyama, T. Planche, J.-B. Lagrange, Y. Ishi, I. Sakai, Y. Mori, Design and construction of FFAG magnets for the ERIT system at KURRI, Applied Superconductivity, IEEE Transactions on 20 (3) (2010) 740–743. doi:10.1109/TASC.2010.2042696.

[28] T. Planche, J. Fourrier, J.L. Lancelot, F. Méot, D. Neuvéglise and J. Pasternak, Design of a prototype gap shaping spiral dipole for a variable energy protontherapy FFAG, Nucl. Instr. and Meth. A 604 (3) (2009) 435 – 442. doi:10.1016/j.nima.2009.02.026.

[29] SAD home page.
URL http://acc-physics.kek.jp/SAD/sad.html

[30] F. Méot, The ray-tracing code zgoubi, Nucl. Instr. and Meth. A 427 (1-2) (1999) 353 – 356. doi:10.1016/S0168-9002(98)01508-3.

[31] M. Aiba and F. Méot, Determination of KEK 150 MeV FFAG parameters from ray-tracing in TOSCA eld maps, Tech. Rep. CEA DAPNIA-04-188, CERN-NUFACT-Note-140, CEA DAPNIA (Oct. 2004).
URL http://cdsweb.cern.ch/record/806545

[32] Y. Mori, *et al.*, A new type of rf cavity for high intensity proton synchro- tron using high permeability magnetic alloy, in: Proc. of EPAC'98 Conf., 1998, pp. 299–301.

[33] I. Bolotin, *et al.*, Ferromagnetic cores made from amorphous material for broad-band accelerating system, in: Proc. of PAC'95 Conf., Vol. 3, 1995, pp. 1833 –1834. doi:10.1109/PAC.1995.505377.

[34] K. Nagamine, H. Miyadera, A. Jason, R. Seki, Compact muon source with electron accelerator for a mobile [mu]sr facility, Physica B: Condensed Matter 404 (5-7) (2009) 1020 – 1023, proceedings of the Eleventh International Conference on Muon Spin Rotation, Relaxation and Resonance. doi:10.1016/j.physb.2008.11.231.

[35] K. Nagamine, K. Shimomura, K. Imai, J. Schultz, Probing magnetism in human blood by muon spin relaxation, Physica B: Condensed Matter 374-375 (2006) 444 – 447, proceedings of the Tenth International Conference on Muon Spin Rotation, Relaxation and Resonance. doi:10.1016/j.physb.2005.11.128.

[36] K. Nagamine, Advanced muon radiography with compact accelerator system, in: Proc. Jpn. Acad. Ser. B, 2004, pp. 179–182.
URL http://www.japan-acad.go.jp/en/publishing/pja_b/contents/80/80_4.html

[37] R. P. Walker, synchrotron radiation, in: Proceedings of CERN accelerator school, University of Jyväskylä, Finland, 1992, pp. 437–459.

[38] International linear collider reference design report, vol. 3 (2007).
URL http://www.linearcollider.org/about/Publications

[39] C. M. Ankenbrandt, M. Atac, B. Autin, V. I. Balbekov, V. D. Barger, O. Benary, J. S. Berg, M. S. Berger, E. L. Black, A. Blondel, S. A. Bogacz, T. Bolton, S. Caspi, C. Celata, W. Chou, D. B. Cline, J. Corlett, L. Cremaldi, H. T. Diehl, A. Drozhdin, R. C. Fernow, D. A. Finley, Y. Fukui, M. A. Furman, T. Gabriel, J. C. Gallardo, A. A. Garren, Status of muon collider research and development and future plans, Phys. Rev. ST Accel. Beams 2 (8) (1999) 081001. doi:10.1103/PhysRevSTAB.2.081001.

[40] S. Geer, Neutrino beams from muon storage rings: Characteristics and physics potential, Phys. Rev. D 57 (11) (1998) 6989–6997. doi:10.1103/PhysRevD.57.6989.

[41] The ISS Physics Working Group, Accelerator design concept for future neutrino facilities v2, report number: RAL-TR-2007-019, arXiv:0710.4947v2 (2007). doi:10.1088/0034-4885/72/10/106201.
URL http://arxiv.org/abs/0710.4947v2

[42] S. Ozaki, R. Palmer, M. Zisman and J. Gallardo (eds.), Feasibility Study-II of a Muon-Based Neutrino Source, BNL-52623 (2001).
URL http://www.cap.bnl.gov/mumu/studyii/final_draft/The-Report.pdf

[43] Y. Kuno, Y. Mori, and the NufactJ Working Group, A feasibility study of a neutrino factory in Japan, v. 1.0 (2001).
URL http://www-prism.kek.jp/nufactj/nufactj.pdf

[44] The ISS Accelerator Working Group, Physics at a future neutrino factory and super-beam facility v2, report number: RAL-TR-2007-23, arXiv:0802.4023v2 (2007). doi:10.1088/1748-0221/4/07/P07001.
URL http://arxiv.org/abs/0802.4023

[45] The ISS Accelerator Working Group, *et al.*, Accelerator design concept for future neutrino facilities, J. Instr. 4 (2009) P07001. doi:10.1088/1748-0221/4/07/P07001.

[46] The IDS-NF front page. [link].
URL https://www.ids-nf.org/wiki/FrontPage

[47] J. Berg, Recent results from optimization studies of linear non-scaling FFAGs for muon acceleration, in: S. Machida, Y. Mori, and T. Yokoi (Ed.), Proc. of FFAG'04 conference, Osaka, Japan, 2004, pp. 1–8.
URL http://hadron.kek.jp/FFAG/FFAG04_HP/

[48] S. Machida, D. J. Kelliher, Orbit and optics distortion in fixed field alternating gradient muon accelerators, Phys. Rev. ST Accel. Beams 10 (11) (2007) 114001. doi:10.1103/PhysRevSTAB.10.114001.

[49] J. S. Berg, Amplitude dependence of time of flight and its connection to chromaticity, Nucl. Instr. and Meth. A 570 (1) (2007) 15 – 21. doi:10.1016/j.nima.2006.09.099.

[50] S. Machida, Longitudinal emittance blowup in fixed field alternating gradient muon accelerators, Phys. Rev. ST Accel. Beams 9 (10) (2006) 104002. doi:10.1103/PhysRevSTAB.9.104002.

[51] the IDS-NF Collaboration , First progress report, IDS-NF-017-v1.2 (2010).
URL https://www.ids-nf.org/wiki/FrontPage/Documentation

[52] J. Berg, S. Kahn, R. Palmer, Overview of acceleration for a neutrino factory, Nucl. Phys. B - Proc. Sup. 149 (2005) 306 – 308, nuFact04. doi:10.1016/j.nuclphysbps.2005.05.055.

[53] E. D. Courant, H. S. Snyder, Theory of the alternating-gradient synchrotron,, Annals of Physics 3 (1) (1958) 1 – 48. doi:DOI:10.1016/0003-4916(58)90012-5.

[54] G. Guignard, A general treatment of resonances in accelerators, Tech. Rep. 78-11, CERN, lecture given in the Academic Training Programme of CERN 1977-1978 (Nov. 1978).

[55] R. D. Ruth, Single particle dynamics in circular accelerators, Tech. Rep. SLAC-PUB-4103, SLAC, Stanford University, Stanford, CA 94305 (Oct. 1986).

[56] P. J. Bryant and K. Johnsen, The pinciples of circular accelerators and storage rings, Cambridge University Press, 1993.

[57] M. Conte and W.W. MacKay, An introduction to the physics of particle accelerators, World Scientific, 1991.

[58] Y. Mori, FFAG accelerators and their applications, in: Proceedings of EPAC'06 Conference, Edinburgh, UK, 2006, pp. 950–954.

[59] T. Nakamoto, N. Higashi, T. Ogitsu, A. Terashima, Y. Ajima, M. Anerella, R. Gupta, Y. Iwamoto, N. Kimura, Y. Makida, T. Obana, H. Ohhata, B. Parker, K. Sasaki, K. Tanaka, T. Tomaru, P. Wanderer, A. Yamamoto, Development of a prototype of superconducting combined function magnet for the 50 gev proton beam line for the j-parc neutrino experiment, Applied Superconductivity, IEEE Transactions on 15 (2) (2005) 1144 – 1147. doi:10.1109/TASC.2005.849515.

[60] F. Lemuet, F. Mot, Developments in the ray-tracing code Zgoubi for 6-D multi-turn tracking in FFAG rings, Nucl. Instr. and Meth. A 547 (2-3) (2005) 638 – 651. doi:10.1016/j.nima.2005.03.156.

[61] H.A. Enge, Deflecting magnets, Focusing of Charger Particles, academic press, new york, london Edition, Vol. 2, A. Septier, 1967, chapter 4.2, pp. 203–264.

[62] V. I. Veksler, J. Phys. U.S.S.R. 9 (3) (1945) 153.

[63] W. J. Henderson, H. LeCame and R. Montaibetta, A magnetic resonance accelerator for electrons, Nature 162 (1948) 699–700. doi:10.1038/162699a0.

[64] A. G. Ruggiero, rf acceleration with harmonic number jump, Phys. Rev. ST Accel. Beams 9 (10) (2006) 100101. doi:10.1103/PhysRevSTAB.9.100101.

[65] J. Scott Berg, Harmonic number jump in a ring with rf cavities distributed everywhere, in: Y. Mori, *et al.* (Ed.), Proceedings of FFAG'06 Conference, KURRI, Osaka, Japan, 2006, pp. 69–76.

[66] M. Puglisi, Conventional rf system design, in: Proceedings of CERN accelerator school, University of Jyväskylä, Finland, 1992, pp. 679–715.

[67] P. F. Meads, A dispersion-free long straight section for a fixed-field alternating-gradient synchrotron, Nuclear Science, IEEE Transactions on 30 (4) (1983) 2448 –2450. doi:10.1109/TNS.1983.4332843.

[68] P. F. Meads, A compensated dispersion-free long insertion for an FFAG synchrotron, in: Proceedings of the Particle Accelerator Conference 1993, 1993, pp. 3825–3827 vol.5. doi:10.1109/PAC.1993.309814.

[69] T. Ohkawa, Two-beam fixed field alternating gradient accelerator, Rev. Sci. Instru. 29 (2) (1957) 108–117.

[70] F. T. Cole, *et al.*, MURA 50-mev electron accelerator–general description and review, Rev. Sci. Instrum. 35 (11) (1964) 1393–1397. doi:10.1063/1.1719171.

[71] T. Nakamoto, *et al.*, Design of superconducting combined function magnets for the 50 gev proton beam line for the J-PARC neutrino experiment, IEEE Trans. App. Supercond. 14 (2) (2004) 616 – 619. doi:10.1109/TASC.2004.830010.

[72] R. J. Noble, Particle production and survival in muon acceleration (1993).
URL http://citeseerx.ist.psu.edu/viewdoc/summary?doi=10.1.1.156.6897

[73] A. Bogacz, Progress on muon linac and RLAs, presentation at the fourth IDS-NF planetary meeting (2009).
URL https://www.ids-nf.org/wiki/TIFR-2009-10-12/Agenda/Accelerator#session1

[74] J. Pasternak *et al.*, Low energy scaling FFAG option, presentation at the fifth IDS-NF planetary meeting (2010).
URL https://www.ids-nf.org/wiki/FNAL-2010-04-08/Agenda/Accelerator#session3

[75] JB. Lagrange, *et al.*, Applications of advanced scaling FFAG accelerator, in: Proceedings of IPAC'10 Conf., 2010, pp. 4503–4505.

[76] J. Pasternak, *et al.*, Accelerator and particle physics research for the next generation muon to electron conversion experiment - the prism task force, in: Proceedings of IPAC'10 Conf., 2010, pp. 3473–3475.

[77] A. Sato, *et al.*, Muon cooling in a racetrack FFAG using superfluid helium wedge absorbers, in: Proceedings of COOL'09 Conf., 2009, to be published.

[78] A.A. Kolomensky and A.N. Lebedev, Theory of cyclic accelerators, North-Holland publishing company - Amsterdam, 1966, english version (Translated from the Russian by M. Barbier).

[79] E. Yamakawa and Y. Mori, Stationary bucket acceleration in scaling FFAG accelerator, in: Proc. of FFAG'09 conf., 2009, p. to be published.

[80] G. Parzen, Non-linear resonances in alternating gradient accelerators, Tech. Rep. 200, Midwest Universities Research Association (MURA) (Oct. 1956).

[81] F.T. Cole, Remarks on the design of FFAG accelerators, Tech. Rep. 456, Midwest Universities Research Association (MURA), 2203 University Avenue, Madison, Wisconsin (Oct. 1959).

[82] W.H. Press, S.A. Teukolsky, W.T. Vetterling, and B.P. Flannery, Numerical Recipies in C, 2nd Edition, Cambridge University Press, Reading, Massachusetts, 1992, Ch. 16. URL http://www.nrbook.com/a/bookcpdf.php

List of publications

Related to chapter 3:

Reviewed paper: T. Planche, E. Yamakawa, T. Uesugi, J.-B. Lagrange, Y. Kuriyama, K. Okabe, Y. Ishi and Y. Mori, Scaling FFAG rings for rapid acceleration of muon beams, Nucl. Instr. and Meth. A 622 (1) (2010), p. 21–27.

Reviewed paper: T. Planche, J. Fourrier, J.L. Lancelot, F. Méot, D. Neuvéglise and J. Pasternak, Design of a prototype gap shaping spiral dipole for a variable energy protontherapy FFAG, Nucl. Instr. and Meth. A 604 (3) (2009), p. 435–442.

Reviewed paper: S. Antoine, B. Autin, W. Beeckman, J. Collot, M. Conjat, F. Forest, J. Fourrier, E. Froidefond, J.L. Lancelot, J. Mandrillon, P. Mandrillon, F. Méot , Y. Mori, D. Neuvéglise, C. Ohmori, J. Pasternak and T. Planche, Principle design of a protontherapy, rapid-cycling, variable energy spiral FFAG, Nucl. Instr. and Meth. A 602 (3) (2009), p. 293–305.

Conference proceeding: T. Planche, J-B Lagrange, E. Yamakawa, Y. Ishi, Y. Kuriyama, Y. Mori, New approaches to muon acceleration with zero-chromatic FFAGs, Proc. of IPAC'10 Conf., Kyoto, Japan (2010), p. 4506–4508.

Related to chapter 4:

Reviewed paper: T. Planche, J-B. Lagrange, E. Yamakawa, T. Uesugi, Y. Kuriyama, K. Okabe, Y. Ishi and Y. Mori, Harmonic number jump acceleration of muon beams in zero-chromatic FFAG rings, to be published in: Nucl. Instr. and Meth. A (2010).

Reviewed conference paper: T. Planche, J.-B. Lagrange, Y. Mori and T. Uesugi, Scaling FFAG lattices for muon acceleration, AIP Conf. Proc., 1222-1, p. 368–372.

Reviewed conference paper: T. Planche, J.-B. Lagrange and Y. Mori, Harmonic number jump acceleration in scaling FFAG rings, to be published in: Proc. of FFAG'09 Conf., FNL Batavia, USA (2009).

Conference proceeding: T. Planche and Y. Mori, Harmonic number jump acceleration in scaling FFAG ring, Proc. of PAC09 Conf., Vancouver, BC, Canada (2010), URL:http://trshare.triumf.ca/~pac09proc/Proceedings/html/author.htm.